

Effects of bone structural unit (BSU) geometry and material properties on crack growth through idealized trabecular microstructures

by

Pavel Rahovich

A thesis submitted in partial fulfillment  
of the requirements for the degree of  
Master of Applied Science (MAsc) in Engineering Science

The Office of Graduate Studies  
Laurentian University  
Sudbury, Ontario, Canada

©Pavel Rahovich, 2022

**THESIS DEFENCE COMMITTEE/COMITÉ DE SOUTENANCE DE THÈSE**  
**Laurentian Université/Université Laurentienne**  
Office of Graduate Studies/Bureau des études supérieures

Title of Thesis Titre de la thèse	Effects of bone structural unit (BSU) geometry and material properties on crack growth through idealized trabecular microstructures	
Name of Candidate Nom du candidat	Rahovich, Pavel	
Degree Diplôme	Master of Science	
Department/Program Département/Programme	Engineering Science	Date of Defence Date de la soutenance October 18, 2022

**APPROVED/APPROUVÉ**

Thesis Examiners/Examineurs de thèse:

Dr. Brent Livers  
(Co-Supervisor/Co-directeur(trice) de thèse)

Dr. Krishna Challagulla  
(Co-Supervisor/Co-directeur(trice) de thèse)

Dr. Junfeng Zhang  
(Committee member/Membre du comité)

Dr. Ming Cai  
(Committee member/Membre du comité)

Dr. Brent Edwards  
(External Examiner/Examineur externe)

Approved for the Office of Graduate Studies  
Approuvé pour le Bureau des études supérieures  
Tammy Eger, PhD  
Vice-President Research (Office of Graduate Studies)  
Vice-rectrice à la recherche (Bureau des études supérieures)  
Laurentian University / Université Laurentienne

**ACCESSIBILITY CLAUSE AND PERMISSION TO USE**

I, **Pavel Rahovich**, hereby grant to Laurentian University and/or its agents the non-exclusive license to archive and make accessible my thesis, dissertation, or project report in whole or in part in all forms of media, now or for the duration of my copyright ownership. I retain all other ownership rights to the copyright of the thesis, dissertation or project report. I also reserve the right to use in future works (such as articles or books) all or part of this thesis, dissertation, or project report. I further agree that permission for copying of this thesis in any manner, in whole or in part, for scholarly purposes may be granted by the professor or professors who supervised my thesis work or, in their absence, by the Head of the Department in which my thesis work was done. It is understood that any copying or publication or use of this thesis or parts thereof for financial gain shall not be allowed without my written permission. It is also understood that this copy is being made available in this form by the authority of the copyright owner solely for the purpose of private study and research and may not be copied or reproduced except as permitted by the copyright laws without written authority from the copyright owner.

## Abstract

Bones containing large proportions of trabecular bone tissue such as the hip, wrist, and spinal column are highly susceptible to fracture. These fractures occur more frequently in the older populations, putting a large burden on the healthcare system and the society as a whole. Bone fracture prediction methods rely heavily on bone quantity measurements when predicting fracture risks. However, research has shown that only using bone quantity as the main predictor fails to identify a large number of patients with a high risk of bone fracture. Recent studies have shown that with age, the microstructure of the trabeculae changes as the patchwork of bone structural units (BSU), also known as trabecular packets, reduce in size due to the remodeling process. Unfortunately, little is known about the mechanical consequences of these changes on the trabeculae's ability to resist cracking. Smaller BSU with age may reduce fracture risk due to crack blunting or redirection. Conversely, smaller BSU results in a larger proportion of brittle cement line which could provide more preferential paths for crack growth. The present work used extended finite element method (XFEM) crack modeling techniques, which have recently been applied to simulate crack growth in cortical bone, to model crack propagation through idealized trabeculae in 2D. The material properties for the BSU and cement line, as well as the size of the BSU themselves, were varied through parametric studies. Smaller BSU were found to accelerate crack growth within bone. Other geometric parameters like aspect ratio and angle of crack deflection were also identified as major contributors to the bones ability to resist cracks. Future work should investigate more representative BSU geometries to further clarify the role these structures have on fracture risk.

**Keywords:** Trabecular bone; bone structural units (BSU); extended finite element method (XFEM); microstructure; cement line; crack propagation

# Contents

Abstract .....	III
List of Figures .....	VII
List of Tables .....	X
Nomenclature .....	XI
Acknowledgements.....	XII
1 Introduction.....	1
1.1 Motivation .....	1
1.2 Aim and objectives of the study.....	5
2 Literature review.....	6
2.1 Chapter introduction.....	6
2.2 Overview of bone .....	6
2.2.1 Hierarchical structure of bone .....	7
2.2.2 Cortical bone tissue .....	8
2.2.3 Trabecular bone tissue .....	9
2.2.4 Bone remodeling.....	10
2.2.5 Cement lines.....	11
2.2.6 BSU properties .....	13
2.3 Modeling crack propagation in bone .....	16
2.3.1 Continuum damage models .....	16
2.3.2 Discrete damage models .....	17
2.4 XFEM simulation of crack propagation in bone .....	19
2.5 Trabecular bone modeling .....	22
2.6 Literature review summary.....	23
3 Methods .....	24
3.1 Chapter introduction.....	24
3.2 Simulation model selection .....	24
3.3 XFEM modeling method.....	24
3.3.1 Crack domain.....	24
3.3.2 Initial crack location.....	25
3.3.3 Damage initiation .....	27
3.3.4 Limitations .....	28

3.4	Material properties .....	28
3.5	Recreation of previous studies and validation of subroutine.....	29
3.6	Modeling geometry .....	30
3.7	Boundary conditions .....	33
3.8	Data collection and results.....	34
3.9	Mesh analysis.....	35
3.10	Model adjustment.....	36
3.11	Parametric studies.....	37
3.11.1	First parametric study .....	37
3.11.2	Second parametric study .....	38
3.11.3	Third parametric study .....	43
4	Results .....	45
4.1	Recreation of Gustafsson osteon model .....	45
4.2	Boundary condition analysis .....	46
4.3	Mesh analysis.....	47
4.4	First parametric study: effects of QUADE critical strain and angles of deflection on crack path in a 2D representation of a trabecula .....	49
4.5	Second parametric study: effects of size of the BSU on the overall crack resistance of the trabeculae .....	50
4.6	Third parametric study: effects of the BSU geometry on the overall crack response in the cement line.....	52
5	Discussion and conclusion .....	55
5.1	Suitability of XFEM for analysis of crack propagation in trabecular bone.....	55
5.2	Identification of critical strain values.....	55
5.3	Effects of the cement line deflections on the microscopic strain to failure .....	56
5.4	Effects of reduction in BSU size on the trabeculae's ability to resist cracking.....	57
5.5	Limitations .....	57
5.6	Clinical implications.....	58
5.7	Future work.....	58
5.8	Conclusion.....	58
	References .....	60
	Appendix A: Fortran code for the cement line UDMGINI subroutine.....	70
	Appendix B: Python script for trabecular geometry generation.....	71



## List of Figures

Figure 1.1 An example of trabecular bone structure. The figure shows possible degradation of trabecular bone due to aging and degradative bone disease. Taken from [12] .....	2
Figure 1.2 Hierarchical structure of trabecular bone. Taken from [26] with permission from Journal of The Royal Society Interface.....	3
Figure 1.3 Simplified diagram showing the five stages of bone remodelling. Taken from [27] and reprinted under (CC BY).....	4
Figure 2.1 Hierarchical structure of bone. Taken from [36] with permission from Elsevier .....	7
Figure 2.2 Photomicrograph of the lamellar structure of cortical bone. Taken from [40] with permission from The Lancet .....	8
Figure 2.3 Trabecular profile with 20 labeled BSU and outlined cement lines. Taken from [28] with permission.....	9
Figure 2.4 From left to right: (A) A trabecula consisting of a patchwork of new and old BSU, separated by cement line (white), (B) a portion of bone is resorbed by remodeling cells, (C) new bone is laid down in the resorbed portion. Taken from [28] with permission .....	10
Figure 2.5 Vertebral trabecular bone architecture. Taken from [44] with permission from Elsevier .....	10
Figure 2.6 Cross section of fractured cortical bone taken from. Note tendency of crack propagation along the cement lines. Taken from [47] with permission.....	12
Figure 2.7 Regression line of the mean wall thickness of trabecular bone packets with advancing age. Taken from [72] with permission from Springer Nature .....	16
Figure 2.8 The principle of the phantom node method. Taken from [105].....	19
Figure 2.9 A set of damage models presented in literature that are used to model crack propagation in bone at the microscale. (A) 2D Crack simulation in cortical bone using the Element Deletion method taken from [79] with permission, (B) Crack analysis of a full bone using the Phase-field Model method Adapted from [88] with permission from John Wiley and Sons, (C) 2D Crack analysis around an osteon using the Cohesive Elements method Adapted from [96] with permission from American Society of Mechanical Engineers, (D) 2D crack propagation analysis of osteon using the XFEM method Adapted from [116] with permission from Elsevier .....	19
Figure 2.10 Sections of cancellous bone specimen. Taken from [118] with permission from sage Publishing.....	22
Figure 2.11 Model cases considered in the Hammond et al. study. Taken from [117] with permission from Elsevier .....	23
Figure 3.1 Crack path comparison between two test samples that were used to test crack domains. A: Sample with a single crack domain. B: Sample with five equally sized vertical crack domains. The crack path for both simulation is indicated in red .....	25
Figure 3.2 Initial crack indicated in red surrounded by a partition indicated in yellow .....	26
Figure 3.3 A) A model where the initial crack (indicated in red) intersects with a mesh node due to poor partitioning. The intersection is indicated by a blue square. B) The same node (indicated with a blue square) fails to split from its phantom node, causing a computational error.....	26
Figure 3.4 A close-up of the cement line mesh with element normal directions indicated by teal arrows. All cement line elements have a unique normal; however, only selected normal are shown for clarity ..	28
Figure 3.5 Model geometries used to represent an osteon in the radial direction. Modeled from Gustafsson et al. [108] .....	29

Figure 3.6 Trabecular profile with 20 distinct BSUs. Taken from [28] with permission ..... 30

Figure 3.7 Labeled geometry of the tiled BSUs showing all the adjustable parameters: specimen width (W), specimen height (H), BSU width (wBSU), BSU height (hBSU), cement line thickness (t), BSU wall angle ( $\theta$ ) and the location of the initial crack indicated in red with its partition highlighted in yellow..... 32

Figure 3.8 Example of how parameters  $X_{DIS}$  and  $Y_{DIS}$  affect the partitioning of the sample plate. A) Sample partitioned into BSUs without the use of  $X_{DIS}$  and  $Y_{DIS}$  parameters. B) the same partitioning with  $X_{DIS}$  set to  $5\mu\text{m}$  and  $Y_{DIS}$  set to  $10\mu\text{m}$ . The BSU that was generated first is highlighted in yellow. Note the interaction between the initial crack and the partition geometry. .... 32

Figure 3.9 examples of BSU geometries that can be generated with the python script. As mentioned above,  $t=5\mu\text{m}$  for these and all other models in this study. The trabeculae plate sample dimensions are constant at  $300\times 300\mu\text{m}^2$ . With  $X_{DIS}$  and  $Y_{DIS} = 25\mu\text{m}$ ..... 33

Figure 3.10 A sample showing the boundary conditions used in this study, with the initial crack highlighted in red. .... 34

Figure 3.11 A test sample with the simulated crack propagation highlighted in red. 4 separate strain reading were taken at different time steps. The blue triangles indicate the locations of the crack tip at the point when readings were taken. **(1)** time increment 219; strain at top edge  $4.13\times 10^{-3}$ . **(2)** time increment 301; strain at top edge  $4.19\times 10^{-3}$ . **(3)** time increment 380; strain at top edge  $4.96\times 10^{-3}$ . **(4)** time increment 484; strain at top edge  $4.96\times 10^{-3}$ ..... 35

Figure 3.12 Examples of a number of mesh analysis models meshed with different element sizes.  $3.5\mu\text{m}$  mesh was the biggest mesh size tested, while the  $0.5\mu\text{m}$  mesh was the smallest. The  $1.8\mu\text{m}$  mesh was selected as the primary mesh size for this study. Note that the images show only a small section of a model, to make the smaller mesh size more visible..... 36

Figure 3.13 A failed simulation where the crack looped back on itself instead of propagating through the sample. The crack path was highlighted in red. The view is zoomed in on a portion of the sample to provide a better visual of the crack path..... 37

Figure 3.14 A model from the first parametric study with  $\theta$  set to  $60^\circ$ . The enlarged area shows the location of the initial crack inside the BSU ..... 38

Figure 3.15 Comparison between real BSUs in a trabecula of a vertebral body taken from [28] with permission, and the idealized hexagonal BSUs that were used in the second parametric study. .... 39

Figure 3.16 Two models of the second parametric study partitioned with different size BSUs. A) BSU size  $15\times 75\mu\text{m}^2$  B) BSU  $75\times 375\mu\text{m}^2$ ..... 41

Figure 3.17 A sample with a  $50\times 250\mu\text{m}^2$  BSU size, where the initial crack is located inside the cement line. Note that the initial crack shifted off center to avoid perfectly mirrored symmetry..... 42

Figure 3.18 Two models with the BSU size  $75\times 375$ , representing the two extremes of the initial crack location A): Initial Crack located on the right side of the BSU, forcing the crack to propagate through the entire BSU before hitting the cement line. B) Initial crack located at the left side of BSU. The crack only needs to propagate through a couple of microns of BSU before it hits the cement line..... 43

Figure 4.1 Predicted crack paths in radial models with and without Haversian canals. Crack propagation was modelled using (A) the MAXPE criterion or (B) the new interface damage criteria for different critical interface strains. Taken from [116] with permission from Elsevier ..... 45

Figure 4.2 predicted crack path in radial models with Haversian canals using dual criteria method. A) Crack is deflected around the osteon via the cement line. B) crack path penetrates through the osteon. .... 46

Figure 4.3: Mesh size analysis plot of strain to complete crack propagation against the mesh size used in the simulation. .... 47

Figure 4.4 The image on the left (A) shows a finely meshed model where the crack deflects around the BSU through the cement line. The figure on the right (B) shows a coarsely meshed model where the crack propagated through the BSU rather than around it. .... 48

Figure 4.5: Plot of strain to full crack propagation over the BSU width  $w_{BSU}$  based on results from the second parametric study. .... 50

Figure 4.6: Plot of strain to full crack propagation over the distance the crack traveled in the BSU based on results from the second parametric study. .... 51

Figure 4.7 Plot of strain to full crack propagation over the distance the crack traveled in the BSU in three different BSU sizes. based on results from the second parametric study. .... 52

Figure 4.8 Plot of the strain response to change in crack path for different size ratios of BSUs. From left to right the crack path changes from deflection around the BSU to propagation through the BSU. .... 54

## List of Tables

Table 2.1 Collection of elastic modulus values of trabecular bone. Recreated from [61] .....	14
Table 2.2 Measurements of BSU parameters of the L2 vertebrae from 16 females including age, number of unaltered BSU measured (n), and their median BSU Area, BSU Thickness and BSU Length [95% CI]. Recreated from [73].....	15
Table 3.1 List of material properties used in this study.....	28
Table 4.1 list of strains required to propagate a crack through a sample of pure BSU material for samples with different heights 'H'.....	47
Table 4.2 Strain required for complete crack propagation [ $\times 10^{-3}$ ] for a range of BSU side angles $\theta$ at multiple QUADE strain values. The transition between the two crack propagation paths is shown with the use of different colors. ....	49
Table 4.3 Comparison of strain ( $\times 10^{-3}$ ) to complete crack propagation between different crack paths in five differently sized BSUs. Data for mixed propagation is taken from the first data set. ....	51
Table 4.4 A collection of strains ( $\times 10^{-3}$ ) at complete crack propagation for the crack paths through and around the BSU for different BSU aspect ratios. Note that images of the samples show the BSU partitions before the adjustment of parameter $Y_{DIS}$ . As such, the BSU partitions are not properly aligned to the initial crack location. ....	53

## Nomenclature

BSU	Bone Structural Units
$D$	Damage variable
DXA	Dual-energy X-ray Absorptiometry
$E$	Young's modulus
$f$	Fracture criterion
$G$	Energy release rate
FEA	Finite Element Analysis
FRAX	Fracture Risk Assessment Tool
$H$	Height of the sample trabeculae plate
$h_{BSU}$	Height of the BSU
LEFM	Linear Elastic Fracture Mechanics
MAXPE	Maximum principal strain (criterion)
MAXPS	Maximum principal stress (criterion)
QCT	Quantitative Computed Tomography
QUADE	Quadratic nominal strain (criterion)
QUADS	Quadratic nominal stress (criterion)
$t$	Thickness of the cement line
$\nu$	Poisson's ratio
$W$	Width of the sample trabeculae plate
$w_{BSU}$	Width of the BSU
$XDIS$	Horizontal partition displacement
XFEM	Extended finite element analysis
$YDIS$	Vertical partition displacement:
$\theta$	Angle of the BSU side walls relative to the horizontal line
$\varepsilon$	Strain
$\sigma$	Stress
$\varepsilon_{eq}$	Equivalent strain

## Acknowledgements

I would first like to thank my two supervisors: Dr. Brent Lievers and Dr. Krishna Challagulla. Thank you for approaching me with the opportunity to further my education. The start of the global pandemic was a stressful and uncertain period of time in my life and having a clear goal of getting a master's degree helped me get through those trying times. Thanks to your guidance and support I was able to achieve something that I thought I would never have the chance to do. Though the process of writing this thesis was made much harder by the global pandemic, I knew that I could always rely on my supervisors to provide me with everything I needed to continue working in a safe and friendly environment.

I would also like to thank my parents for not only supporting me throughout my studies, but also for making the difficult decision to immigrate to Canada, to provide a better life for my brother and me. I can only imagine how hard it was for you to leave everything behind and start over in a different country, and I will be forever grateful to you for providing me with a chance to get a high-level education. When I asked for advice on continuing my studies, you never hesitated and only encouraged me to take the next step. Thank you both for believing in me, and I hope to continue making you proud.

# 1 Introduction

## 1.1 Motivation

Bone is a remarkable material that is designed to handle large loads over extended periods of time without fracturing. Unfortunately, factors like ageing and bone diseases can significantly compromise the integrity of the bone, leading to a higher risk of bone fracture. It is estimated that one in three women and one in five men over the age of 50 worldwide will sustain an osteoporotic fracture [1].

Osteoporotic fractures are caused by osteoporosis, a condition in which bone becomes more fragile due to a decrease in bone density and degradation of bone structure on the microscale and mesoscale. Individuals with osteoporosis have a high risk of sustaining bone fractures due to minor falls or minimal physical activities [2]. As such, the economic costs associated with these fractures represent a major burden on health care systems and are only expected to rise as the populations of industrialized countries age over the coming decades [3]. For example, 2.05 million fractures were estimated to occur in 2005 in the United States, costing nearly \$17 billion in treatment and prevention. Furthermore, both the number of fractures and their associated costs are projected to grow by more than 48% by 2025 [4]. In addition to the economic costs, osteoporotic bone fractures also result in reduced quality of life and increased likelihood of mortality.

Bones differ drastically in strength and composition based on their location and function in the body. Bones containing large proportions of trabecular bone such as the hip, wrist, and spinal column are highly susceptible to fracture [4]. Trabecular bone is a light and porous bone tissue. It consists of a complex three-dimensional network of interconnected rods and plates called trabeculae. Trabecular bone, also known as cancellous bone or spongy bone, is usually surrounded by a protective layer of compact bone, which provides greater strength and rigidity to the overall structure [5, 6]. Due to ageing and degenerative bone diseases like osteoporosis, the trabeculae degrade over time by thinning or sometimes by disappearing entirely. This degradation causes a reduction in the overall bone mass of trabecular bone, making it more prone to fracturing [7]. Figure 1.1 shows an artistic representation of the overall structure of a trabecular bone and how it might change with age or degenerative bone disease.

An efficient, non-invasive method of assessment is needed to correctly identify and treat patients with a high risk of bone fractures. Osteoporosis is characterized by reduced bone mass, and as such, bone mineral density (BMD) tests are commonly used as a quantitative predictor of the likelihood of fracture [8, 9]. The most frequently used BMD test is the central Dual-energy X-ray Absorptiometry (DXA) test; however, other tests like quantitative computed tomography (QCT) can also be used to measure BMD [10]. The BMD value is most commonly compared to that of a healthy young adult and is given a T-score based on standard deviations away from the reference mean. A person with a T-score of 2.5 standard deviations below a healthy value is considered to have osteoporosis [11].

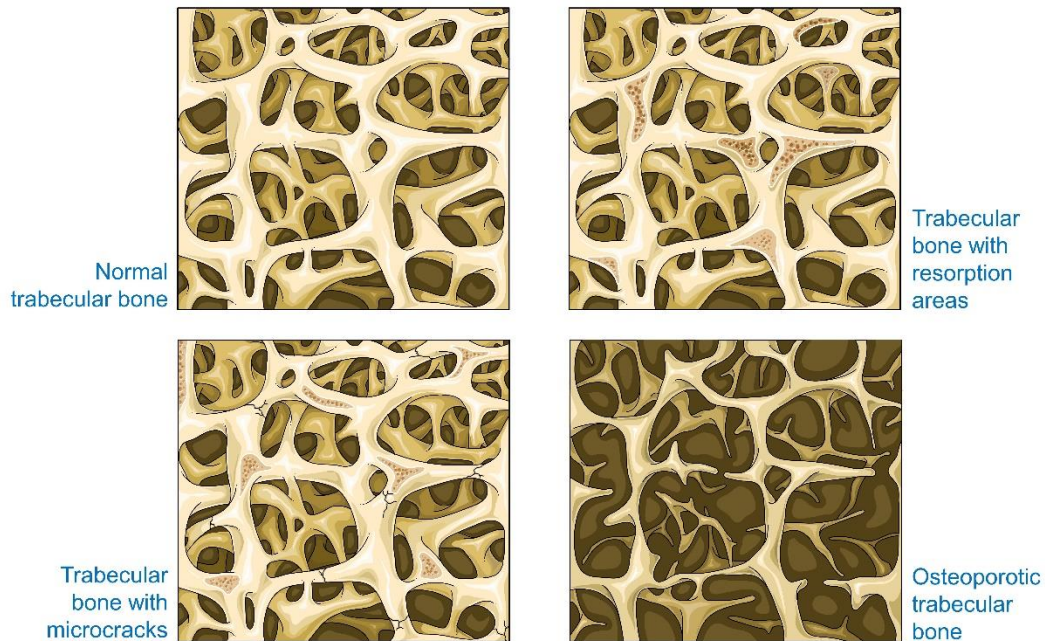


Figure 1.1 An example of trabecular bone structure. The figure shows possible degradation of trabecular bone due to aging and degradative bone disease. Taken from [123].

Unfortunately, using BMD as the only physical measurement of bone’s likelihood of fracture is not always sufficient. BMD tests identify only around one-third to half of the patients with a high bone fractures risk [12–14]. BMD is an essential factor in bone’s resistance to fracture; however, it is not the only factor. Properties like bone structure and trabecular composition also change with age and can potentially increase fracture risk in older people. The BMD tests are not always reliable because the tests only identify the density of the bone, but they tell us nothing about the bone’s quality or structure. New methods must be developed that consider the quantity of bone and its quality if we are to improve the process of identifying the level of fracture risk in patients.

Other assessment tools exist that use BMD as part of a more in-depth investigation to predict an individual’s risk of bone fracture more accurately. For example, the Fracture Risk Assessment Tool (FRAX) developed by a research group at the University of Sheffield uses BMD with a combination of other factors to predict the risk of fractures in a person with osteoporosis. A FRAX score estimates the probability of a hip, arm, or spine fracture within the next 10 years by providing a percentage value that indicates the risk. Some factors include age, weight, height, history of fractures, smoking and drinking [15, 16]. It is important to note that although FRAX uses 12 factors to determine risk, BMD is the only parameter that looks at the physical properties of the bone.

Trabecular bone is a hierarchical material which is structured on multiple length scales to protect against fractures (Figure 1.2). It achieves this objective by implementing efficient mechanisms that prevent crack growth by redirecting cracks, bludgeoning crack tips, and quickly repairing existing microcracks [17, 18]. With age, the structure of bone undergoes significant changes at various hierarchical levels which can increase the fracture risk. For example, all bones are composed of a mineral and collagen

composite on the nanoscale. With age, the collagen properties degrade, and the composite gets more mineralized, becoming more brittle [19, 20]. While on the mesoscale (Figure 1.2), the trabeculae degrade over time, becoming thinner, or disappearing entirely [21, 22]. This degradation, in turn, leads to a decrease in the bone volume fraction and the trabecular connectivity [23–25]. Although BMD measures do reflect the overall loss of bone, they cannot detect for architectural or other changes to the trabeculae.

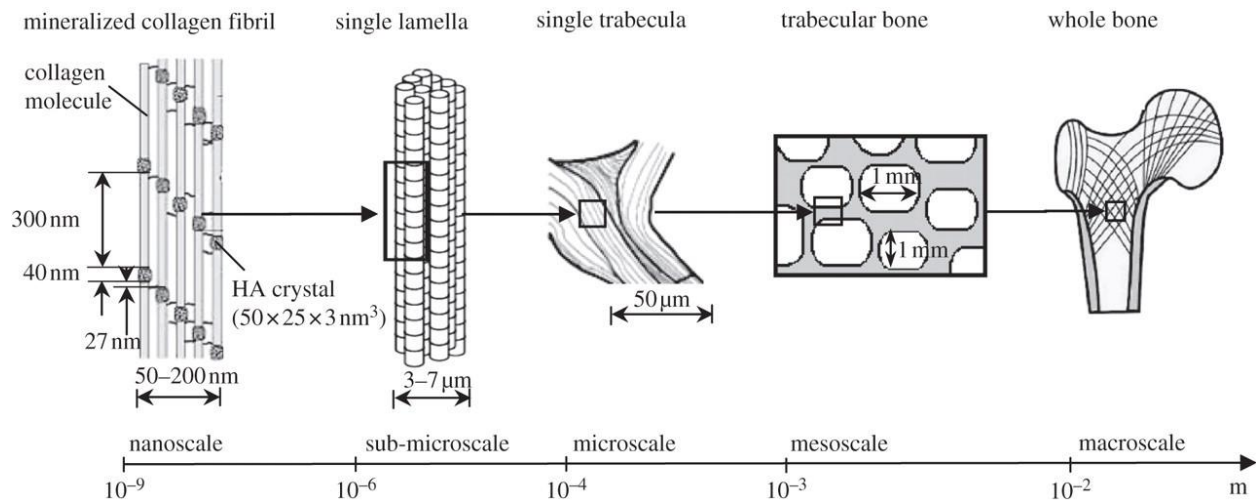


Figure 1.2 Hierarchical structure of trabecular bone. Taken from [26] with permission from *Journal of The Royal Society Interface*

On the microscale, trabeculae consist of bone structural units (BSU) which are surrounded and joined together by a thin layer of material called cement line (Figure 1.2). New BSUs are generated and regenerated due to a process known as bone remodelling, which continuously occurs throughout the person’s lifetime. The remodelling process involves one set of cells known as osteoclasts destroying old bone, while a different set of cells known as osteoblasts rebuilds the missing bone with new tissue. The remodeling process is depicted in simplified form in Figure 1.3 [27]. The newly remodelled patch of bone tissue is usually surrounded by a highly mineralized material called cement line [5]. It has recently been discovered that the overall size (thickness, length and area) of BSU, as measured in 2D, decreases with age [28]. As the average number of BSUs per unit area increases, the proportion of cement line contained within the trabeculae as the interface area between the BSUs also grows [28]. This increase in the proportion of cement line in the trabeculae might play a role in reducing the bone’s ability to resist crack propagation, increasing the risk of trabecular bone fracture.

Cement lines are thought to be more mineralized and less collagenated than the adjacent BSU [29]. This combination of properties causes the cement lines to be stiffer and more brittle, making them ideal for crack deflection. Previous studies have shown that cement lines in cortical bone tend to deflect cracks around the osteons [30, 31]. This cortical bone crack deflection is considered beneficial, as it forces the cracks to propagate further and expend more energy before a complete fracture can occur [5]. Cortical bone and trabecular bone have different structures and compositions; however, they both contain cement lines that become more numerous with age. It is hypothesized that cement lines in trabecular bone can also deflect cracks, increasing the bone’s ability to resist fracture.

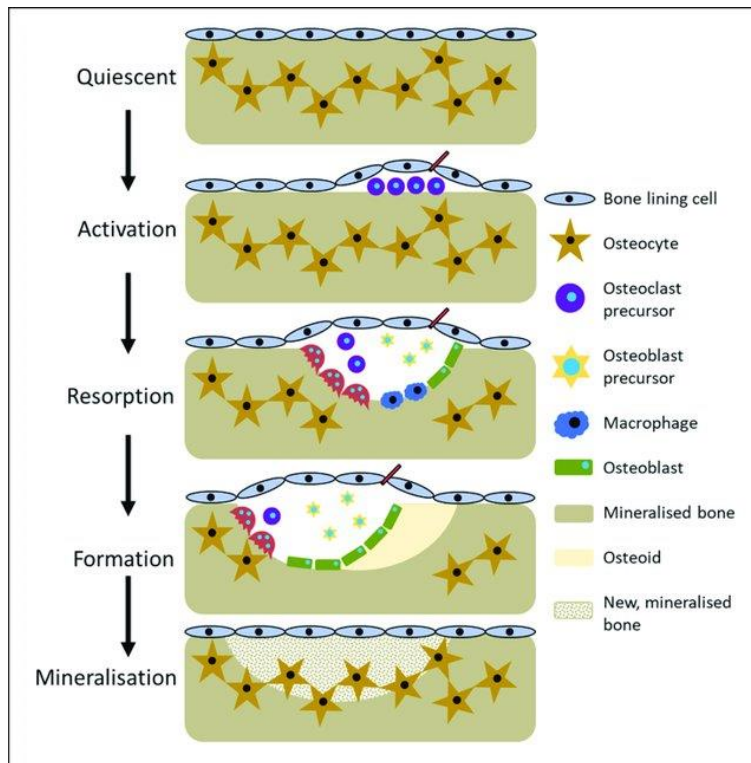


Figure 1.3 Simplified diagram showing the five stages of bone remodelling. Taken from [27] and reprinted under (CC BY).

This hypothesis is difficult to test experimentally, as physical tests on the microscale are expensive and labor intensive. Fortunately, we can use Finite Element Analysis (FEA), in combination with years of previous bone research, to simulate crack propagation in trabecular bone. The use of FEA can not only provide valuable insight into the significance of the microstructural changes of trabecular bone due to age, but also help us develop new more reliable tool to identify high risk of fracture.

FEA modeling is a wide field of study. As such, there exists a plethora of ways to evaluate crack propagation in trabecular bone. A number of previous studies use parameters like tissue strength to model bone [32, 33]; however, it might also be important to consider other parameters like fracture toughness and fatigue strength to create a comprehensive fracture risk analysis model. While strength describes failure from a single large load, toughness considers failure at moderate loads with pre-existing damage, and fatigue strength describes failure due to repetitive cyclic loads that are experienced in every day life [34]. All three parameters mentioned above are valid and require in-depth study; however, this thesis will only focus on studying how age-related changes in the microstructure of trabeculae affect crack propagation. The crack propagation will be simulated with the use of the extended finite element analysis (XFEM) damage model implemented through ABAQUS 2020. This damage model was chosen based on previous studies that will be discussed in the literature review section of this thesis.

## 1.2 Aim and objectives of the study

This thesis aims to analyze the effects of age-related microstructural changes on crack propagation in trabecular bone using XFEM modelling. The specific objectives are to:

1. implement a numerical interface damage model, previously used in the study of cortical bone, to accurately simulate crack propagation in a 2D sample of trabecular bone;
2. identify the critical values for the interface damage model that cause the crack to propagate around the BSU via cement lines rather than through it;
3. investigate how cement line deflections in trabeculae affect the microscopic strain to failure; and,
4. determine if the age-related reduction in the BSU size slows or accelerates crack growth in trabeculae.

## 2 Literature review

### 2.1 Chapter introduction

The literature concerning the structure of trabecular bone and crack propagation modelling through bone was reviewed and summarized in this section. The literature was reviewed to provide the necessary background to better understand the methods and the results developed in this thesis.

The objective of this study is to use numerical methods to identify the role the cement lines play in terms of providing crack resistance to the trabeculae, and to better understand how changes in BSU size might affect crack growth in the trabeculae. To accomplish this goal, the following topics were reviewed in this chapter.

First, bone composition and physical properties are reviewed, focusing on the macro and micro length scales of the bone structure. Though this thesis investigates crack propagation in trabecular bone, much of the existing crack modelling work is done in cortical bone. As such, the literature on cortical and trabecular bone is reviewed to provide an understanding of the similarities and differences between the two types of bone tissue. The lack of literature on bone properties is also discussed to justify the assumptions and estimations that were made in this thesis.

Next, the crack modelling literature is reviewed to establish known methods of simulating crack propagation through bone-like materials. This thesis focuses on understanding how remodelling of trabecular BSUs over time affects the overall resistance of crack propagation in trabecular bone. To show why this research is needed, this section also emphasizes the relative lack of research in the field of crack propagation through the trabecular bone on the microscopic level.

This review aims to provide a complete overview of the current knowledge of trabecular bone and point out the gaps in the knowledge, which, if studied, can improve our knowledge of the mechanisms that trabecular bone uses to improve its resistance to damage like microcracking.

### 2.2 Overview of bone

The term bone refers to a set of organic calcified tissues primarily composed of mineralized collagen fibrils. Though bone is a broad term that encompasses many different skeletal structures, it is also closely related to other calcified tissues like dentin and enamel in teeth. These tissues are composed of similar materials; however, each is structured and proportioned in a specific way to provide appropriate material properties based on the tissue's required mechanical function.

Bone is a composite material that consists of an organic, type (I) collagen matrix imbued with nanocrystalline carbonated apatite. The mineral provides stiffness to the matrix, while collagen provides resilience and ductility. These basic materials are arranged in well-defined hierarchical structures, ranging from the sub-nanoscale to the macroscale [35]. Most bone tissues are constructed using the same basic mineralized collagen fibrils; however, the higher-level hierarchical structure of bone and its material composition depends on the type of bone and its mechanical function in the body.

The hierarchical structure of the bone is well depicted in . As the bone tissue ascends the hierarchical levels, the structure becomes more intricate, and the calculations of the mechanical properties of the tissue become more complex. Though each hierarchical level is important to the overall strength and

fracture resistance of bone, this thesis focuses on the macrostructure and microstructure levels to reduce the overwhelming complexity of the subject.

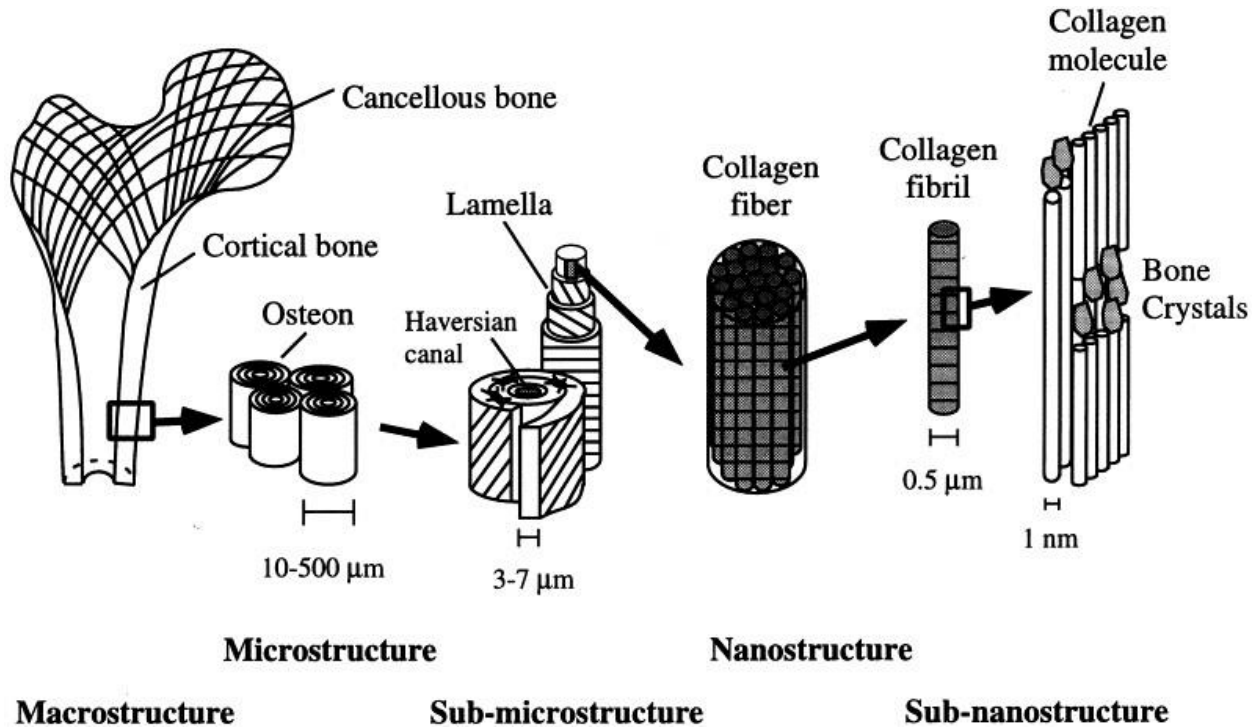


Figure 2.1 Hierarchical structure of bone. Taken from [36] with permission from Elsevier

### 2.2.1 Hierarchical structure of bone

The mineralized collagen fibrils are the basic building blocks of bone. The fibrils are approximately 0.5 μm in diameter and are created by collagen forming a matrix that is then impregnated with mineral crystals [37]. The mineral crystals provide stiffness to the bone, while the collagen matrix provides toughness and ensures proper structure. The proportions of the two materials are usually related to the function of the bone, with higher mineral content associated with higher stiffness and lower toughness [38].

One step higher on the hierarchical structure scale, the collagen fibrils are combined to form collagen fibers and then packed into planar lamella sheets. The lamella sheets are anisotropic; however, they are usually stacked together in a layered plywood-like pattern with the plate fibrils oriented in alternating directions. The lamella sheets are then structured based on the type and function of bone tissue they are creating. The lamellae are formed into two different tissue types at the microscale: trabecular (spongy/cancellous) bone and cortical (compact/dense) bone. In trabecular bone the lamella sheets form into packets known as bone structural units (trabecular packets/hemioosteons), and in the cortical bone the sheets are wound around each other creating structures known as osteons. On the macroscale, cortical tissue makes up the hard outer shell of the bones, while the trabecular bone tissue is used to form the porous internal structure of bones.

Groups of lamellae are usually sheathed in a thin layer of highly mineralized bone tissue known as the cement lines. It is widely believed that the size and volume fraction of cement line in bone greatly

affects the bone's overall mechanical properties [39], and is of great interest in this study. As such, cement lines will be further discussed later in this section.

### 2.2.2 Cortical bone tissue

Though this thesis focuses on modelling crack propagation through trabecular bone, many of the modelling methods discussed in the next section were created for simulating crack propagation through cortical bone or tested using models of cortical bone. As such, it is essential to review the basic similarities and differences between trabecular and cortical bone.

On the macroscale, cortical bone has a dense and solid structure. Due to its properties, it is also sometimes referred to as compact bone. Cortical bone is used to provide strength and stiffness to the overall structure of the skeleton. Cortical bone also covers the outside of the skeleton to protect the weaker bone tissues, like the trabecular bone. On the microscopic scale, cortical bone consists of lamellar sheets that are wound concentrically around blood channels (voids), also known as Haversian canals, to create structures known as osteons. These tubular osteons are considered the main structural units of cortical bone tissue and are the main vascular channels that penetrate the compact bone tissue. Other smaller channels, known as Volkmann canals, run perpendicular to the Haversian canals and interconnect the channels into an extensive network. Osteons are embedded in an interstitial matrix and are usually enclosed by a thin interface called the cement line or cement sheath, which separates the osteon from the rest of the matrix. shows the lamellar structure of cortical bone around multiple osteons.

It is believed that osteons play a key role in preventing crack propagation through bone. The cement lines tend to deflect the crack paths around the osteons rather than allowing the crack to break through them. The extended crack path and sudden change in direction caused by the cement lines make the crack lose more energy forcing it to terminate early. If the crack breaks through the osteon, it becomes blunted in the Haversian canals, again losing much of its energy. Several papers were published trying to model crack propagation through osteons due to its unique properties. Some of the papers will be reviewed later in the crack modelling section.

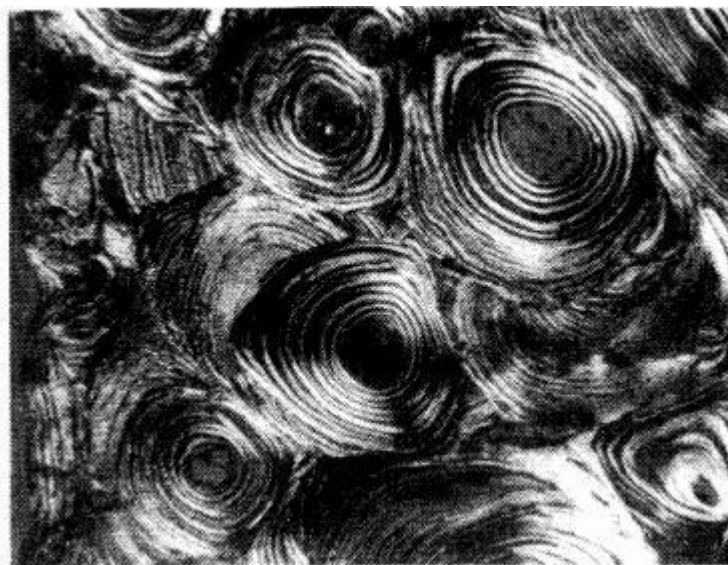


*Figure 2.2 Photomicrograph of the lamellar structure of cortical bone. Taken from [40] with permission from The Lancet*

### 2.2.3 Trabecular bone tissue

Trabecular bone is a porous bone tissue located at the ends of long bones and in vertebral bodies. As mentioned before, in trabecular bone, lamellae are aligned tangentially to the outer surface of the bone. The resulting semi-crescent lamellar structures are known as BSU, hemiosteons, or trabecular packets [28]. BSUs are formed into a series of interconnecting rods and plates known as trabeculae. In the trabeculae, the BSUs are separated by cement line material in a brick-and-mortar type fashion. This structure can be seen clearly in . The microscopic scale of the trabeculae is the only scale of interest in this study. The work done by Lamarche [28] documents morphometric changes with age in human BSU in the lumbar spine. In her thesis, Lamarche shows that BSU size tends to decrease with age, as the damaged BSU gets remodelled into multiple smaller BSU, as shown in . This change in size over time of the BSU is hypothesized to affect the overall fracture resistance of the trabecular bone.

On the macroscale, the trabeculae of trabecular bone are arranged into extremely complex 3D structures to provide maximum load transfer while reducing the overall mass of the bone. The complex structure of trabecular bone is shown in . In most cases, the trabecular bone is architecturally optimized for maximum load transfer with minimal weight. With age, a loss of trabecular bone mainly occurs by thinning or complete removal of trabeculae [41]. These bone density losses usually occur due to degenerative bone diseases like osteoporosis [42].

There is a significant amount of research on macroscopic changes in the trabecular bone architecture due to ageing and degenerative bone disease [9, 12, 13, 23, 43]. However, little is known about the effects of microscopic changes in the trabecular bone due to ageing and the remodelling process.

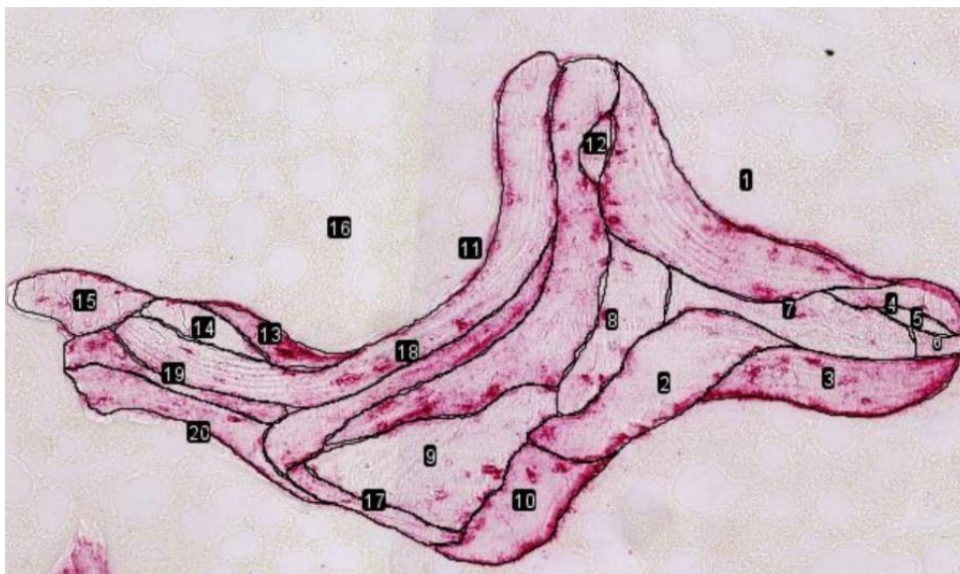


Figure 2.3 Trabecular profile with 20 labeled BSU and outlined cement lines. Taken from [28] with permission

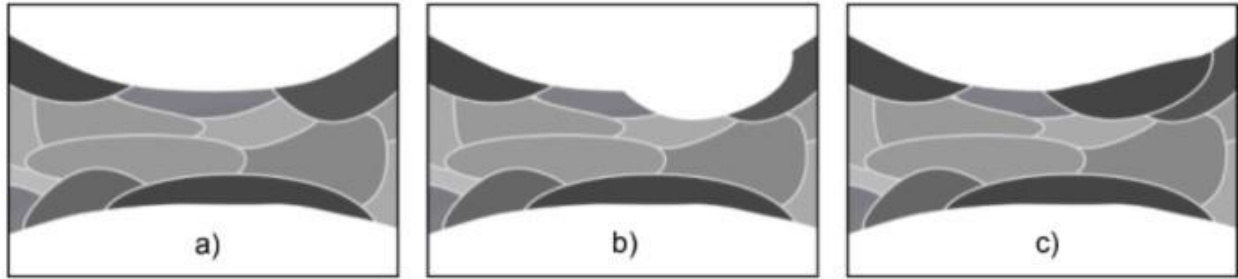


Figure 2.4 From left to right: (A) A trabecula consisting of a patchwork of new and old BSU, separated by cement line (white), (B) a portion of bone is resorbed by remodeling cells, (C) new bone is laid down in the resorbed portion. Taken from [28] with permission

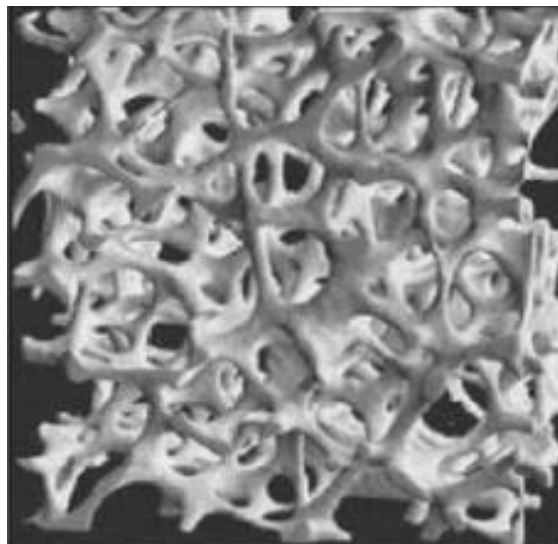


Figure 2.5 Vertebral trabecular bone architecture. Taken from [44] with permission from Elsevier

#### 2.2.4 Bone remodeling

Throughout a person's life, their bones undergo physical changes known as bone remodelling. As parts of old bone get destroyed or damaged, new bone is deposited to replace the old bone and repair the damage. Bone remodelling can also occur as the bone adjusts to new or unusual loads. The initiation of the remodelling process is a heavily studied topic; however, little is known about how the bone knows where it is damaged and when to start remodelling. In any case, the lack of knowledge in this area of study should not be a concern as it is outside the scope of this research.

The remodelling process is accomplished with the help of two different types of cells known as osteoclasts and osteoblasts. Osteoclasts attack a specific portion of the bone to start the remodelling process, dissolving it in the process. After a portion of bone is destroyed, the osteoclasts disappear, and osteoblast cells establish a new organic matrix that is then mineralized into a new BSU.

Bone remodelling plays a significant role in how bone properties change over time. For example, at the architectural level, remodelling causes the trabecular thinning or perforation that is known to reduce the strength of trabecular bone. Remodelling is also responsible for generating the patchwork of trabecular BSU at the microstructural level. Over time new packets become noticeably smaller and,

through discrete modelling events, decrease the size of pre-existing BSU. Also, smaller BSUs also increases the amount of cement line in the bone, as more trabecular packets create more boundary layers. This process and the changes in human trabecular BSU are described in detail in the study done by Lamarche [28]. shows the steps for remodelling trabecular bone and how it affects the overall structure of the bone.

#### 2.2.5 Cement lines

The structure of trabecular bone can be compared to a brick wall, where BSUs are the bricks, and the cement lines are the mortar that fills the gaps between BSUs and keeps them fastened together. New cement lines are generated during remodelling in the trabecular bone as boundaries between new and old bone tissue. The effects of the increase in volume fraction of cement lines in trabeculae are unknown and are the focus of this thesis. However, based on studies on cement lines in the cortical bone, we can hypothesize the effects of cement lines in trabecular bone.

The importance of cement lines in preventing crack propagation in cortical bone is well known and is discussed in many studies [45–52]. When a crack propagates through bone, it takes a path of least resistance. Such paths usually appear along the cement lines since cement lines are more brittle and more susceptible to cracking. The idea that cement lines are areas of weakness was demonstrated well by F. Gaynor Evans in his 1976 paper [47]. In his work, Evans shows a decalcified cross-section of cortical bone from the unembalmed fibula of a 56-year-old Caucasian man, which was accidentally fractured during mounting on a slide. The propagation of cracks occurred along the cement lines, as seen in . Similar results were also observed in work by Evans and Bang [46], where fractures produced in transverse sections of decalcified specimens by applying tension showed a tendency to follow the cement lines. A similar tendency was observed when a section of cortical bone was allowed to dry. During the drying process, the stresses and strains inside the bone resulted in crack formation along the cement lines.

Even though cement lines are considered to be less resistant to cracking than the surrounding bone, their unique properties and geometry may help prevent the complete separation of bone during crack propagation. Cement lines deflect and bludgeon cracks, forcing them to consume more energy as they take longer and more convoluted paths through the bone. In some cases, cement line deflections allow the bone to withstand higher strains without reaching a complete failure state. The resulting partial cracks are much easier to restore via the remodelling process. Though the benefits of cement lines in cortical bones are well established [6, 39, 51, 53], the cement lines' composition and mechanical properties are still disputed today. Cement lines are extremely thin structures; their thickness ranges from 1 to 5  $\mu\text{m}$ . This scale makes it challenging to quantify the material properties of cement lines with ordinary procedures. Though this thesis uses the more popular assumption that cement lines are highly mineralized, there exists literature that describes cement lines as being softer than the surrounding bone. Some of the literature for both sides of the argument will be summarized below.

In one example, Montalbano et al. [54] used nanoindentation to find the elastic modulus and hardness of the ovine and bovine cement lines in compact bone. The study results show that the cement lines in the ovine and bovine samples were approximately 30% softer and more compliant than the surrounding bone. A study by Frasca [55] used scanning electron microscopy to analyze adult human bone that was decalcified and stained. The samples were compressed between glass slides to create a partial mechanical disruption, after which they were observed under a scanning electron microscope. The

cement line regions were found to contain large concentrations of amorphous ground substance, which was distinct from the collagen fiber bundles observed in collagen-rich lamellae. Burr et al. [56] suggested that cement lines had reduced mineralization compared to the surrounding bone tissue and were ductile in nature [56].

On the other hand, a different nanoindentation study by Gupta et al. [57] showed that the indentation modulus increased abruptly at the cement line, while being constant across the osteon. This and other recent studies report that the cement lines are hyper-mineralized or collagen-deficient relative to the surrounding bone, meaning they have a higher mineral content than the surrounding bone tissue [29, 58, 59]. Though the osteonal bone tissue differs in properties from that of trabecular tissue, it is likely that the property variation between the cement line and the BSU should be similar.

As mentioned before, there is no consensus about the stiffness of the cement line. As such, there exist two opposite hypotheses that try to describe the stiffness of the cement line. The first hypothesis describes the cement line as a viscous interface that attracts cracks. The second hypothesis describes the cement line as a highly mineralized brittle material. However, regardless of the cement line's stiffness, the interface between the two materials is usually considered weak to fracture. This property makes cement lines ideal for crack deflection. Dong et al. [60] devised a method to test the interface between the cement line and the rest of the bone material. In the study, a push-out test was performed on an osteon in compact bone. This test measured the shear strength of the interface between the cement line and the surrounding cortical bone. The results show that the shear strength at the cement line interface is significantly weaker than the rest of the tissue. The cement line interfacial strength ranged from 5.38 MPa to 10.85 MPa, while other tissue in the bone ranged from 45.97 MPa to 93.74 MPa [60].

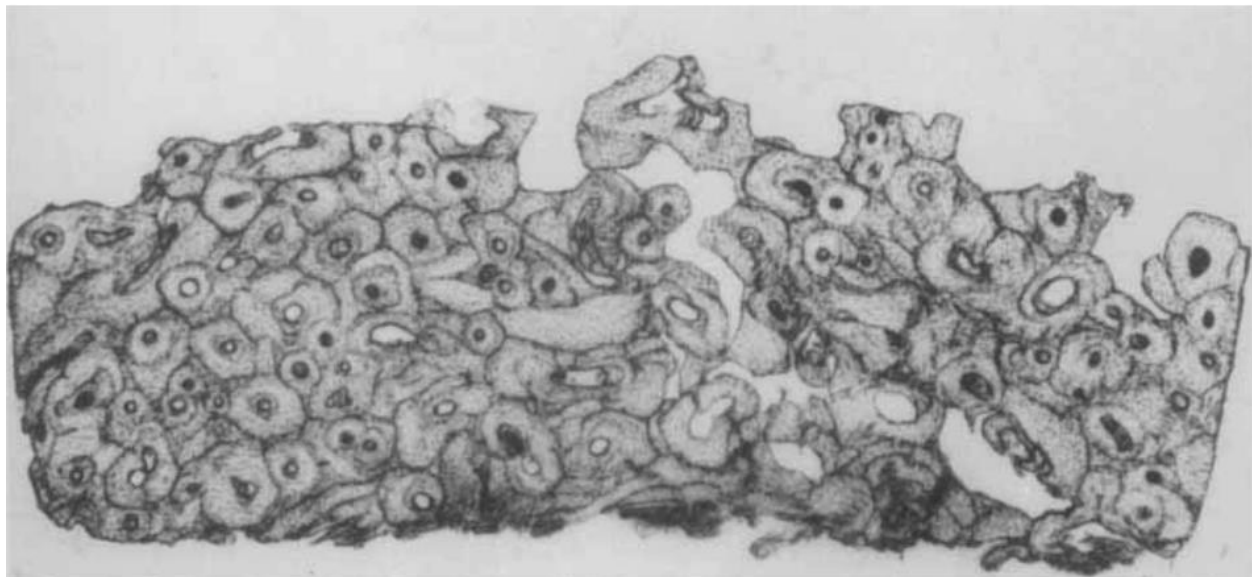


*Figure 2.6 Cross section of fractured cortical bone taken from. Note tendency of crack propagation along the cement lines. Taken from [47] with permission*

### 2.2.6 BSU properties

A significant amount of research has been done on the elastic modulus and hardness properties of trabecular bone. The trabecular bone review paper by Oftadeh, et al. [61] has gathered many of the values that researchers produced over the years. The paper provides values for multiple testing techniques like FEA analysis in conjunction with experimental testing, buckling, ultrasonic, and nano-indentation. Some of the nano-indentation test values are presented in Table 2.1. Out of the given list of testing techniques, the nano-indentation section is reviewed more in-depth as it represents the elastic modulus of specific BSUs and not the entire trabecular structure. From initial inspection, the elastic modulus values appear to fluctuate between 10-20 GPa; however, many of the nano-indentation tests are done on dried bone due to the nature of the test. Dried bone is known to have a larger elastic modulus than wet bone. Therefore, the values should be adjusted if they are to be used in crack propagation simulations. It might be useful to refer to the work of Townsend et al. [62], who found that drying the trabecular bone increased Young's moduli of trabeculae by about 24%. Though newer studies by Lievers et al. [63] suggest that when the increase in tissue modulus is considered together with the decrease in the bone volume fraction, the increase in the modulus of cancellous bone following dehydration should be close to 14%. If the same factor applies to nano-indentation, the elastic modulus values should be around 8.5-17 GPa.

Table 2.1 Collection of elastic modulus values of trabecular bone. Recreated from [61]

Reference	Bone Type and Location	Tissue Modulus (GPa)
[64]	Human femoral neck	11.4 ± 5.6
[65]	Human distal femur	18.1 ± 1.7
[66]	Human vertebra	13.4 ± 2.0
[67]	Human femoral head	21.8 ± 2.9
	Human femur trochanter	21.3 ± 2.1
[68]	Human distal radius	13.75 ± 1.67
	Human vertebrae	8.02 ± 1.31
[69]	Porcine femur	21.5 ± 2.1
[70]	Human tibia/vertebrae	19.4 ± 2.3
[71]	Sheep proximal femur	20.78 ± 2.4

Trabecular packets vary in both length and thickness depending on the location from where the sample was taken, and the age, gender, health, and size of the donor. A study by Lips, et al. [72] recorded the mean wall thickness of the trabecular bone packets in the human iliac crest in 14 female and 22 male subjects of varying age. The mean wall thickness was measured to be  $49.7 \pm 8.7 \mu\text{m}$  at a mean age of 50.9 years. The study also found a relationship between age and the mean wall thickness. This result is not surprising and is most likely caused by the remodeling of the trabecular bone that occurs with age. shows a graph of the Lips' results as mean wall thickness with respect to age. It is also important to note that there are many outside factors like sex, skeletal site, and disease that can influence the size of the packets. Lamarche et al. [73] has also provided an extensive list of BSU measurements from frontal sections of L2 vertebrae from 16 females of widely varying ages (see Table 2.2). Though both the BSU thickness and BSU length are shown to have a large range of sizes, on average the BSU length appears to be 4 to 5 times larger than its thickness. This aspect ratio, along with the BSU thickness and length values reported by Lamarche et al. [73], will be the primary reference for the BSU size in this study.

Table 2.2 Measurements of BSU parameters of the L2 vertebrae from 16 females including age, number of unaltered BSU measured (n), and their median BSU Area, BSU Thickness and BSU Length [95% CI]. Recreated from [73]

<b>Age</b>	<b>n</b>	<b>BSU Area (<math>\mu\text{m}^2</math>)</b>	<b>BSU Thickness (<math>\mu\text{m}</math>)</b>	<b>BSU Length (<math>\mu\text{m}</math>)</b>
<b>18.5</b>	202	7770 [6497-9647]	45.1 [40.5-52.0]	248 [228-282]
<b>21.4</b>	278	8528 [7474-9941]	45.1 [41.2-49.4]	291 [270-310]
<b>21.7</b>	300	9873 [7884-11567]	51.0 [45.7-54.3]	268 [246-305]
<b>26.2</b>	305	5293 [4067-6344]	34.0 [31.3-38.1]	194 [178-230]
<b>30.2</b>	340	7166 [6407-7949]	47.2 [45.2-52.2]	204 [186-225]
<b>35.7</b>	319	6894 [6163-7943]	42.1 [39.8-43.8]	243 [218-260]
<b>36.2</b>	385	5777 [5115-6452]	41.9 [40.5-44.1]	182 [168-199]
<b>37.6</b>	262	10929 [9224-12592]	57.3 [53.5-62.2]	258 [224-292]
<b>69.1</b>	232	3698 [3103-4107]	32.1 [28.6-34.6]	153 [138-170]
<b>71.6</b>	195	7145 [5690-8338]	49.2 [44.9-54.6]	210 [187-238]
<b>73.5</b>	181	4071 [3431-5152]	33.5 [29.0-36.2]	167 [134-202]
<b>77.3</b>	189	6774 [5570-8046]	39.4 [36.0-43.0]	228 [197-258]
<b>78.0</b>	260	3839 [3220-4447]	33.6 [31.8-36.4]	161 [149-180]
<b>83.0</b>	233	3678 [3408-4730]	33.9 [31.2-36.7]	157 [145-173]
<b>85.8</b>	321	3222 [2859-3656]	29.2 [27.6-30.9]	161 [150-178]
<b>96.4</b>	228	6522 [5648-7463]	44.7 [40.6-47.8]	210 [188-233]

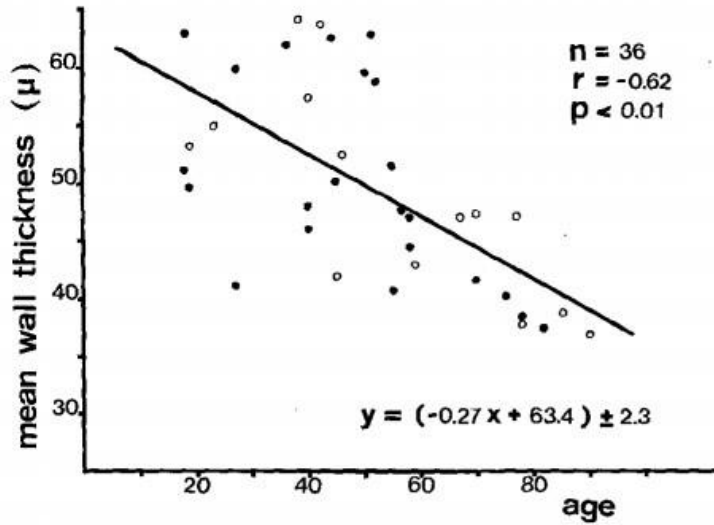


Figure 2.7 Regression line of the mean wall thickness of trabecular bone packets with advancing age. Taken from [72] with permission from Springer Nature

## 2.3 Modeling crack propagation in bone

There are two distinct categories of numerical damage models: continuous and discrete damage models. Furthermore, there exist two different approaches to modelling. There are strength-based models, like the Rankine criterion, and energy-based models, like the criterion for interface damage by He and Hutchinson [74]. The two approaches were also combined into the cohesive damage models proposed by Barenblatt [75]. This section will go over the most commonly used damage models for studying bone damage, and review literature that used these models to simulate crack propagation in bone. Only studies using finite element methods will be considered.

### 2.3.1 Continuum damage models

Continuum damage models use a broad damage approach to describe the crack without considering its exact topology.

#### 2.3.1.1 Scalar damage models

Scalar damage models, also known as element deletion, use a damage variable  $D$  that represents a fraction of damaged material in a cross-section of a body. A value of  $D = 0$  represents a body with zero damage, while  $D = 1$  represents full separation. The simplest constitutive stress-strain relationship can be written as:

$$\sigma = (1 - D)E\varepsilon \quad (1)$$

where  $E$  is the Young's modulus. In a simplified form, a finite element is considered failed once the equivalent strain reaches the failure strain i.e.

$$\begin{cases} D = 0; \varepsilon_{eq} < \varepsilon_f \\ D = D_c; \varepsilon_{eq} \geq \varepsilon_f \end{cases} \quad (2)$$

where  $\varepsilon_{eq}$  is the equivalent strain of choice and  $D_c$  is the critical damage. It is common to keep  $D_c < 1$  to ensure that there is no complete element deletion to avoid numerical errors.

The element deletion method is robust and can be used in a wide range of modeling. However, the method has some quirks that make it unreliable in a few situations. Element deletion has a high mesh sensitivity. Since the method “deletes” elements, the section affected by the crack directly corresponds to the size of the element. Similarly, the dissipated energy is also closely related to the mesh size for the same reason [76]. Unrealistic crack paths can appear due to mesh size and structure and, as such, special care must be taken when meshing the models [77]. This mesh dependency can be overcome by introducing a characteristic length in a non-local damage formulation [76, 78]. Another difficulty with this method is that the material softening from element deletion can cause numerical convergence problems, which makes simulating full crack propagations a challenge [79].

Scalar damage models have been used in a number of studies of crack propagation in bone on multiple size scales. At the macroscale, the proximal femur was simulated using both 2D projections and full 3D models in multiple literatures [79–83]. At the microscale, crack propagation was simulated in cortical bone (Figure 2.9 A) to estimate the critical energy release rate of cement lines [84].

#### 2.3.1.2 Phase-field models

Phase-field models are based on Griffith’s theory for brittle fracture in solids. Phase-field models propagate cracks with the use of energy release rate critical values. These models improve on Griffith’s theory by predicting crack initiation with the use of variational methods on energy minimization [85–87]. Phase-field models can branch existing cracks or nucleate new cracks during simulation. The cracks in these models are described by a phase-field that varies between 0 and 1 for intact and damaged material. The idea of the phase field method is to represent fracture as a continuum entity with a finite width where the stiffness of the material is greatly reduced. In this way, the crack can be represented without the need to explicitly track the discontinuity [88].

There exist several studies that use scalar damage models for biomechanical applications in the literature. A number of studies used the model to simulate damage in soft tissue [89–91]. A study done by Wu et al. [92] showed fracture modeling of brittle biomaterials with the use of the phase-field method on the macroscale. Shen et al. [88] demonstrated the use of the method in simulating crack propagation in long bone on the organ scale (Figure 2.9 B). A recent paper by Gustafsson et al. [93] evaluated a number of recent implementations of the phase field methods to find the best approach for simulating crack growth in bone tissue. Though the phase-field models show great potential due to its capability of capturing complex cracking phenomena, it is still not well-established in the field of biomechanics, particularly as applied to bone.

#### 2.3.2 Discrete damage models

Discrete damage models simulate cracks as a discontinuity that is embedded in a continuum [78].

##### 2.3.2.1 Cohesive element models

Cohesive element models use special interface elements that are inserted between solid elements in the model. The degradation of the cohesive elements is governed by a traction-separation law and are used

to simulate the crack propagation path. The manual insertion of cohesive elements makes this method ideal for simulation where the crack path is already known or can be easily estimated.

Cohesive elements have been used to study bone mechanics in several ways. At the nanoscale, this method was used to evaluate damage at the collagen-mineral interface and describe the damage at the interface of non-collagenous proteins due to tensile and compressive loads [94, 95]. On the microscale, cohesive elements have been used to simulate crack propagation in cortical bone in 2D. An osteon was modeled, and two different crack paths were set up (one through the osteon, and one round it) to study the effect of crack path on the crack resistance of the microstructure (Figure 2.9 C) [96]. A similar approach was also used to simulated deflection or propagation in dentin [97]. Other studies have attempted to simulate crack propagation without providing a pre-existing crack path by inserting cohesive elements between every solid element [98, 99]. Unfortunately, cohesive element models are not well optimized for such an approach, and as such, they are known to be mesh dependent and unreliable [100]. At the macroscale, the use of cohesive element modeling becomes difficult as the crack path is usually unknown and cannot be predetermined in these kinds of simulations. A few examples in literature of macroscale simulations show oversimplified models with numerous estimations [101, 102].

### 2.3.2.2 XFEM modeling

The extended finite element method (XFEM) is a numerical approach based on the generalized finite element method and the partition of unity method that was introduced by Belytschko and Black [103] as a finite element method with minimal remeshing. It enhances the basic FEM approach by adding discontinuous functions to the solution space for the solutions to differential equations. This method is commonly used to simulate crack propagation through an object or a material. Unlike other traditional finite element methods, crack location in XFEM is not confined to the boundaries of the mesh. Therefore, there is no need for re-meshing or specifying a pre-defined path for crack propagation when working with XFEM. This makes XFEM a perfect tool for studying the onset and propagation of cracks in quasi-static problems.

The extended finite element method is based on the concept of partition of unity where enriched degrees of freedom are used to describe cracks within finite elements [104]. When using a cohesive segments approach, crack propagation is modelled as a two-step procedure.

Initially, when the damage initiation criterion is reached, the element is split into two new elements with phantom nodes connected at the location of the crack and separated by a cohesive surface. The crack topology is implicitly described using level-set theory [105]. Damage initiation is modeled with the use of a fracture criterion  $f$  and a vector that is set perpendicular to the direction of the crack. Next, the damage evolution law governs the transformation and/or degradation of the cohesive surface up until the crack opens (i.e., the crack surface becomes traction free). The damage evolution law can be defined in terms of the traction-separation law or the strain energy release rate [78]. There exist two fracture criteria that are commonly used in the simulation of crack propagation through bone. The interaction between the real and phantom nodes can be seen in Figure 2.8.

The first commonly used fracture criterion is the maximum principal strain criterion (MAXPE)

$$f_{MAXPE} = \left\{ \frac{\langle \varepsilon_{max} \rangle}{\varepsilon_{max}^0} \right\}$$

(3)

where  $\varepsilon_{max}$  is the maximum principal strain, and  $\varepsilon_{max}^0$  is the critical damage initiation strain. The symbol  $\langle \rangle$  is the Macaulay bracket which indicates that pure compressive states do not initiate damage. Crack propagation is achieved when  $f_{MAXPE} > 1$ . For MAXPE, the direction of the crack is assumed to be perpendicular to the principal strain.

The second commonly used criterion is the quadratic nominal strain criterion (QUADE)

$$f_{QUADE} = \left\{ \frac{\langle \varepsilon_n \rangle}{\varepsilon_n^0} \right\}^2 + \left\{ \frac{\langle \varepsilon_s \rangle}{\varepsilon_s^0} \right\}^2 \quad (4)$$

where  $\varepsilon_n^0$  is the normal critical damage initiation strain, and  $\varepsilon_s^0$  is the shear critical damage initiation strain. The two damage initiation strains are perpendicular to each other, with  $\varepsilon_n^0$  being aligned to the normal direction of the material. For the QUADE criterion, the crack propagation is assumed to be perpendicular to the normal strain.

- **Original nodes**
- **Phantom nodes**

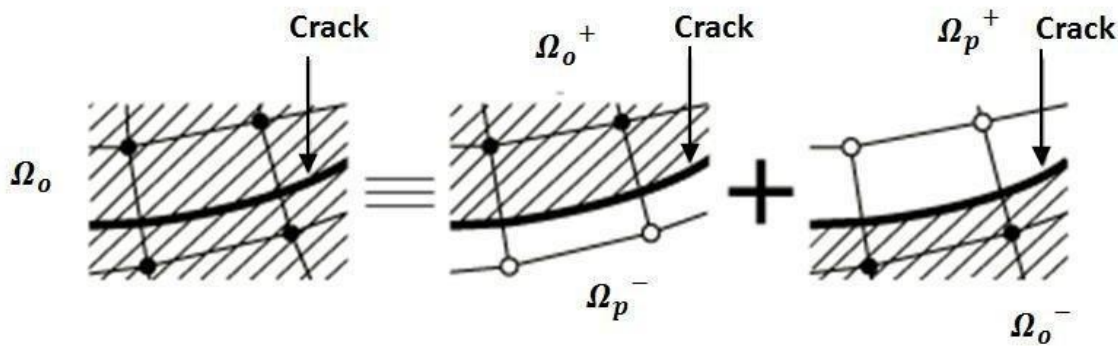


Figure 2.8 The principle of the phantom node method. Taken from [105]

## 2.4 XFEM simulation of crack propagation in bone

The first XFEM bone studies were done using the MAXPE criterion for crack initialization and linear elastic fracture mechanics (LEFM) as the crack growth law. The studies were performed on the microscale using 2D geometry and were used to analyze the effects of osteons on the propagation of the crack in cortical bone when subjected to uniaxial tensile loading. The predicted crack paths grew perpendicular to the applied load, and did not deflect around the cement line, as was expected from the experimental results [106–109].

Other studies tried using MAXPE criterion in combination with the cohesive segments approach rather than LEFM. These studies were also unable to generate realistic crack paths, that would deflect around cement lines [110–113]. Work by Rodriguez-Florez et al. [114] explored the possibility of using multiple enriched subregions for generation of multiple cracks. However, this approach was calculation-intensive, and not suitable for complex geometries [114]. Previous literature shows that just using MAXPE is not

sufficient when it comes to modeling crack propagation in bone, as the cracks do not capture the cement line deflections seen in the experimental data.

More realistic predictions of crack propagation through bone were achieved by Feerick et al. [115]. This study simulated a screw pull-out test in cortical bone using multiple damage criteria. The quadratic nominal stress (QUADS) criterion was used to simulate crack growth parallel to the osteon directions and maximum principal stress (MAXPS) criterion was used for off-axis crack propagation [115].

More recently a study by Gustafsson et al. [53] tried to combine the MAXPE and QUADE fracture criteria to achieve realistic crack propagation around osteons in 2D samples of cortical bone. In the study, a model for crack propagation in 2D at the microscale in cortical bone was developed using the XFEM method in ABAQUS (Figure 2.9 D). The objective of the study was to simulate crack deflections at the osteon boundaries as previously seen in experimental data. The study implemented the two fracture criteria (MAXPE and QUADE) using the UDMGINI subroutine. The results of Gustafsson et al. [53] show that the combined criteria method can be used to properly simulate crack propagation through bone with deflections at the cement line.

Due to its popularity and successes, XFEM will be used in combination with the dual fracture criteria method to simulate crack propagation in trabecular bone. As such, this thesis will heavily reference the work done by Gustafsson et al. [53].

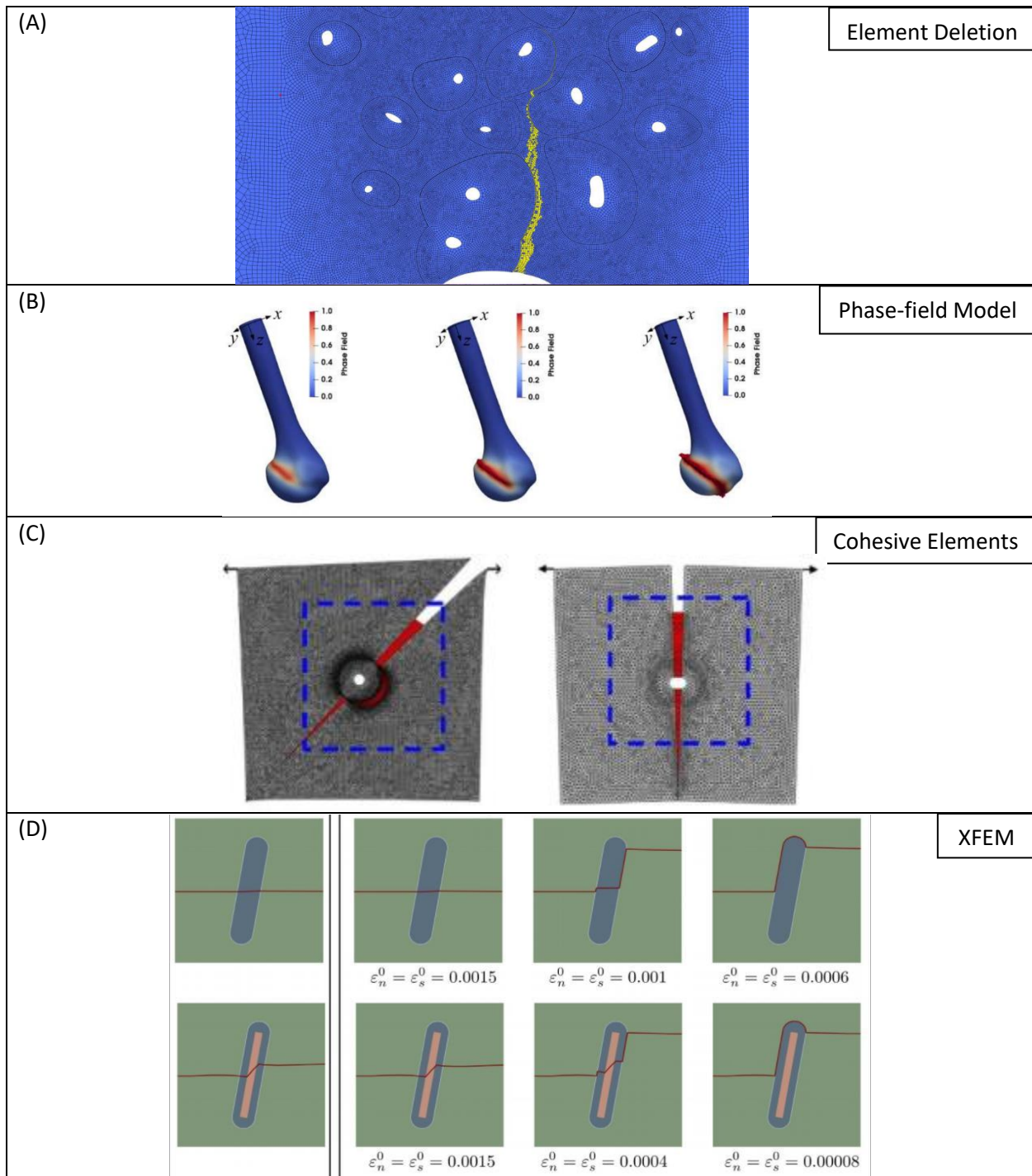


Figure 2.9 A set of damage models presented in literature that are used to model crack propagation in bone at the microscale. (A) 2D Crack simulation in cortical bone using the Element Deletion method taken from [79] with permission, (B) Crack analysis of a full bone using the Phase-field Model method Adapted from [88] with permission from John Wiley and Sons, (C) 2D Crack analysis around an osteon using the Cohesive Elements method Adapted from [96] with permission from American Society of Mechanical Engineers, (D) 2D crack propagation analysis of osteon using the XFEM method Adapted from [116] with permission from Elsevier

## 2.5 Trabecular bone modeling

A number of papers have used FEM and XFEM analysis to examine failure in cancellous bone. Unfortunately, that research focused on the macroscale of trabecular bone rather than modeling the BSU and cement lines on the microscale. Though it is important to research the mechanics of trabecular bone on all levels, and it would be too complicated to create and run a model that contains every hierarchical structure, there is a clear gap in knowledge when it comes to modeling trabecular bone at the microscale.

Hammond et al. [117] used a similar approach to Feerick et al. [115] to model crack propagation in trabecular bone, exploring the effect of using isotropic or anisotropic tissue with homogeneous or heterogeneous tissue distribution. The only downside to this study is that the two fracture criteria were used separately from one another in two different simulations. The models for this study were generated on the macro level. As such, the trabeculae were not sub divided into BSUs and cement lines. The sections of the 2D cancellous bone specimen can be seen in .

Salem et al. [118] modeled cancellous bone specimens to accurately predict the propagation of cracks under mechanical loading. The study used the MAXPE criterion to simulate crack propagation through a single trabecula, and 2D sections of trabecular bone specimens. Both the single trabecula and the 2D sections were modeled as a homogeneous material, showing no distinction between BSU and cement line.

Both studies mentioned above do not fully consider the complexity of the trabecular bone on the microscale. In the case of Hammond et al. [117], the paper tries to account for the different BSUs by using anisotropic and heterogeneous material properties. All the model cases that were considered in that study can be seen in . However, the simulation fails to include cement lines, and the absence of this important structure likely affects the accuracy of the crack predictions.

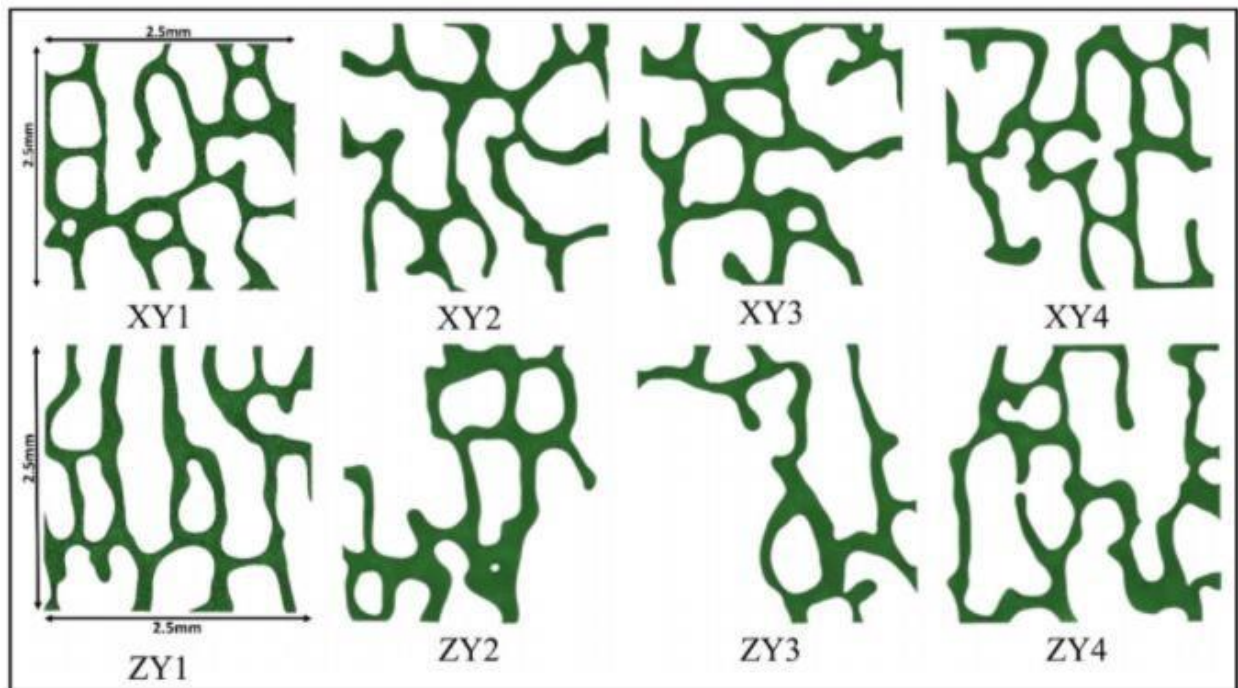


Figure 2.10 Sections of cancellous bone specimen. Taken from [118] with permission from sage Publishing

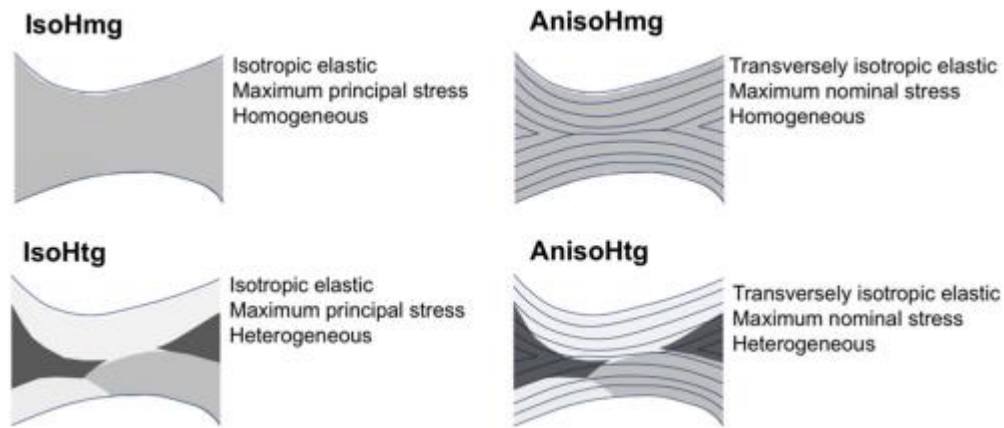


Figure 2.11 Model cases considered in the Hammond et al. study. Taken from [117] with permission from Elsevier

## 2.6 Literature review summary

The goal of this thesis is to use numerical methods to identify the role that cement lines play in terms of providing crack resistance to the trabeculae, and to better understand how changes in BSU size might affect crack growth. Therefore, this chapter reviewed background required to understand the current state of XFEM crack propagation modeling, in trabecular bone, at the microscopic level.

This literature review first provided a summary of the structure of cortical and trabecular bones at multiple length scales. This was done to show how each organizational level serves to improve the strength and resilience of bone. The literature of bone's mechanical properties was then reviewed to provide context for the material property values that are used in this study. Lastly, the literature on methods of FEM modeling of cracks in biomechanics was reviewed to identify a simulation method that would be most suited for simulating crack propagation in trabecular microstructure.

Only two studies were identified that simulated crack growth in trabeculae, and neither included the cement line in the models. Gustafsson is one of the few to investigate the effect of cement line in XFEM simulations, but only in cortical bone. This review suggests that the proposed investigation into the effects of decreasing BSU size, and increasing proportion of cement line, represents a novel area of research. Therefore, this study will use idealized BSU structures combined with XFEM analysis to better understand how cement lines affect crack growth in individual trabeculae.

## 3 Methods

### 3.1 Chapter introduction

This chapter will provide a detailed description of the methods that were used to accomplish this study including the following topics:

- the selection and validation of the crack failure model;
- the selection and generation of model geometry;
- the mesh and boundary condition analysis; and,
- an explanation of the three parametric studies undertaken during the research.

### 3.2 Simulation model selection

A modelling method had to be selected to ensure realistic simulations of crack propagation through trabecular bone. As previously discussed in the literature review section of this document, several modelling methods have been used in the literature to simulate crack propagation in bone. Based on previous studies in cortical bone, XFEM was chosen because it can produce arbitrary crack paths, which is a necessary attribute for the parametric studies presented in this thesis. The choice of XFEM modeling also allows the new dual damage criteria approach, which has been used to capture realistic crack deflection around osteons in cortical bone, to be applied to cancellous bone. Due to the assumed similarities in the mechanical properties of the cement line in trabecular and cortical bone, the dual criteria XFEM method was well suited for this research. The method was also well described and documented by Gustafsson and others which allowed for easy implementation in ABAQUS [53, 119, 120].

### 3.3 XFEM modeling method

The following section describes the XFEM crack analysis modeling, and its implementation in the ABAQUS software.

#### 3.3.1 Crack domain

The crack domain is an assigned area that contains all the regions where cracks can initiate and propagate in the material. Multiple cracks can nucleate in a single crack domain only if they reach their critical damage values at the same time increment. Otherwise, additional cracks will not nucleate until all the pre-existing cracks in the crack domain have propagated through the boundary of the given crack domain. If the model is expected to generate more than one crack, the part should be partitioned into multiple crack domains based on the model's geometry.

For this study, the entire sample was assigned a single crack domain. The single domain was considered sufficient since a single crack would be initialized in the model and only that one crack was expected to grow and propagate through the entire sample. No others were expected to nucleate. To confirm that this approach was appropriate, a single model was tested multiple times with up to five crack domains. The rectangular sample subjected to uniaxial tension in the vertical direction was partitioned into equally sized vertical strips, with each strip being allocated to a different domain. The simulations produced identical results compared to the model with a single domain. Therefore, a single crack domain was deemed sufficient for this study. The simulation results for the single crack domain and five different equally-sized crack domains can be seen in Figure 3.1.

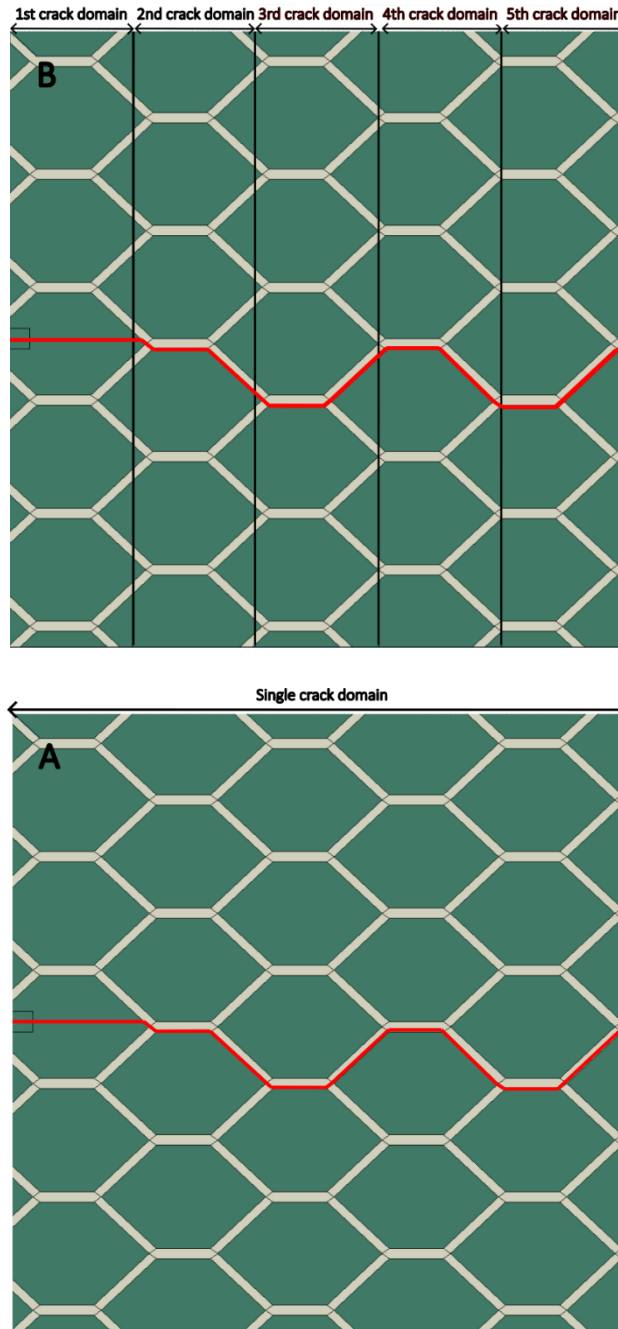


Figure 3.1 Crack path comparison between two test samples that were used to test crack domains. A: Sample with a single crack domain. B: Sample with five equally sized vertical crack domains. The crack path for both simulation is indicated in red

### 3.3.2 Initial crack location

The user can specify an initial crack location to provide a better level of control over the nucleation of the crack. The initial crack can either be modelled as a wire object in a two-dimensional part or defined using the geometry of the modelled object. For example, the crack can be defined using a boundary between two materials or a sharp angle in the object.

An initial crack must be located inside the crack domain to be able to propagate; however, it is optional. Regardless of whether an initial crack is present, ABAQUS can simulate crack nucleation and growth as defined by the selected failure criterion.

This study uses a 5  $\mu\text{m}$  crack to standardize crack initiation between different simulations. The initial crack is always located at the halfway point along the height of the sample, on the leftmost edge of the sample, oriented perpendicular to the edge and in the tensile direction. The crack (indicated in red in Figure 3.2) is always bound inside a  $10 \times 10 \mu\text{m}^2$  partition, highlighted in yellow in Figure 3.2. The partition is meshed separately from the rest of the model to ensure that the initial crack does not pass through any mesh nodes, as doing so would sometimes cause computational errors in ABAQUS.

One of the computational errors mentioned above can be seen in Figure 3.3, where the initial crack (indicated in red) intersects with a mesh node (indicated with a blue square). As shown in Figure 3.3, the intersecting node (again indicated by a blue square) does not separate from its phantom node, causing an unrealistic crack propagation behaviour.

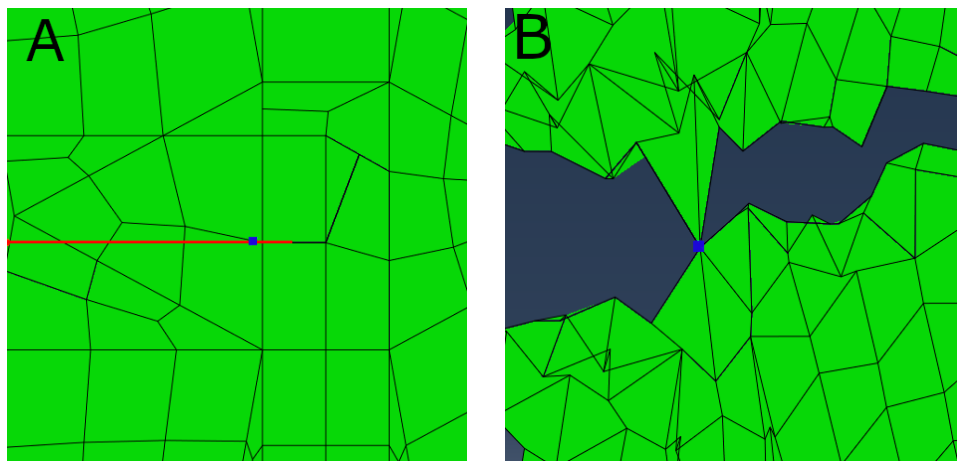


Figure 3.3 A) A model where the initial crack (indicated in red) intersects with a mesh node due to poor partitioning. The intersection is indicated by a blue square. B) The same node (indicated with a blue square) fails to split from its phantom node, causing a computational error

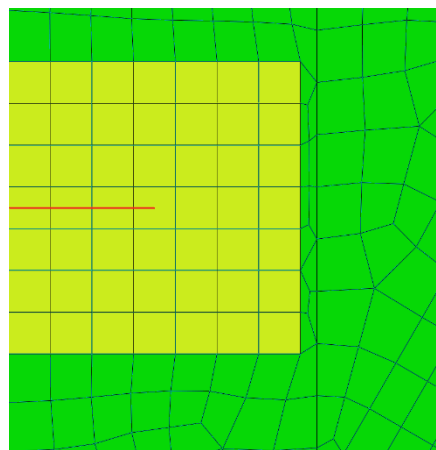


Figure 3.2 Initial crack indicated in red surrounded by a partition indicated in yellow

### 3.3.3 Damage initiation

The damage initiation criterion governs crack growth and is used to determine the crack direction. As outlined in the Literature Review, the criterion can be based on either strain or stress. Following the example of Gustafsson et al. [53], two different strain-based failure criteria were used for crack growth in the cement line versus the BSU.

Crack propagation through the BSUs was governed by the MAXPE criterion (Equation 1). Once the damage is initiated in an element, the growth of the crack is then modelled with an energy-based damage evolution law with linear softening behavior.

Conversely, crack propagation in the cement line was governed by a dual criterion that uses a combination of both the MAXPE (Equation 3) and QUADE (Equation 4) criteria:

$$f_{Sub} = \max \left\{ \left\{ \frac{\langle \varepsilon_n \rangle}{\varepsilon_n^0} \right\}^2 + \left\{ \frac{\langle \varepsilon_s \rangle}{\varepsilon_s^0} \right\}^2, \left\{ \frac{\langle \varepsilon_{max} \rangle}{\varepsilon_{max}^0} \right\} \right\}$$

(5)

where the crack propagation is achieved when  $f > 1$ .

ABAQUS does not natively support the use of two damage criteria in the same material. However, the UDMGINI subroutine can be implemented to allow the user to create their own damage criteria, which can then be used by ABAQUS. The subroutine code is presented in Appendix A: Fortran code.

It is important to note that QUADE and MAXPE use different methods to calculate the path of crack propagation. In MAXPE, the crack propagates in a direction perpendicular to that of the maximum principal strain. In most cases, when the MAXPE criterion is used, the crack will propagate perpendicularly to the loading conditions, creating no deflections in the crack path. However, with the QUADE criterion cracks propagate perpendicularly to the normal direction of the material. When the normals are properly assigned to the cement line elements, the QUADE propagation allows the crack to travel along the cement line, causing it to deflect around the BSU. These differences in crack propagation are a core feature of the dual-damage subroutine and allow the crack to travel through either the BSU or the cement line based on which criterion is triggered first.

Since the QUADE damage criterion uses normal vectors to determine the direction of propagation, each element in the cement line had to be assigned a normal vector based on its position within the geometry. This step was accomplished via python scripts. Figure 3.4 shows a close-up of the cement line, with the assigned element normals indicated by the teal arrows.

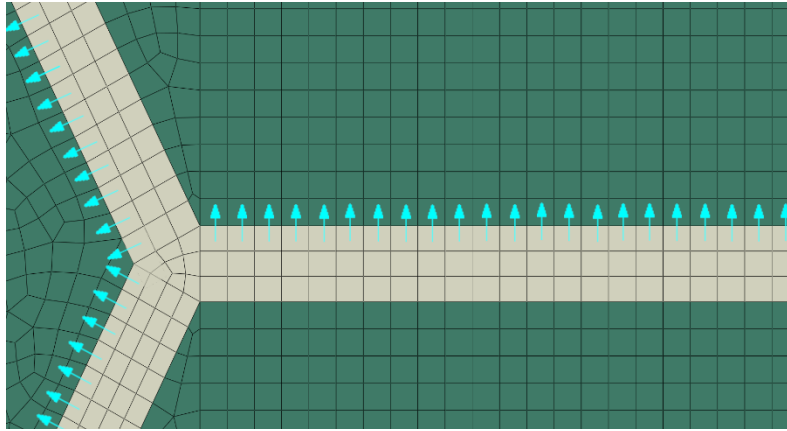


Figure 3.4 A close-up of the cement line mesh with element normal directions indicated by teal arrows. All cement line elements have a unique normal; however, only selected normals are shown for clarity

### 3.3.4 Limitations

The following list is a summary of XFEM limitations in the ABAQUS software, specifically version 6.10 which was used in this study [121]:

- a crack cannot branch into multiple cracks;
- only one crack can exist in a particular element;
- a crack can only turn up to 90 degrees within a particular element; and,
- only linear continuum elements can be used (CPE4, CPS4, C3D4, C3D8).

Though this study was not strongly affected by these limitations, they are important to keep in mind for future studies.

## 3.4 Material properties

The cement line and the BSU were assumed to exhibit isotropic linear elastic behaviour. Based on the literature review, it was decided that the material properties used by Gustafsson to simulate crack propagation in cortical bone would also be used in trabecular bone given the parametric nature of the work presented herein.

The Young's modulus ( $E$ ) of the BSU was used as a reference for choosing a stiffness for the cement line. The cement line was assumed to be 20% stiffer than the BSU, due to the fact that the cement line is considered to be highly mineralized. The Poisson's ratio ( $\nu$ ), MAXPE critical strain ( $\epsilon_{max}^0$ ), and the energy release rate ( $G$ ) were all assumed to be equal between the BSU and the cement line. All of the material properties are summarised in Table 3.1 and are used throughout this work without any adjustment.

Table 3.1 List of material properties used in this study

Parameter	BSU	Cement line
$E$ (GPa)	15	18
$\nu$	0.3	0.3
$\epsilon_{max}^0$	0.004	0.004
$G \left( \frac{kJ}{m^2} \right)$	0.2	0.2

### 3.5 Recreation of previous studies and validation of subroutine

The dual damage criteria method was previously used and described in several studies; however, the exact details of implementing the method were never specified. The method had to be reverse engineered based on the descriptions given in the Gustafsson et al. [53] and example code of the UDMGINI subroutine provided by Mohammad Salem in his thesis [119]. To ensure that the new subroutine worked similarly to the original, an XFEM model based on work in Gustafsson et al. [53] was recreated and tested to ensure its accuracy.

An idealized model geometry of a circular osteon, surrounded by cement line, and embedded in a homogeneous block of lamellar bone was created based on Gustafsson et al. [53]. Displacement controlled loading was applied on all nodes along the top edge and all nodes along the bottom edge were constrained in the y-direction. The osteon was assumed to be 150  $\mu\text{m}$  in diameter with a 50  $\mu\text{m}$  wide Haversian canal. The geometry measured 400  $\times$  400  $\mu\text{m}^2$  with a 40  $\mu\text{m}$  long initial crack inserted in the left edge perpendicular to the displacement direction. The initial crack was placed 3.25  $\mu\text{m}$  above the middle point of the left edge to avoid perfectly symmetric conditions (see Figure 3.5). Plane stress 4-node bilinear elements with reduced integration (CPS4R) were used to mesh the model. A range of QUADE critical strain values ( $\varepsilon_n^0 = \varepsilon_s^0 = 0.0010 - 0.0025$ ) were used to simulate crack propagation in and around the radial osteon. The results from Gustafsson et al. [53] show a clear transition between crack deflection and crack penetration between  $\varepsilon_n^0 = \varepsilon_s^0$  values of 0.0015 and 0.0016. The goal of this test was to capture the transition between crack deflection and crack penetration near the QUADE critical strain values seen in previous works in order to validate the subroutine implementation.

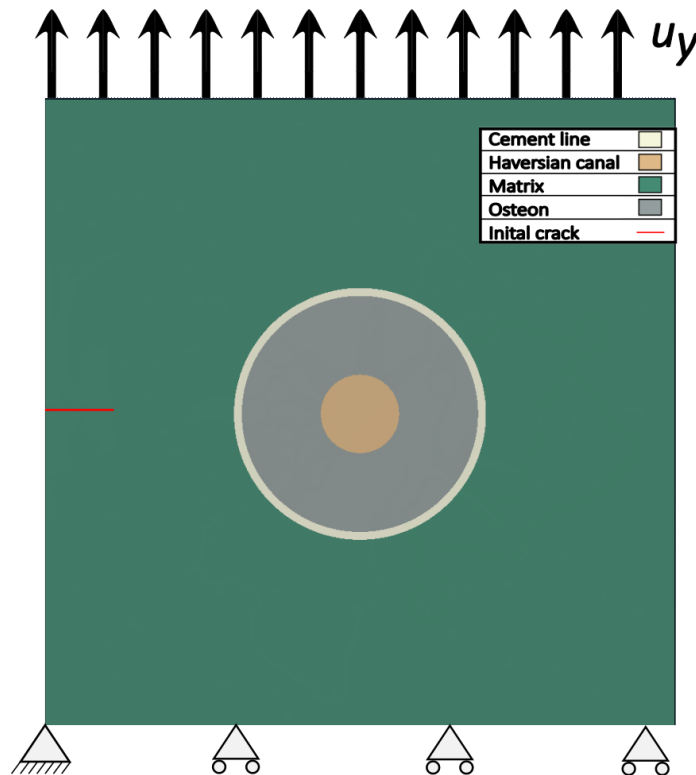


Figure 3.5 Model geometries used to represent an osteon in the radial direction. Modeled from Gustafsson et al. [108]

### 3.6 Modeling geometry

Modelling crack propagation in trabecular bone on the microscopic scale is a new area of study, and as such, there is little to no literature on this topic. Because of the lack of previous results, this research was completed under many assumptions and simplifications to establish a basis for future study. One of the major simplifications adopted by this research was the simplified geometric representation of the BSU.

Trabecular bone is a biological material, and as such, it is irregular in both shape and size. The BSUs usually have smooth edges, and semi-crescent shapes. A real trabecular profile with 20 BSUs can be seen in Figure 3.6. To automatically model a realistic trabecular profile like the one seen in Figure 3.6 would require the use of complex algorithms, the creation of which is outside of the scope of this study.

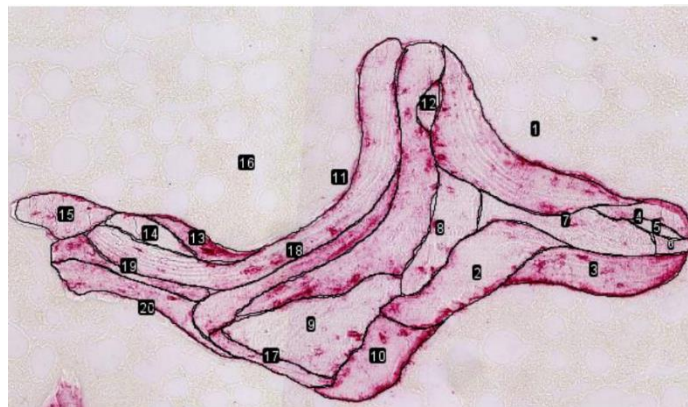


Figure 3.6 Trabecular profile with 20 distinct BSUs. Taken from [28] with permission

As a first estimation, it was decided that the BSUs should be represented by a set of tiling geometric shapes, which would be separated by a uniform cement line of constant thickness. This simplified geometry allowed the creation of python scripts that can automatically generate perfectly partitioned geometries with varying geometric parameters.

There are only three regular shapes that tile tightly. Triangles, squares and hexagons were all considered as a possible tiling shape for this study. Unfortunately, both triangles and squares tile by subdivision, creating parallel lines that are infinitely straight. This geometric phenomenon causes problems, as a crack traveling through an infinitely straight cement line would never need to propagate around a BSU, making the simulation pointless. The preference therefore was given to hexagonal patterns, as they allow the creation of tiling surfaces without gaps and or continuous straight lines. The hexagons can also be distorted in multiple directions without losing the ability to tile.

A python script was developed to partition a 2D plate of any size into hexagonal BSUs separated by a cement line of any thickness (see Appendix B: Python script). The width, height, and side angle of the generated hexagons could be adjusted separately, allowing for a wide range of geometries (see Figure 3.7). All of the adjustable parameters include:

- the width of the sample trabeculae plate ( $W$ );
- the height of the sample trabeculae plate ( $H$ );
- the height of the BSU ( $h_{BSU}$ );
- the width of the BSU ( $w_{BSU}$ );
- the angle of the BSU side walls relative to the horizontal line ( $\theta$ );
- the thickness of the cement line ( $t$ );
- horizontal partition displacement ( $X_{DIS}$ ); and,
- vertical partition displacement: ( $Y_{DIS}$ ).

Since the boundary conditions can affect the results of the simulation if the crack propagates too close to them, it was decided that the initial crack would always be located at the vertical half point of the specimen plate (see Figure 3.7). Since the location of the initial crack is of great interest in this thesis, a set of parameters  $X_{DIS}$  and  $Y_{DIS}$  were introduced in the python script to allow the shifting of the BSU partitions on the sample plate.

Figure 3.8 shows how the two parameters can be used to adjust the location of the crack relative to the BSUs while not actually moving the initial crack.

Figure 3.8a shows a sample plate populated with hexagonal BSUs. For this sample the  $X_{DIS}$  and  $Y_{DIS}$  values were both set to 0 and, as such, the first hexagonal BSU (highlighted in yellow) was generated exactly in the bottom left corner. The other BSUs were tiled from that initial BSU, creating the pattern seen in the figure. Looking at the initial crack location of Figure 3.8a, we can see that the initial crack spans both the BSU and part of the cement line. Since the cement line also introduces extra partitioning near the crack, it is highly likely that the mesh around the initial crack will be compromised and will cause numerical errors, as previously discussed in section 0.

Figure 3.8b shows the same sample, however, here the  $X_{DIS}$  was set to 5  $\mu\text{m}$  and  $Y_{DIS}$  was set to 10  $\mu\text{m}$ . This change in variable values caused the entire BSU partition to shift in such a way, as to allow the initial crack to be located at the left most side of the BSU, and vertically directly in the middle of it. In this study, the two parameters  $X_{DIS}$  and  $Y_{DIS}$  will be used extensively to manipulate the location of the crack relative to the BSU partition.

Based on previous literature, it was also decided that the cement lines will be kept a constant thickness  $t=5 \mu\text{m}$  throughout the entire study to reduce the number of adjustable parameters. Figure 3.9 shows some of the geometries that can be generated by the script.

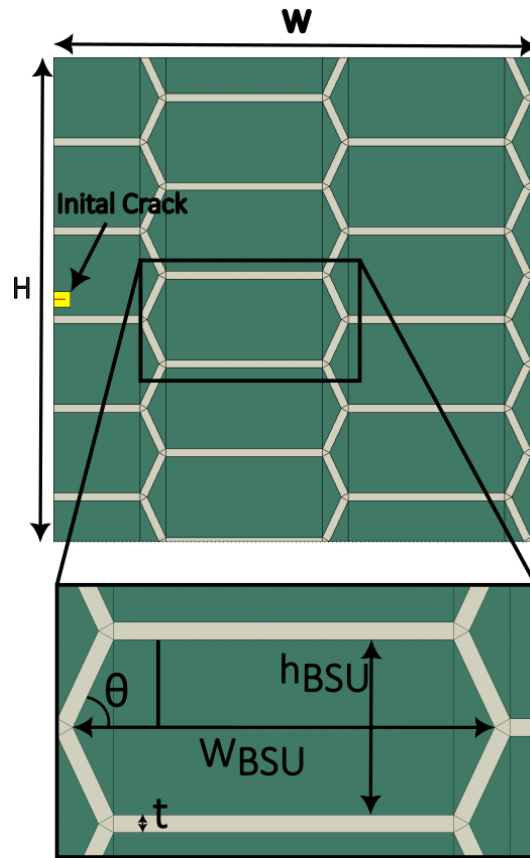


Figure 3.7 Labeled geometry of the tiled BSUs showing all the adjustable parameters: specimen width ( $W$ ), specimen height ( $H$ ), BSU width ( $w_{BSU}$ ), BSU height ( $h_{BSU}$ ), cement line thickness ( $t$ ), BSU wall angle ( $\theta$ ) and the location of the initial crack indicated in red with its partition highlighted in yellow.

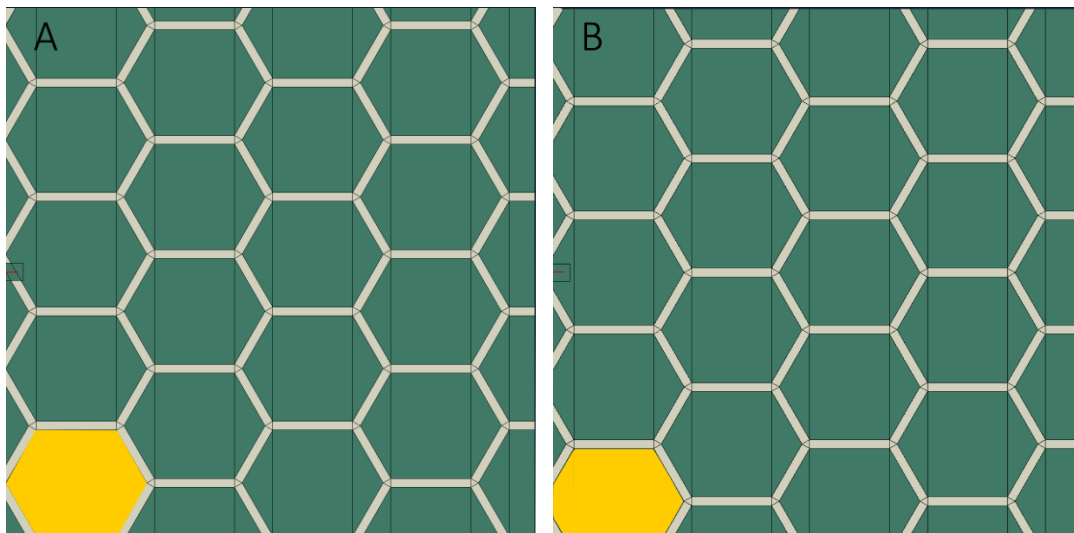


Figure 3.8 Example of how parameters  $X_{DIS}$  and  $Y_{DIS}$  affect the partitioning of the sample plate. A) Sample partitioned into BSUs without the use of  $X_{DIS}$  and  $Y_{DIS}$  parameters. B) the same partitioning with  $X_{DIS}$  set to  $5\mu\text{m}$  and  $Y_{DIS}$  set to  $10\mu\text{m}$ . The BSU that was generated first is highlighted in yellow. Note the interaction between the initial crack and the partition geometry.

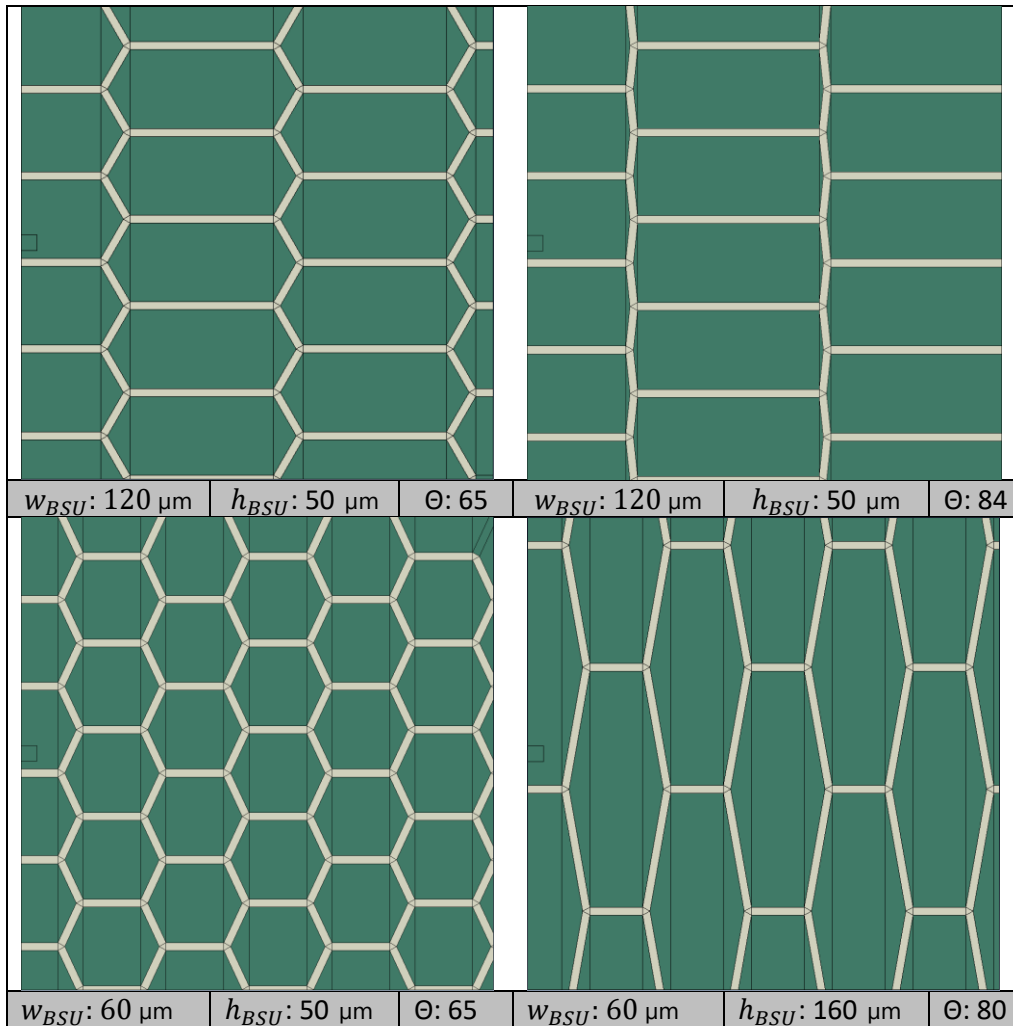


Figure 3.9 examples of BSU geometries that can be generated with the python script. As mentioned above,  $t=5 \mu\text{m}$  for these and all other models in this study. The trabeculae plate sample dimensions are constant at  $300 \times 300 \mu\text{m}^2$ . With  $XDIS$  and  $YDIS = 25 \mu\text{m}$ .

### 3.7 Boundary conditions

The samples underwent a uniform displacement-based loading for all simulations in this study using quasi-static analysis. As shown in Figure 3.10, each model was assigned nodal boundary conditions to replicate uniaxial loading. Nodes along the bottom edge were fixed in the vertical Y-direction, while the top edge nodes were uniformly loaded in the vertical Y-direction until either a maximum displacement of  $10 \mu\text{m}$  was achieved or until complete failure occurred. The latter was defined as the moment when the crack completely traversed the model from left to right. The nodes in the top left and bottom left corners were also fixed in the horizontal X-direction.

Since the models represent a part of a larger structure, it was crucial to ensure that the applied boundary conditions do not interfere with the crack propagation and the resulting macroscopic failure strains. Several simulations were performed to test the effects of boundary conditions where a crack was propagated through a sample of pure BSU material. Throughout the simulations, the height of the specimen,  $H$ , was increased by doubling the height of the previous model from  $H=100 - 800 \mu\text{m}$ . The results were compared between the tested samples to identify if the distance between the boundary conditions and the crack produced any changes in the results.

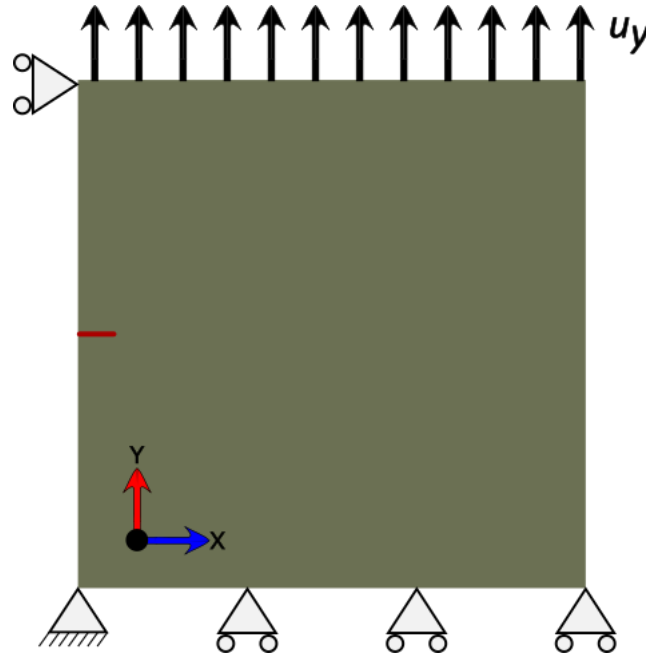


Figure 3.10 A sample showing the boundary conditions used in this study, with the initial crack highlighted in red.

### 3.8 Data collection and results

Since one of the primary goals of this study was to identify how the size of the BSUs affects a trabecula's ability to resist crack growth, it was essential to find a way to compare crack resistance between multiple simulations.

It was decided that the macroscopic tensile strain required to propagate the crack across the sample from the left edge to the right edge would be a suitable parameter to identify the crack resistance of the trabeculae. The results of each simulation were reviewed to identify the time step at which the crack tip reached the opposite side of the sample. Since each sample undergoes displacement-based loading, the displacement of the loaded top edge of the specimen can be recorded at the proper time step and converted to strain based on the height  $H$  of the sample. The strains can then be compared between different simulations as long as the width of the sample plate stays the same between the simulations. The entire simulation history could also be examined to identify areas where strain buildup occurred during the simulation. Figure 3.11 shows a model with the simulated crack highlighted in red. This test sample was evaluated at 4 different time steps. The blue triangles in the figure indicate the location of the crack tip at each tested step. In this example the strain buildup occurred up to crack tip location #3, at which point the crack propagated to the end of the sample without further deformation of the plate.

Another result of interest is the crack path itself. In parts of this study, the strain at complete crack propagation and the crack path were used together to identify how the trabeculae resisted crack propagation.

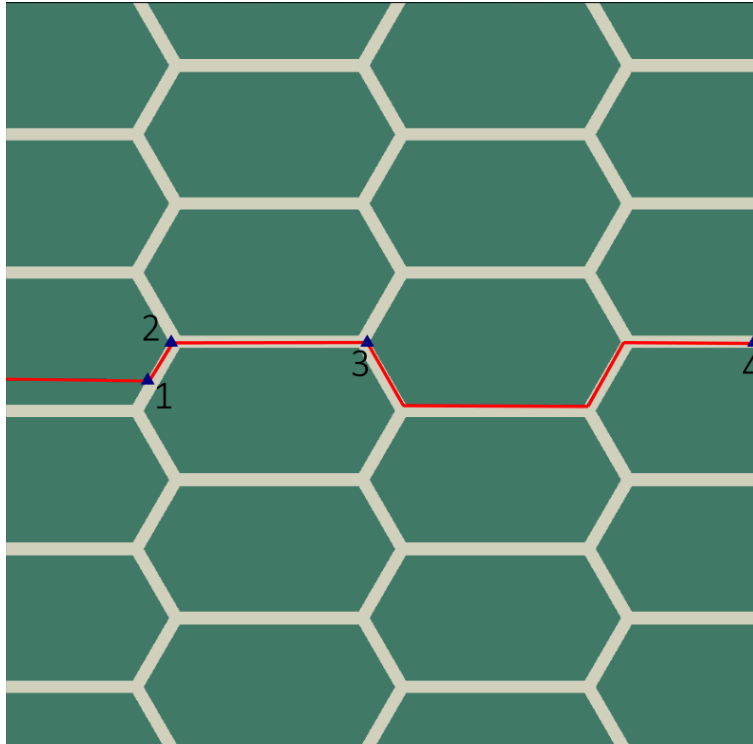


Figure 3.11 A test sample with the simulated crack propagation highlighted in red. 4 separate strain readings were taken at different time steps. The blue triangles indicate the locations of the crack tip at the point when readings were taken. **(1)** time increment 219; strain at top edge  $4.13 \times 10^{-3}$ . **(2)** time increment 301; strain at top edge  $4.19 \times 10^{-3}$ . **(3)** time increment 380; strain at top edge  $4.96 \times 10^{-3}$ . **(4)** time increment 484; strain at top edge  $4.96 \times 10^{-3}$ .

### 3.9 Mesh analysis

Due to the mesh restrictions of XFEM, the plane stress 4-node bilinear elements with reduced integration (CPS4R) were used to mesh all of the models in this study. Based on the work of Gustafsson, an initial mesh size of  $2.5 \mu\text{m}$  was established as a base size; however, a thorough mesh analysis had to be completed to ensure that the mesh size was sufficiently refined for the geometries used in this study.

A comparison was completed for mesh sizes ranging from  $3.5 \mu\text{m}$  to  $0.5 \mu\text{m}$ . A total of 50 mesh sizes were tested to provide an in-depth analysis. The tests were done on a  $150 \times 150 \mu\text{m}$  ( $W \times H$ ) sample with  $120 \times 50 \mu\text{m}$  hexagons ( $w_{BSU} \times h_{BSU}$ ) having a side angle of  $\theta = 35^\circ$ . Based on the results, which can be seen in the results section of this document, a mesh size of  $1.8 \mu\text{m}$  was chosen as the primary average mesh size for this study (see Figure 3.12)

The mesh size was also given an allowance of  $\pm 0.1 \mu\text{m}$  to provide some flexibility in models that required extra remeshing. For further information on remeshing see section 3.10.

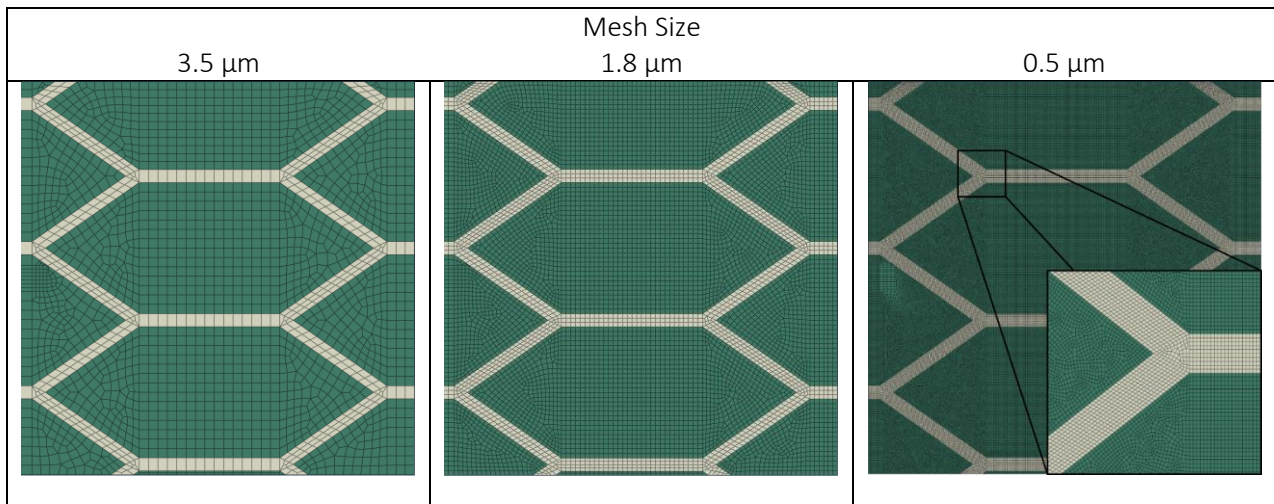


Figure 3.12 Examples of a number of mesh analysis models meshed with different element sizes. 3.5 μm mesh was the biggest mesh size tested, while the 0.5 μm mesh was the smallest. The 1.8 μm mesh was selected as the primary mesh size for this study. Note that the images show only a small section of a model, to make the smaller mesh size more visible.

### 3.10 Model adjustment

Though most of the models and simulation were completed automatically via scripts, a number of simulations failed and, as such, had to be manually adjusted by the researcher. This section will discuss some of the problems that occurred during the research, and how they were solved.

The most common error that occurred during the crack simulation was the “timeout error”. Some sections of the simulation required extremely small time increments for the crack propagation calculations. When the time increment requirement reached the minimum increment set in the model, the simulation would terminate with a timeout error. Since reducing the minimum time increment size increased the run time of the simulation, doing so for every simulation would be inefficient and time consuming. With the time period set to 1, the minimum increment size was always set to  $1 \times 10^{-10}$  and only lowered for simulations that produced a timeout error. In some cases, the minimum increment size reached as low as  $1 \times 10^{-20}$  before the simulation was able to properly calculate crack propagation through the model. This solution only affected the runtime of the simulations and had no affect on the results.

A second, more substantial problem that occurred was based on improper crack propagation. During the simulation, some cracks tended to loop onto themselves during the deflection around the BSU. Figure 3.13 shows an example of this looping behaviour occurring in one of the study samples. The solution for this behavior was to re-mesh the model after small changes to the model parameters. Some of the solutions involved increasing or decreasing the mesh size by  $0.01 \mu\text{m}$  increments up to the allocated mesh difference of  $\pm 0.1 \mu\text{m}$  (as stated in section 3.9), adjusting the  $Y_{\text{DIS}}$  value by up to  $\pm 0.5 \mu\text{m}$  to slightly sift the vertical location of the initial crack inside the BSU, or adding extra partitioning to disturb the original mesh matrix. Since each of the adjustments could potentially change the resulting strain response in a significant way, only one method was used at a time, and the modification was kept as small as possible.

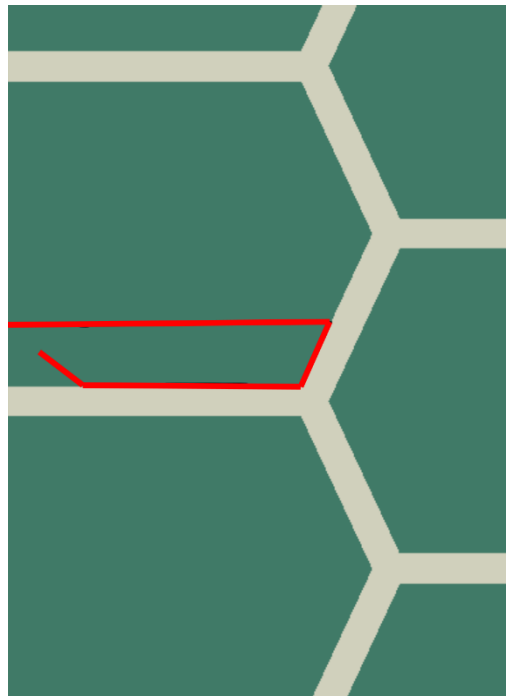


Figure 3.13 A failed simulation where the crack looped back on itself instead of propagating through the sample. The crack path was highlighted in red. The view is zoomed in on a portion of the sample to provide a better visual of the crack path.

### 3.11 Parametric studies

This thesis consists of three different parametric studies intended to investigate the effects of BSU geometry on crack growth. Since the XFEM dual damage criteria method has not been used to simulate crack propagation in trabeculae at the micron magnification before, multiple parametric studies had to be undertaken to investigate some important fundamental parameters. Each study only varied one or two parameters to identify how each affected the rate of crack propagation through a trabecula.

#### 3.11.1 First parametric study

In previous studies by Gustafsson, the QUADE critical strain values ( $\varepsilon_n^0, \varepsilon_s^0$ ) were identified as important parameters for determining whether the crack propagated through the osteon or around it in the cement line. Repeating a similar study for trabecular bone would confirm that comparable behaviour is achievable in a trabecular microstructure and would provide a range of QUADE values to be used in the next two parametric studies.

Therefore, the objective of the first parametric study was to identify the critical values for the interface damage model that caused the crack to propagate around the BSU via cement lines rather than through it. A secondary objective was to examine how a change in the BSU side angles ( $\theta$ ) would affect those critical values. The adjustable parameters for the BSU partition script were set as follows:

- $H \times W$ :  $300 \times 300 \mu\text{m}$ ;
- $h_{BSU} \times w_{BSU}$ :  $50 \times 120 \mu\text{m}$ ;
- $t$ :  $5 \mu\text{m}$ ; and,
- mesh size:  $1.8 \mu\text{m}$ .

The  $X_{DIS}$  and  $Y_{DIS}$  were set to place the initial crack inside the BSU at  $80 \mu\text{m}$  away from the furthest right point of the BSU, and  $10 \mu\text{m}$  below the horizontal midpoint of the BSU (see Figure 3.14).

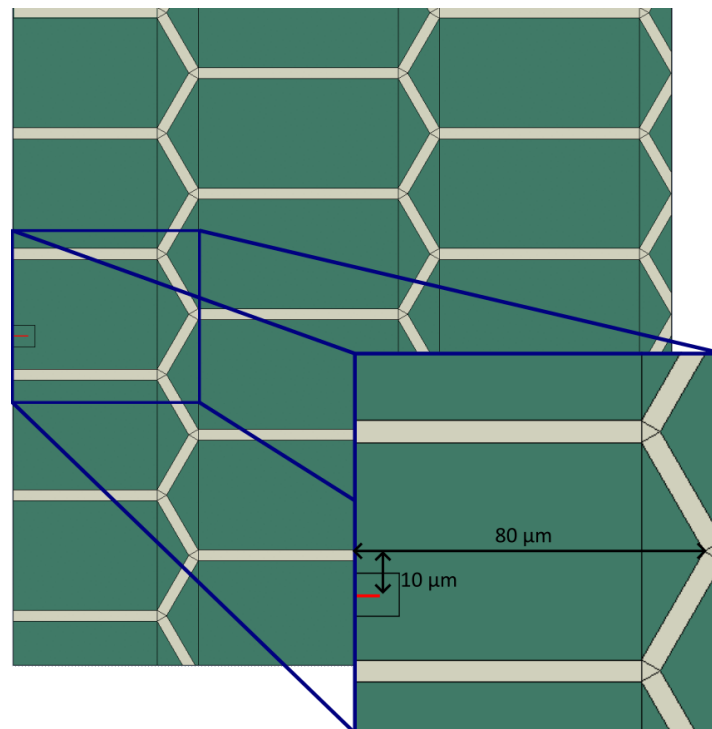


Figure 3.14 A model from the first parametric study with  $\theta$  set to  $60^\circ$ . The enlarged area shows the location of the initial crack inside the BSU

The BSU side angle,  $\theta$ , was varied in the range of  $40\text{--}80^\circ$  in  $5^\circ$  increments. Each angle increment was simulated with 7 different QUADE critical strain values ranging from  $1 \times 10^{-3}$  to  $7 \times 10^{-3}$  to identify the transition point between crack deflection around and crack propagation through the BSU at each  $\theta$  angle. For each of the 63 simulations, the strain to full crack propagation, and the path of crack propagation, were both recorded to visualize how the crack path affected the crack resistance of the model microstructure.

### 3.11.2 Second parametric study

The objective of the second parametric study was to identify how the overall size of the BSU affects the crack resistance of the trabeculae. For this study, the aspect ratio of the hexagons was changed to better represent the real BSUs which are usually orientated parallel to the trabeculae (see Figure 3.15). Since the size of the BSUs would be the variable investigated in this study, a constant BSU width to

height ratio ( $w_{BSU}/h_{BSU}$ ) of 1:5 was chosen and maintained for all of the models in this parametric study. This new ratio only allowed  $\theta$  angles between 77-90° because of how the hexagon geometry was defined. Therefore,  $\theta$  was set at a constant 80° for the entirety of this parametric study to ensure that only the scaled size of the BSU would change between models. The sample size was also adjusted to better represent the thickness of a trabeculae. The adjustable parameters for the BSU partition script were set as follows:

- $H \times W$ :  $400 \times 150 \mu\text{m}$ ;
- $w_{BSU}/h_{BSU}$ : 1.5;
- $\theta$ : 80°
- $t$ :  $5 \mu\text{m}$ ;
- $\varepsilon_n^0 = \varepsilon_s^0$ : 0.0015; and,
- mesh size:  $1.8 \mu\text{m}$ .

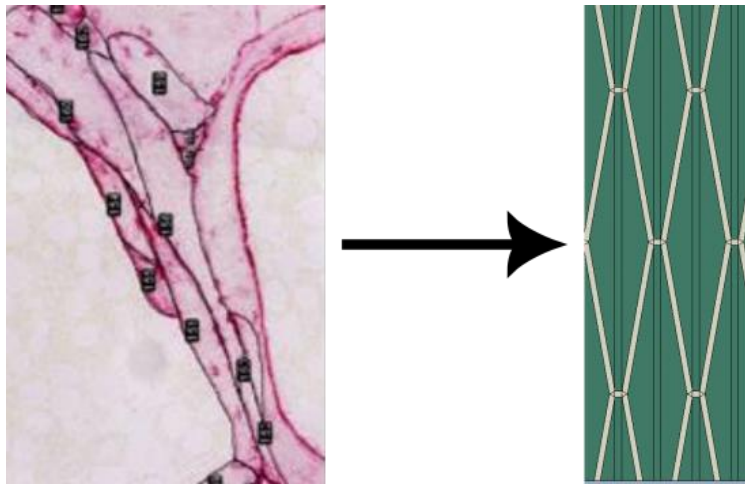


Figure 3.15 Comparison between real BSUs in a trabecula of a vertebral body taken from [28] with permission, and the idealized hexagonal BSUs that were used in the second parametric study.

There exists a number of possible crack propagation paths that can occur inside the trabecula. A mixed crack propagation involves both propagation through the BSU and the cement line. This is the most common scenario, as cracks are more likely to start in the BSU and propagate through it until they reach the cement line. At that point the crack will deflect around the rest of the BSUs by following the cement line to the other side of the trabecula. The other two types of propagation are pure penetration where no deflection around the BSU occurs, and pure deflection where the crack initiates in the cement line and never enters the BSU throughout its propagation.

The following sections will describe the methods that were used to study the effects of the size of BSU in relationship to the different types of crack propagation mentioned above.

#### 3.11.2.1 Mixed crack propagation

Since the mixed crack propagation was most likely to occur in real life, it was thoroughly studied. The  $X_{DIS}$  and  $Y_{DIS}$  parameters were constantly adjusted for each model to keep the initial crack location approximately  $5 \mu\text{m}$  above the vertical center of the BSU, and as far to the left of the BSU as possible. Though the vertical distance was kept as close to  $5 \mu\text{m}$  above the vertical center of the BSU as possible, the distance was sometimes adjusted as mentioned in section 3.10. With this initial crack location, the

crack would be forced to propagate through an entire BSU (minus the initial crack length) before reaching the cement line.

After reaching the cement line, the chosen QUADE critical strain ( $\varepsilon_n^0 = \varepsilon_s^0 = 0.0015$ ) would force the crack to propagate in the cement line, deflecting around the BSUs for the rest of the propagation. The size of the tested BSUs ranged from 15×75 all the way to 75×375  $\mu\text{m}$  ( $w_{\text{BSU}} \times h_{\text{BSU}}$ , see Figure 3.16).

#### 3.11.2.2 *Pure penetration and pure deflection crack paths*

Though the other two paths were of interest, they did not require an extensive amount of data compared to the mixed crack propagation path. As such, the two other paths were only simulated with five different BSU sizes ranging from 20×100 to 60×300  $\mu\text{m}$  ( $w_{\text{BSU}} \times h_{\text{BSU}}$ ) in equally sized increments.

For the BSU penetration crack path, the initial crack location was identical to the mixed crack propagation setup. To achieve crack propagation through the BSU rather than around it, the QUADE critical strains were raised to  $\varepsilon_n^0 = \varepsilon_s^0 = 0.0020$ . This change in QUADE critical strain caused a similar effect to what was seen in section 3.5.

For the cement line only propagation path, the  $X_{\text{DIS}}$  and  $Y_{\text{DIS}}$  parameters were adjusted so that the initial crack was located inside the horizontal section of the cement line (see Figure 3.17). Since the QUADE critical strain values stayed identical to the mixed crack propagation values ( $\varepsilon_n^0 = \varepsilon_s^0 = 0.0015$ ), the crack followed the cement line all the way to the end of the sample without ever entering the BSU.

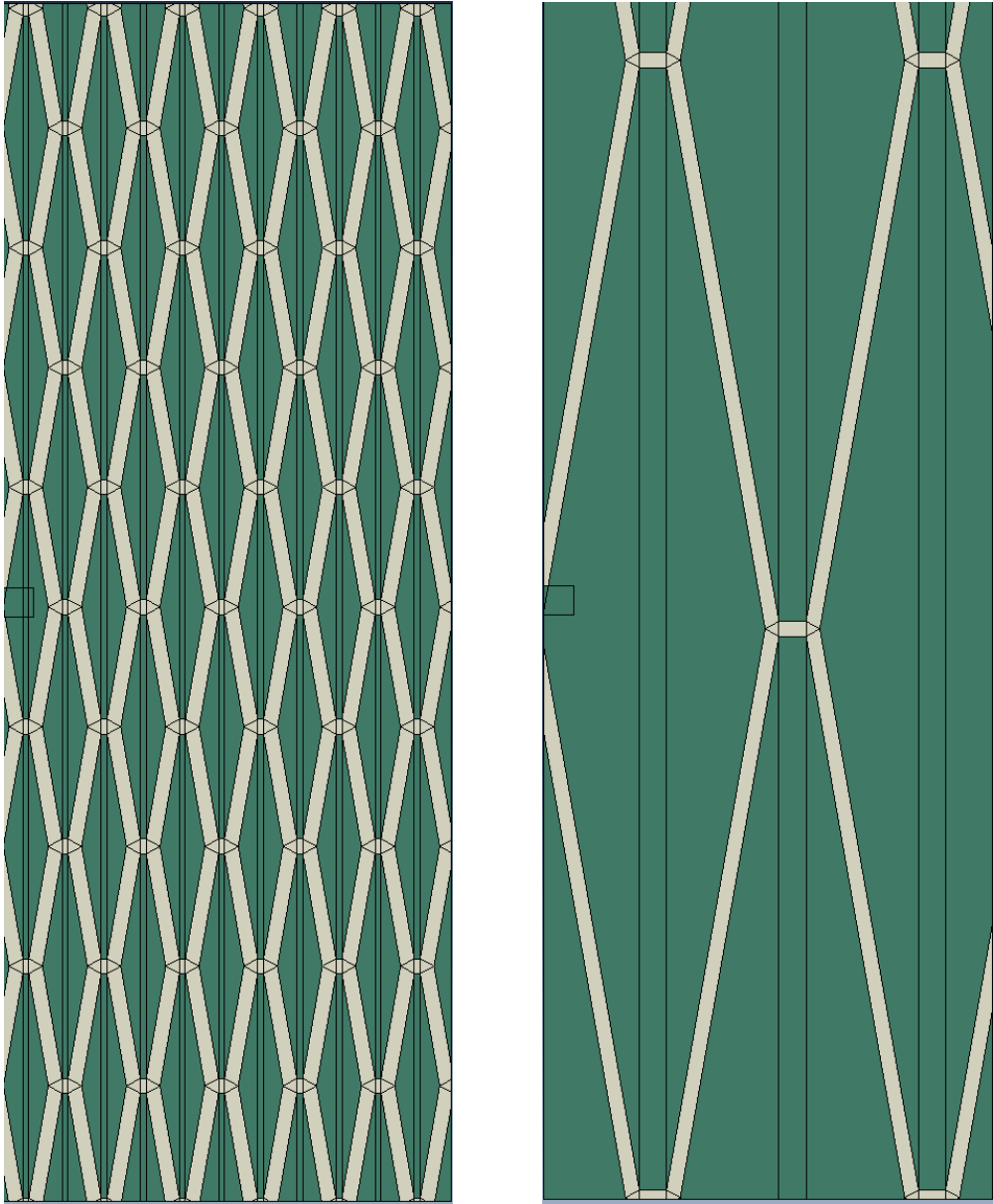


Figure 3.16 Two models of the second parametric study partitioned with different size BSUs. A) BSU size  $15 \times 75 \mu\text{m}^2$  B) BSU  $75 \times 375 \mu\text{m}^2$

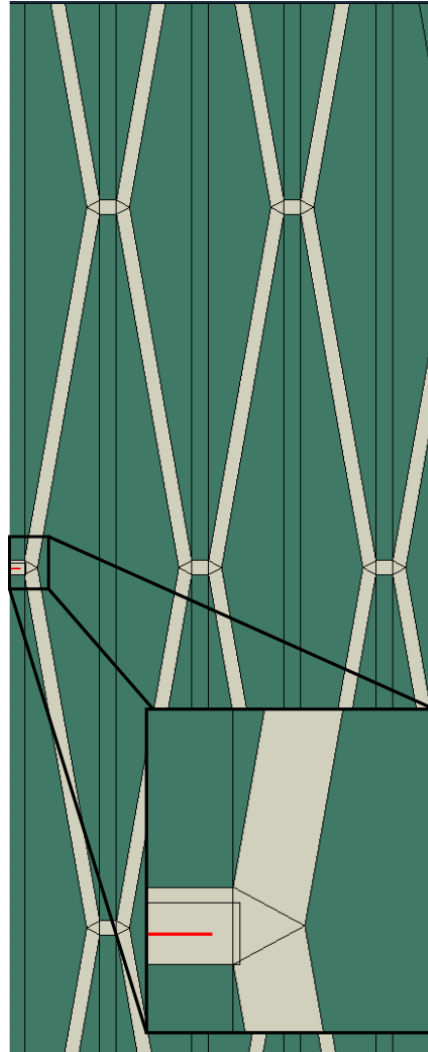


Figure 3.17 A sample with a  $50 \times 250 \mu\text{m}^2$  BSU size, where the initial crack is located inside the cement line. Note that the initial crack shifted off center to avoid perfectly mirrored symmetry.

### 3.11.2.3 Effects of BSU size based on crack location in the BSU

Based on the results of this parametric study (which are discussed in section 5.4) another smaller study was undertaken to investigate how the location of the initial crack inside the BSU affects the trabecula's ability to resist cracks for different sizes of the BSU.

Three models with BSUs of largely varying size, but constant  $w_{\text{BSU}}:h_{\text{BSU}} = 1:5$  aspect ratio ( $20 \times 100$ ,  $40 \times 200$  and  $75 \times 375 \mu\text{m}^2$ ), were tested with the crack located at different horizontal locations in the BSUs (see Figure 3.18 ). The strain to full crack propagation for each model was plotted against the distance the crack traveled through the BSU before reaching the cement line. This allowed the comparison of strain to full crack propagation between differently sized BSU while having the crack travel the same distance in the BSU.

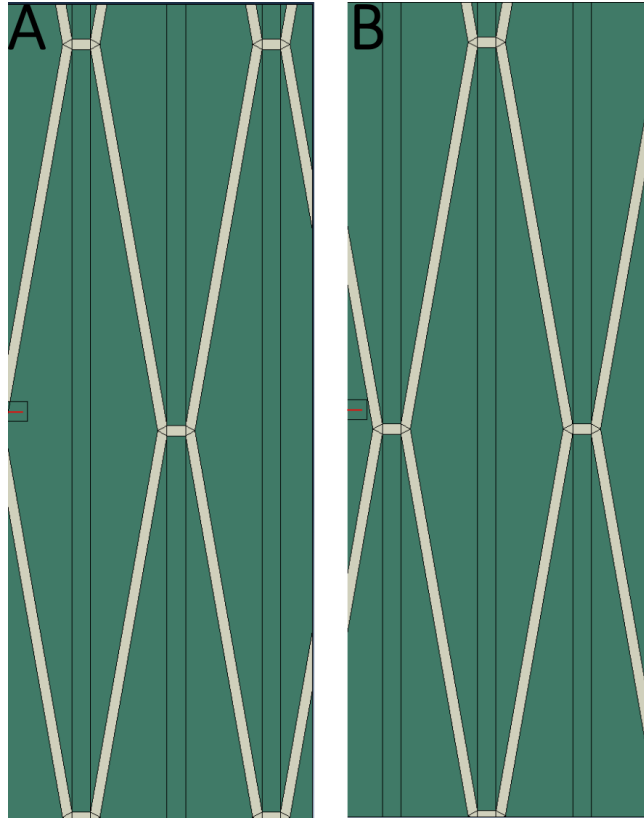


Figure 3.18 Two models with the BSU size 75X375, representing the two extremes of the initial crack location A) Initial Crack located on the right side of the BSU, forcing the crack to propagate through the entire BSU before hitting the cement line. B) Initial crack located at the left side of BSU. The crack only needs to propagate through a couple of microns of BSU before it hits the cement line.

### 3.11.3 Third parametric study

The first two studies used BSU geometries with vastly different aspect ratios. While in the first study the major axis of the hexagonal BSU was perpendicular to major axis of the trabecula; in the second study, the major axes of the BSU and the trabecula were aligned.

The third parametric study investigates how changing the aspect ratio between the two extremes affects the cement line's ability to resist crack propagation in the trabecula. For this study, a series of models were generated where the geometry of the first parametric study was sequentially morphed into the geometry of the second parametric study. The adjustable parameters for the BSU partition script were set as follows:

- $H \times W$ :  $300 \times 300 \mu\text{m}$ ;
- $h_{BSU}$ :  $50 \mu\text{m}$ ;
- $t$ :  $5 \mu\text{m}$ ;
- $\theta$ :  $60^\circ$ ; and,
- mesh size:  $1.8 \mu\text{m}$ .

A model was first taken from the first parametric study at  $\theta=60^\circ$  and was run with different QUADE strain values to simulate crack propagation both through and around the BSU. For each subsequent

model, the BSU width  $w_{BSU}$  was reduced by 20  $\mu\text{m}$  to morph the BSU dimensions closer to the 1:5 ratio that was used in the second parametric study.

For each model, the  $Y_{DIS}$  parameter was adjusted to ensure that the crack would only propagate approximately 15  $\mu\text{m}$  inside the BSU. The 15  $\mu\text{m}$  travel distance was chosen to accommodate models with small  $w_{BSU}$  values. A total of five different BSU sizes were tested with BSU dimensions ranging from 120 $\times$ 50  $\mu\text{m}$  to 40 $\times$ 50  $\mu\text{m}$ .

For each of the different BSU sizes/ratios the strain to full propagation was recorded for the crack path both around and through the BSU.

## 4 Results

The simulations for this entire study were run in batches and verified by hand to ensure that no errors or calculation artifacts occurred. Any simulations that failed to converge or produced a calculation error were either adjusted as described in section 3.10, or were completely omitted from the final results. The entire study consisted of nearly 300 successful simulations which required close to one terabyte of disk storage space. This chapter will go over the results of the simulations, starting with the validation studies and then followed by the three parametric studies examining the effects of geometry and material properties on crack growth.

### 4.1 Recreation of Gustafsson osteon model

Gustafsson et al. [53] have published 2D XFEM modelling results for an osteon, surrounded by cement line, embedded in a homogeneous solid. Their results used the dual failure criterion and serve as a validation for the failure subroutine developed and used for this thesis (see Appendix A: Fortran code). They noted that the crack path switched from passing through the osteon, to going around the osteon, for QUADE critical strain  $\varepsilon_n^0 = \varepsilon_s^0$  values of 0.0015 and 0.0016 (see Figure 4.1).

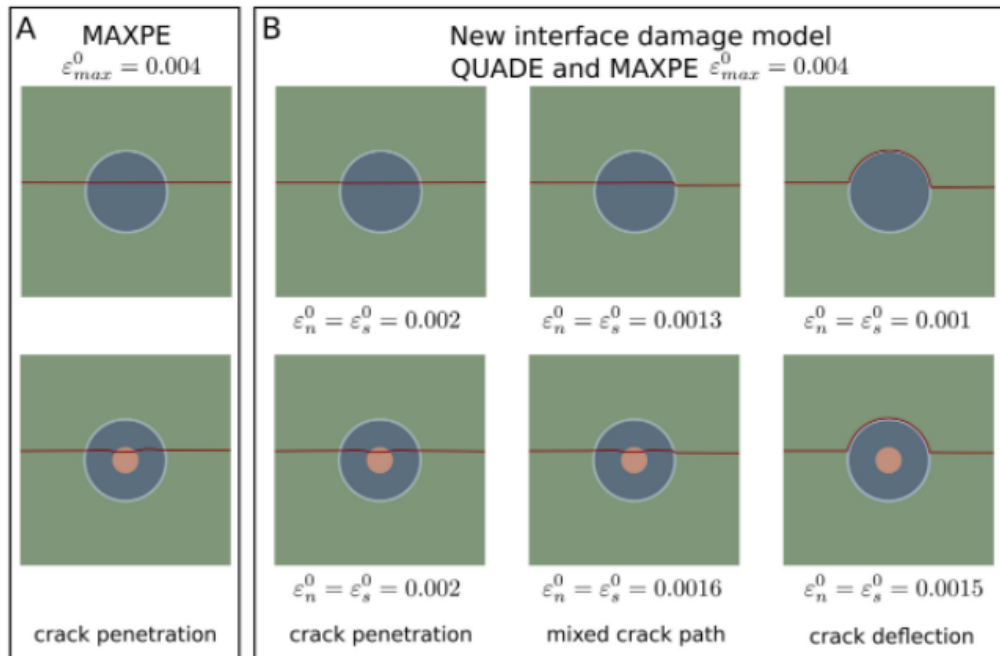


Figure 4.1 Predicted crack paths in radial models with and without Haversian canals. Crack propagation was modelled using (A) the MAXPE criterion or (B) the new interface damage criteria for different critical interface strains. Taken from [116] with permission from Elsevier

The models for an osteon in Gustafsson et al. [53] was recreated as closely as possible; however, variations in mesh size and crack location are expected because not all the information was provided in the publication. The model was tested with a range of  $\varepsilon_n^0 = \varepsilon_s^0$  values between 0.0010 and 0.0025. The changeover between the crack behavior was recorded at the QUADE values of 0.0018 and 0.0019 (see Figure 4.2). This behavior is similar to what was observed by Gustafsson et al. [53] where reducing the QUADE critical strain values allowed the crack to deflect around the osteon, while larger QUADE critical strains force the crack through the osteon. The general agreement between the two sets of results, despite the missing information regarding to the original model, suggests that the dual-failure subroutine has been implemented properly.

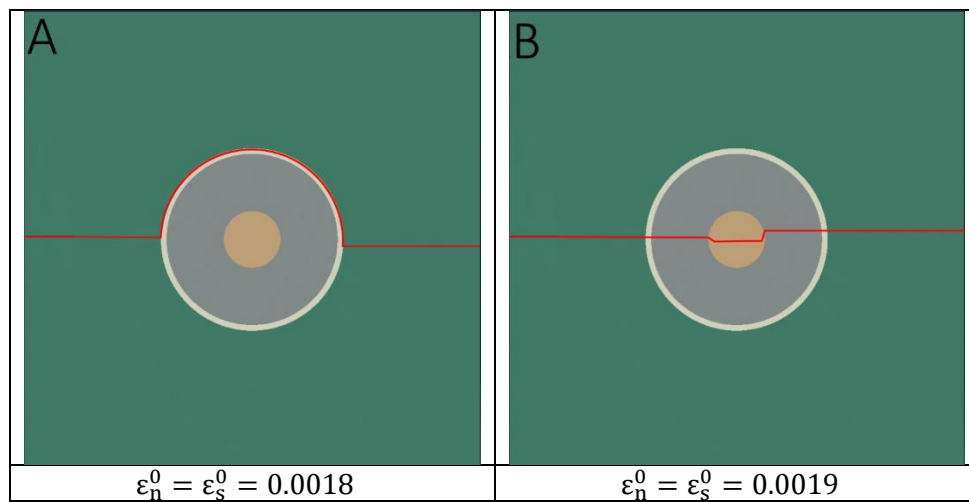


Figure 4.2 predicted crack path in radial models with Haversian canals using dual criteria method. A) Crack is deflected around the osteon via the cement line. B) crack path penetrates through the osteon.

## 4.2 Boundary condition analysis

Allowing the uppermost and lowermost nodes on the model to translate in the horizontal x-direction should produce a more homogeneous strain gradient through the sample compared with constraining x-motion. Therefore, the overall height of the sample, or the proximity of the crack to the upper and lower boundaries, is not expected to have an appreciable effect on the crack growth. This hypothesis was investigated by varying the overall height of a model.

Four different height models were used for the boundary condition analysis. As shown in Table 4.1, the strains to complete crack propagation were recorded and compared with the 200  $\mu\text{m}$  model. The largest difference in the strain at complete crack propagation was 0.21% and can be attributed to mesh differences, as increasing the area of the sample constantly shifted the mesh. It can be concluded that boundary conditions do not affect the results in a meaningful way when they are located at least 50  $\mu\text{m}$  away from the initial crack.

Table 4.1 list of strains required to propagate a crack through a sample of pure BSU material for samples with different heights 'H'.

Sample height, H ( $\mu\text{m}$ )	Sample strain ( $\times 10^{-3}$ ) to complete crack propagation	Percent difference
100	4.213	0.047%
200	4.211	0.00
400	4.220	0.21%
800	4.218	0.17%

### 4.3 Mesh analysis

The same geometry was re-meshed 50 times with element sizes from 0.5 to 3.5  $\mu\text{m}$  to determine the coarsest mesh (i.e., fewest elements and fastest simulation time) that could ensure stable results. The strains to full crack propagation from the mesh analysis simulations were all recorded and plotted against the mesh size used in the simulation (Figure 4.3).

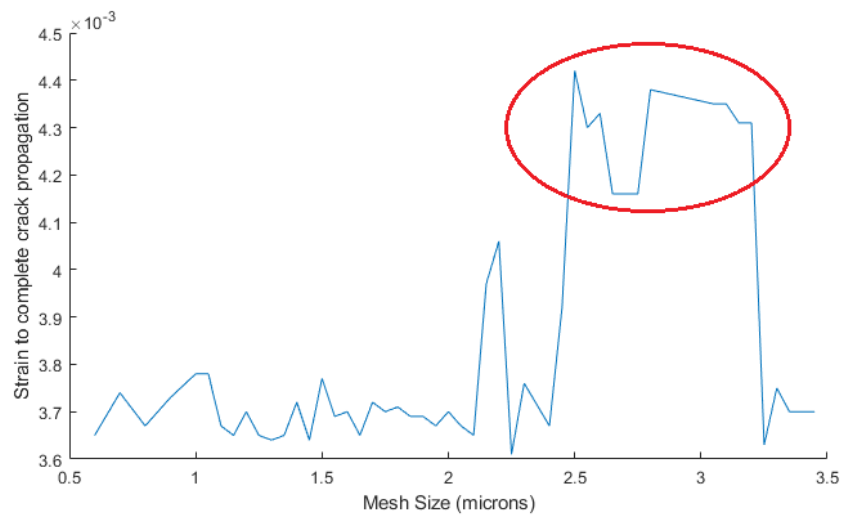


Figure 4.3: Mesh size analysis plot of strain to complete crack propagation against the mesh size used in the simulation.

For the tested geometry, the average mesh sizes below 2  $\mu\text{m}$  appears to be semi-stable with a strain to complete propagation of around  $3.7 \times 10^{-3}$ . Mesh sizes larger than 2  $\mu\text{m}$  appear to be more variable. The area circled in red is of note, as those mesh sizes caused the crack to propagate through the BSU rather than around it, causing a large difference in the crack path and the recorded strain values. Two different propagation examples can be seen in Figure 4.4. The coarser meshed model on the right represents the crack path of the models circled in red, while the more finely meshed model on the left represents the crack path of all the other models.

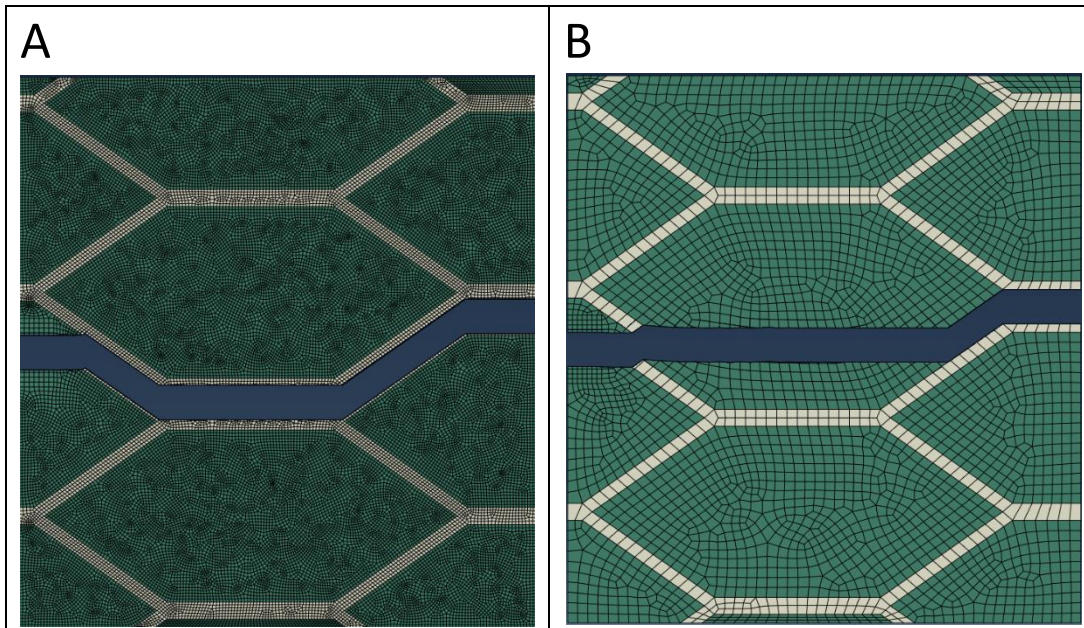


Figure 4.4 The image on the left (A) shows a finely meshed model where the crack deflects around the BSU through the cement line. The figure on the right (B) shows a coarsely meshed model where the crack propagated through the BSU rather than around it.

After further investigation, it was concluded that the variation in crack propagation is caused by the fact that when the coarser mesh is used, the cement line mesh has only a single element through its thickness. Since the crack must propagate through at least one element when the critical strain is reached, it has no choice but to propagate through the entire cement line, causing a divergence in the simulation results. This conclusion was confirmed by re-running the coarsely meshed models with increasingly smaller QUADE strain values to promote deflection around the BSU. After reducing the QUADE strain to an extremely small value of 0.0010, the crack continued to propagate through the BSU, rather than deflecting. This behaviour indicated that the change in the crack path through the sample was caused solely by the mesh size, rather than any other simulation parameters.

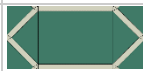
Further analysis of the results showed that even when using mesh sizes lower than  $2\ \mu\text{m}$ , a change in the mesh size could introduce variability of  $\pm 1 \times 10^{-4}$  to the macroscopic failure strain results. It was therefore decided that the mesh size should be kept constant as much as possible to reduce the potential error in the results.

An average mesh size of  $1.8\ \mu\text{m}$  was chosen as the default mesh size for all the subsequent modeling in this study. The mesh size of  $1.8\ \mu\text{m}$  provided a good balance between mesh coverage and the average simulation time. It also ensured a minimum of 3 elements through the thickness of the cement line. If the mesh size had to be adjusted for a particular simulation due to convergence or meshing errors, the change was strictly kept between  $1.7$  and  $1.9\ \mu\text{m}$ .

#### 4.4 First parametric study: effects of QUADE critical strain and angles of deflection on crack path in a 2D representation of a trabecula

The values of the BSU angle ( $\theta$ ) and the QUADE critical strain values ( $\varepsilon_n^0 = \varepsilon_s^0$ ) were varied to determine the interaction of these two parameters. Table 4.2 shows the strain to full crack propagation for  $\theta=40-80^\circ$  at seven different QUADE critical strain values. Each result is also color coded based on the crack propagation path that was observed in that simulation.

Table 4.2 Strain required for complete crack propagation [ $\times 10^{-3}$ ] for a range of BSU side angles  $\theta$  at multiple QUADE strain values. The transition between the two crack propagation paths is shown with the use of different colors.

	BSU side angle $\theta$ [°]								
	40	45	50	55	60	65	70	75	80
QUADE Strain									
0.0015	5.02	5.02	5.04	4.96	4.90	5.15	4.87	4.89	4.22
0.002	5.02	5.02	5.04	4.95	4.92	4.95	4.86	4.89	4.22
0.003	5.02	5.02	4.91	4.92	4.96	4.94	4.15	4.13	4.22
0.004	5.01	5.04	4.91	5.02	4.99	4.29	4.07	4.13	4.22
0.005	5.00	4.99	5.05	4.33	4.15	4.29	4.07	4.13	4.22
0.006	5.05	4.97	4.61	4.33	4.15	4.29	4.07	4.13	4.22
0.007	5.05	4.97	4.61	4.33	4.15	4.29	4.07	4.13	4.22
Deflection of the crack around the BSU.			Mixed propagation with both penetration through BSU and deflection around the BSU.				Propagation through the BSU with no deflection.		

#### 4.5 Second parametric study: effects of size of the BSU on the overall crack resistance of the trabeculae

This second parametric study, which examined the effects of BSU size on crack growth, consisted of multiple sets of data. The first set looked at how the size of the BSU affected strain to full crack propagation in a sample with a mixed crack propagation path (see section 3.11.2.1). A total of 35 differently sized BSUs ranged from 15x75 to 75x375  $\mu\text{m}$  were tested; however, two simulations were discarded due to convergence issues, reducing the number of usable simulations to 33. The strain to full crack propagation was recorded and plotted against BSU length in Figure 4.5. The plot shows a general trend of increased crack resistance in bigger BSUs.

When analyzing the crack propagation at different time steps throughout the simulations, it was noticed that the macroscopic strain build-up only occurs during propagation through the BSU; the cement line contributes nothing to the trabecula's ability to resist crack propagation. This observation suggests that the trend in Figure 4.5 is based only on the initial propagation distance of the crack through the BSU, rather than the BSU's actual size. It is important to note, however, that the distance the crack travels in the BSU is linked to the size of the BSU, as bigger BSUs have more material through which the crack must travel. By calculating the distance that the crack travels through the BSU before reaching the cement line, and then plotting strain over that distance, the trend becomes more visible, as can be seen in Figure 4.6.

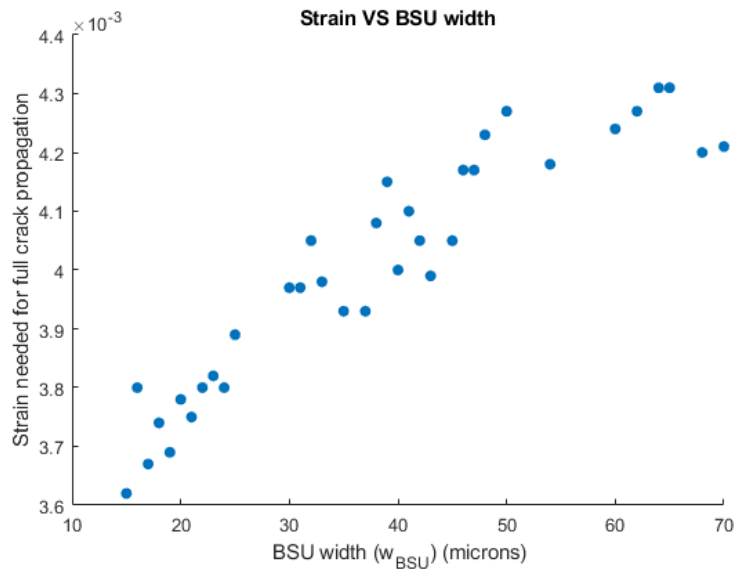


Figure 4.5: Plot of strain to full crack propagation over the BSU width  $w_{BSU}$  based on results from the second parametric study.

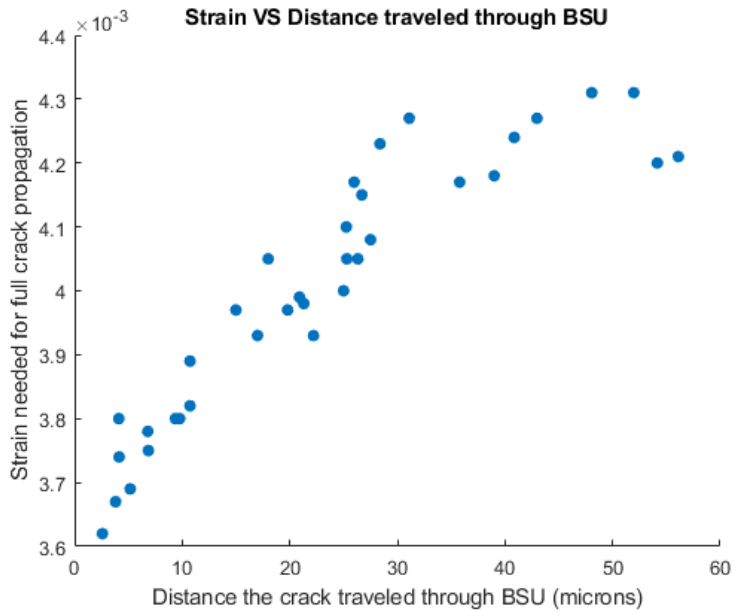


Figure 4.6: Plot of strain to full crack propagation over the distance the crack traveled in the BSU based on results from the second parametric study.

The second data set of this parametric study investigated how the BSU and cement line contribute to the overall crack resistance of trabeculae. Five different models with varying BSU sizes (see section 3.11.2.2), but a constant 1:5 BSU aspect ratio, were chosen out of the first data set and tested with only propagation through the BSU (pure propagation) and only deflection around the BSU (pure deflection). The tabulated results of the second data set can be seen in Table 4.3.

Table 4.3 Comparison of strain ( $\times 10^{-3}$ ) to complete crack propagation between different crack paths in five differently sized BSUs. Data for mixed propagation is taken from the first data set.

Failure Mode	BSU Size ( $\mu\text{m} \times \mu\text{m}$ )				
	60×300	50×250	40×200	30×150	20×100
Pure deflection	2.89	2.91	2.93	2.87	2.92
Mixed propagation	4.24	4.27	4.00	3.97	3.78
Pure propagation	4.43	4.40	4.41	4.37	4.38

In the third data set, three models with BSUs of varying sizes, but constant aspect ratio, were tested with the crack located at different horizontal locations in the BSUs (see section 3.11.2.3) in order to vary the distance the crack must travel to reach the cement line. The macroscopic strain to full crack propagation for each model was plotted against the distance the crack traveled through the BSU in microns (see Figure 4.7).

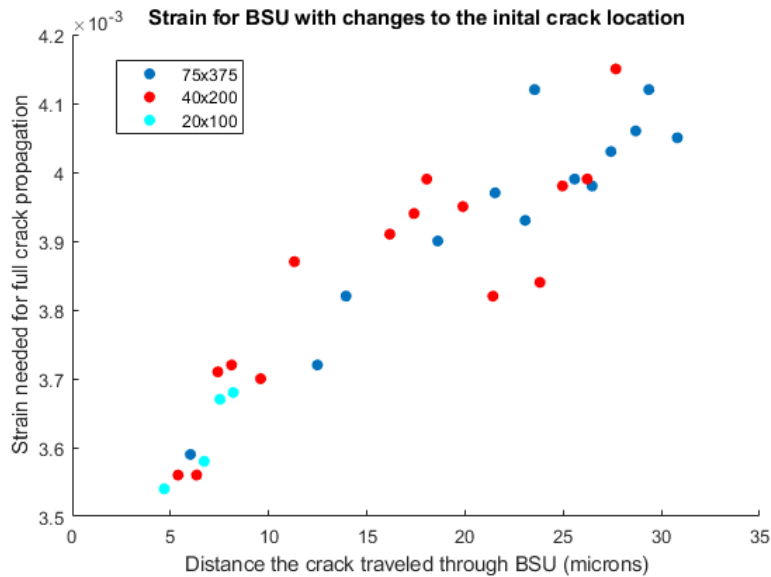


Figure 4.7 Plot of strain to full crack propagation over the distance the crack traveled in the BSU in three different BSU sizes. based on results from the second parametric study.

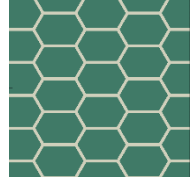
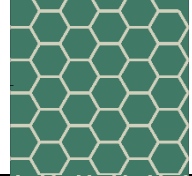
#### 4.6 Third parametric study: effects of the BSU geometry on the overall crack response in the cement line

The first two parametric studies have each shown a different strain response to cracks deflecting around the BSUs along the cement line compared to those that pass through the BSUs. In the first study, the crack deflection was beneficial to the trabeculae’s ability to resist cracks (i.e., macroscopic strain to failure increased); however, the opposite was true for the second study. Based on these results it was hypothesized that the change in BSU aspect ratio was responsible for the different trends observed in the two studies. The third parametric study was therefore undertaken to confirm that a change in the BSU geometry can cause a fundamental change in the strain response of the trabeculae sample.

Since the aspect ratio was the biggest change in the geometry between the first two studies, a sample from the first parametric study was altered by holding  $w_{BSU}$  constant and varying  $h_{BSU}$ . The two crack paths (through and around the BSU) were obtained for each model by varying the QUADE values.

Table 4.4 shows the collected data, while Figure 4.8 shows the plot of the strain to complete crack propagation, for the five trabeculae geometries versus the QUADE critical strain values. A transition in behaviour is noted between 100×50 and 80×50, where crack propagation around the BSU is beneficial for the former (i.e., higher macroscopic strain at failure) but detrimental in the latter.

Table 4.4 A collection of strains ( $\times 10^{-3}$ ) at complete crack propagation for the crack paths through and around the BSU for different BSU aspect ratios. Note that images of the samples show the BSU partitions before the adjustment of parameter  $Y_{DIS}$ . As such, the BSU partitions are not properly aligned to the initial crack location.

Image of sample	BSU dimensions ( $\mu\text{m}\times\mu\text{m}$ )	Propagation Around BSU		Propagation Through BSU	
		$\varepsilon_n^0 = \varepsilon_s^0$ (0.003)	$\varepsilon_n^0 = \varepsilon_s^0$ (0.004)	$\varepsilon_n^0 = \varepsilon_s^0$ (0.005)	$\varepsilon_n^0 = \varepsilon_s^0$ (0.006)
	120×50	5.00	5.00	4.19	4.18
	100×50	4.95	4.96	4.22	4.22
	80×50	4.02	4.02	4.14	4.14
	60×50	4.07	4.07	4.17	4.17
	40×50	4.04	4.04	4.18	4.18

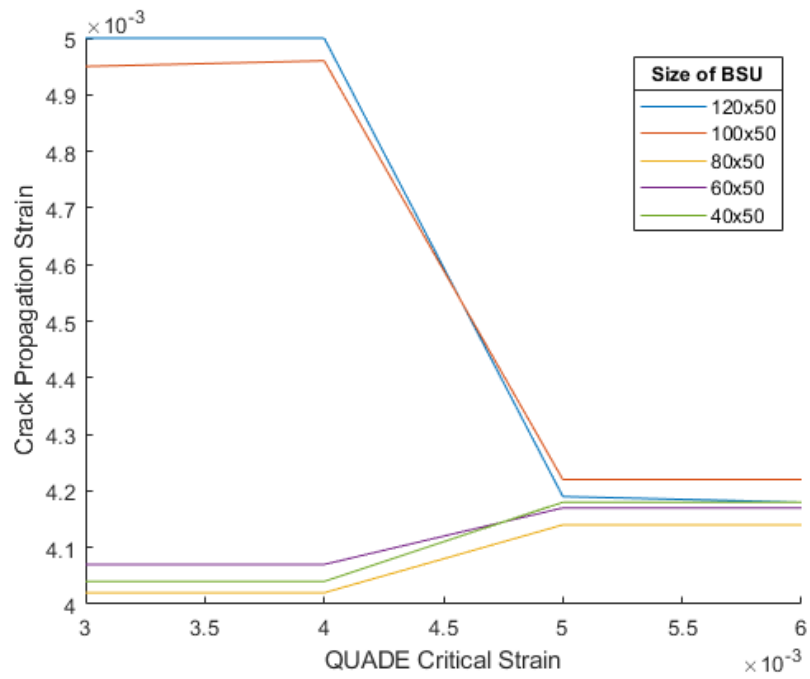


Figure 4.8 Plot of the strain response to change in crack path for different size ratios of BSUs. From left to right the crack path changes from deflection around the BSU to propagation through the BSU.

## 5 Discussion and conclusion

Cheap and reliable ways to assess fracture risk are crucial when it comes to helping the aging population. Though fracture risk assessment methods based on the bone quantity exist, they are sometimes insufficient when it comes to identifying patients with high risk of bone fracture.

Recent studies have identified microscopic changes in BSU with age. Two-dimensional image analysis has shown that BSU length, width, and area all decrease with age and deteriorating architecture [28]. These measures could be combined with existing bone quantity parameters to develop more accurate methods for identifying patients with high risk of bone fracture. However, the mechanistic effects of these changes in BSU size must first be understood. Does the higher proportion of cement line associated with smaller BSU inhibit crack growth through blunting or redirection? Or is more cement line, which is thought to be more brittle, detrimental to the overall strength by providing more potential paths for crack growth?

The goal of this study was to apply XFEM methods that were previously used to simulate crack propagation in cortical bone to understand the role of BSU size and geometry in the trabeculae's ability to resist crack propagation. This chapter summarizes the work completed in this study and discusses the importance of the findings based on the initial goals of this thesis.

### 5.1 Suitability of XFEM for analysis of crack propagation in trabecular bone

XFEM analysis has been used in a number of previous studies to simulate crack propagation in cortical bone with great success. In this study, it has again proven to be an effective tool, when combined with the dual damage criteria method, for predicting realistic crack propagation patterns in 2D representations of trabecular bone. XFEM was particularly well suited for the kinds of parametric studies conducted for this thesis, as it did not require selecting a predetermined crack path. Overall, the XFEM method is well suited for accurately simulating crack propagation in 2D samples of trabecular bone. Nevertheless, some issues were uncovered during the study that are worth noting.

Due to the unpredictability of the XFEM crack propagation, simulation of large numbers of different models was tedious and time consuming. For approximately 70% of the models, the crack tended to loop back on itself during the simulation, rather than propagating across the model, prompting an intervention from the researcher to manually adjust the geometry or mesh of the sample. These user-provided adjustments proved time consuming when working with a large number of models and simulations. For future studies, it is highly recommended that the damage subroutine be improved to reduce unwanted crack behavior by limiting the turn angles and travel directions of the propagating crack.

### 5.2 Identification of critical strain values

Based on the results of the first parametric study (Section 4.4), when the QUADE critical strain values are lowered, the crack is encouraged to follow the cement line, deflecting around the BSU. This deflection response is similar to the behaviour that was previously observed in cortical bone, where lowering QUADE critical strain values also caused the crack to deflect around osteon. Therefore, QUADE critical strains can be used to govern what path the crack will take during a simulation.

According to data in Table 4.2, increasing the BSU side angle  $\theta$  appears to reduce the likelihood of the crack deflection around the BSU, as it takes a larger reduction in the QUADE critical strain for the crack to change its path from penetration to deflection. This results intuitively makes sense as steeper deflection angles would require the crack to expend more energy to achieve.

In conclusion, QUADE critical strains play a crucial role in determining the path the crack takes when propagating through a trabecula. However, the results also show that the QUADE values at which the crack path transitions from BSU deflection to BSU propagation is heavily reliant on the geometry of the BSU. The side angle of the idealized hexagonal BSU was found to be one of the most important variables in determining the QUADE values at which the crack path switch occurs. Based on the results of the first parametric study, the QUADE strain values for the transition point between the two crack paths can range from  $1.5 \times 10^{-3}$  to  $7.0 \times 10^{-3}$  based solely on the angle at which the crack meets the BSU. Steeper deflection angles are harder to achieve, and as such they require smaller QUADE values for the deflection to occur.

Since the QUADE critical values for the crack path transition rely heavily on the geometry, it is recommended to perform a parametric study for each new geometry in future studies to ensure suitable parameters are being used.

### 5.3 Effects of the cement line deflections on the microscopic strain to failure

Based on the data in the first parametric study (section 4.4), the deflections around the BSUs provide an increase in the trabeculae's ability to resist crack propagation, as deflecting cracks require the sample to undergo a larger strain for the crack to achieve full propagation. In other words, the deflection caused by the cement lines appeared to be beneficial.

However, after the geometry of the BSU was adjusted to better represent real life BSU (section 4.5), the deflections around the BSUs became detrimental to the trabeculae's ability to resist cracking. This sudden change in how the cement line fundamentally affects the trabeculae and its ability to resist cracks prompted a third parametric study which tried to bridge the gap between the different geometries used in the first two parametric studies.

The results of the third parametric study (Section 4.6) show that deflections caused by the cement line in trabeculae can be either beneficial or detrimental, depending on the geometry of the BSUs. In the two widest BSU samples which were tested in the study (see Figure 4.8), the strain to complete crack propagation becomes larger when the crack path switches from penetration through the BSU to deflection around the BSU. The other three BSU sizes show a slight decrease in the strain during the crack path switchover. This difference in the strain response to crack deflection fundamentally changes the crack resistance properties of the BSU.

In summary, though this study provides results based on idealized geometry, the fact that the fundamental role of the cement line is heavily dependent on the geometry may mean that the use of simplified BSUs may simply not be feasible. The results of this thesis may require further validation with the use of less idealized 2D representations of BSUs.

5.4 Effects of reduction in BSU size on the trabeculae's ability to resist cracking  
Based on the results of the second parametric study (section 4.5), the BSU size was found to have a significant affect on the trabeculae's ability to resist cracking during mixed crack propagation. The cement lines were found to be detrimental in resisting cracks. As such, larger BSU sizes tended to keep the crack tips away from the cement lines for longer, requiring a higher strain for a complete crack propagation to occur.

The data in Table 4.3 shows that propagation through the cement line drastically reduces the macroscopic strain required to propagate cracks through the trabeculae. While a crack propagation without deflection around any of the BSUs required a strain of approximately  $4.4 \times 10^{-3}$  to achieve full crack propagation regardless of the BSU size. A crack propagation through the cement line required a strain of only about  $2.9 \times 10^{-3}$  to achieve the same result, once again regardless of the BSU size. These two types of propagation can be considered as the two extremes, where pure BSU propagation is the best-case scenario, and the pure cement line propagation is the worse-case scenario. Therefore, mixed crack propagation can be considered as a combination of the two other propagations. The ratio between the two types of propagation is dependent on the size of the plate, and the width of the BSU that the crack is forced to propagate through at the start of the simulation.

As such, having the crack propagate through BSU as much as possible became an effective way to increase the trabeculae's ability to resist cracking. Simply having larger BSUs showed no particular benefit when the distance the crack traveled through the BSU was standardized between different BSU sizes (Figure 4.7); however, larger BSUs provide longer best-case scenario crack propagation before the crack tip reached the weak cement line.

In conclusion, though the size of the BSU does not slow propagation once a crack reaches the cement line, the larger BSUs will keep the crack tip away from the cement lines for longer, providing a higher crack resistance to the trabeculae.

## 5.5 Limitations

This study has a few limitations that should be noted here. The entire study was completed using 2D geometry which does not necessarily represent the complex interactions between their 3D counterparts. Furthermore, the chosen geometry (hexagonal BSUs) was highly idealized and did not vary in size or shape throughout a given model.

Though a significant amount of time was dedicated to finding accurate material properties in previous literature, the broad spectrum of conflicting or simply missing data on the topic forced the study to make many assumptions about the properties of BSU and cement line. Further simplifications of material properties also included BSU homogeneity. In reality, each BSU would have a unique shape, lamellar orientation, and mineralization level based on when it was added to the skeleton. The study also simplified usually anisotropic BSUs into an isotropic material.

One final limitation is that the trabeculae were idealized as rectangular bars subjected to uniaxial tension. The true shape of trabeculae is obviously much more complicated and these shapes, and their variability, needs to be incorporated into numerical models. Cyclic bending is likely more representative of a typical loading scenario in the skeleton and should be investigated in the future. Nevertheless, uniaxial tension provides a simple, easily reproduced boundary condition for this initial attempt at understanding the effects of trabecular microstructure on crack growth.

## 5.6 Clinical implications

Though this study only provides preliminary results, the parametric analyses from this thesis indicate that it might be possible to use BSU size as a predictive parameter when identifying fracture risk in patients. Using the BSU size together with other qualitative and quantitative parameters to predict fracture risk will most likely increase the accuracy of the current detection methods. However, before these new parameters can be implemented into our fracture risk evaluation methods, further research must be undertaken to better understand the effects of these parameters on the overall properties of the bone.

## 5.7 Future work

The goal for these studies was to perform an initial investigation of XFEM crack modeling in trabecular bone at the micron magnification to identify the effects of reduction in BSU size on the trabeculae's ability to resist crack propagation. As mentioned in the previous section, the simulations described in this study are highly idealized; future work should focus on adopting the methods from this study to simulate crack propagation in more realistic models of trabeculae. Since it would be extremely time consuming to generate realistic BSU structures by hand, effort should be spent on developing algorithms that can automatically generate random life-like representations of trabecular microstructures

Future studies should also focus on identifying exact material properties for both the BSU and the cement line in trabecular bone. Though there exist a number of sources for material properties of trabecular bone, the variation in the provided values is extremely high, and as such they might not be accurate for the purposes of crack simulation in trabecular bone.

Other crack modeling techniques should also be researched to identify the ideal method for simulating cracks in trabecular bone. At the time of this study, phase-field damage models are an active research field with very little established biomechanical applications. In the future it might be a strong replacement for XFEM analysis in trabecular bone. Furthermore, recent studies show development in particle-based models that can prove useful as an alternative to continuum-based approaches [122].

Finally, as computing power increases, it might also soon be possible to efficiently run 3D simulations of crack propagation in trabecular bone. The jump from 2D to 3D should provide an enormous leap in accuracy, due to the added complexity of the simulation. However, given the importance of BSU geometry shown in this thesis, some real 3D data of trabecular microstructure will be needed to ensure that any model is representative of reality.

## 5.8 Conclusion

The primary objective of this thesis was to try to answer the fundamental question of "how does the reduction of the BSU size in trabeculae affect crack propagation in trabecular bone on the microscopic level?".

While recognizing the limitations of this study, based on the data collected, the effects of the size of BSU were found to depend heavily on the type of crack propagation that a trabecula experiences. The resistance to cracking in trabeculae was found to be weakest when the crack propagates purely through cement line. On the other hand, propagation purely through the BSU without deflection provided the highest crack resistance. These two types of propagation can be considered as the two extremes, for which the size of the BSU has no effect on the strain required for complete crack propagation.

However, mixed crack propagation contains both propagation through cement line and BSU, and the ratio between the two is mostly dependent on the size of the BSU. As such, a trabecula's ability to resist cracking in mixed crack propagation is heavily dependent on the size of the BSU. Bigger BSUs keep the crack tip away from the weak cement lines for longer, giving the trabecula the ability to sustain larger strain deformations without completely cracking.

Since mixed propagation is more likely to occur than the two extremes, it is concluded that on average, larger BSUs will provide more crack resistance to trabeculae when compared to smaller BSUs.

## References

- [1] Hernlund E, Svedbom A, Ivergård M, Compston J, Cooper C, Stenmark J, McCloskey EV, Jönsson B, Kanis JA. Osteoporosis in the European Union: medical management, epidemiology and economic burden. *Archives of Osteoporosis*. 2013;8(1):136. doi:10.1007/s11657-013-0136-1
- [2] Rachner TD, Khosla S, Hofbauer LC. Osteoporosis: now and the future. *The Lancet*. 2011;377(9773):1276–1287. doi:10.1016/S0140-6736(10)62349-5
- [3] Poole KES, Compston JE. Osteoporosis and its management. *BMJ*. 2006;333(7581):1251–1256. doi:10.1136/bmj.39050.597350.47
- [4] Burge R, Dawson-Hughes B, Solomon DH, Wong JB, King A, Tosteson A. Incidence and economic burden of osteoporosis-related fractures in the United States, 2005-2025. *Journal of Bone and Mineral Research: The Official Journal of the American Society for Bone and Mineral Research*. 2007;22(3):465–475. doi:10.1359/jbmr.061113
- [5] Currey JD. *Bones: Structure and Mechanics*. Princeton University Press; 2002.
- [6] Cowin SC, editor. *Bone Mechanics Handbook*. 2nd ed. Boca Raton: CRC Press; 2013. doi:10.1201/b14263
- [7] Chen H, Zhou X, Fujita H, Onozuka M, Kubo K-Y. Age-Related Changes in Trabecular and Cortical Bone Microstructure. *International Journal of Endocrinology*. 2013;2013:e213234. doi:10.1155/2013/213234
- [8] Pasco JA, Seeman E, Henry MJ, Merriman EN, Nicholson GC, Kotowicz MA. The population burden of fractures originates in women with osteopenia, not osteoporosis. *Osteoporosis International*. 2006;17(9):1404–1409. doi:10.1007/s00198-006-0135-9
- [9] Kanis JA, Cooper C, Rizzoli R, Reginster J-Y, on behalf of the Scientific Advisory Board of the European Society for Clinical and Economic Aspects of Osteoporosis (ESCEO) and the Committees of Scientific Advisors and National Societies of the International Osteoporosis Foundation (IOF). European guidance for the diagnosis and management of osteoporosis in postmenopausal women. *Osteoporosis International*. 2019;30(1):3–44. doi:10.1007/s00198-018-4704-5
- [10] Brett AD, Brown JK. Quantitative computed tomography and opportunistic bone density screening by dual use of computed tomography scans. *Journal of Orthopaedic Translation*. 2015;3(4):178–184. doi:10.1016/j.jot.2015.08.006
- [11] Bone Mass Measurement: What the Numbers Mean | NIH Osteoporosis and Related Bone Diseases National Resource Center. [accessed 2022 Mar 7]. <https://www.bones.nih.gov/health-info/bone/bone-health/bone-mass-measure>
- [12] Wainwright SA, Marshall LM, Ensrud KE, Cauley JA, Black DM, Hillier TA, Hochberg MC, Vogt MT, Orwoll ES. Hip Fracture in Women without Osteoporosis. *The Journal of Clinical Endocrinology & Metabolism*. 2005;90(5):2787–2793. doi:10.1210/jc.2004-1568

- [13] Odén A, McCloskey EV, Johansson H, Kanis JA. Assessing the Impact of Osteoporosis on the Burden of Hip Fractures. *Calcified Tissue International*. 2013;92(1):42–49. doi:10.1007/s00223-012-9666-6
- [14] NIH Consensus Development Panel on Osteoporosis Prevention D and Therapy. Osteoporosis Prevention, Diagnosis, and Therapy. *JAMA*. 2001;285(6):785–795. doi:10.1001/jama.285.6.785
- [15] Kandola A. FRAX score: What is it, and what do the results mean? 2020 Mar 12 [accessed 2022 Mar 7]. <https://www.medicalnewstoday.com/articles/frax-score>
- [16] Roland J. FRAX Score: Calculator, Meaning, and More. Healthline. 2017 Dec 8 [accessed 2022 Mar 7]. <https://www.healthline.com/health/frax-score>
- [17] Taylor D, Hazenberg JG, Lee TC. Living with cracks: Damage and repair in human bone. *Nature Materials*. 2007;6(4):263–268. doi:10.1038/nmat1866
- [18] Launey ME, Buehler MJ, Ritchie RO. On the Mechanistic Origins of Toughness in Bone. *Annual Review of Materials Research*. 2010;40(1):25–53. doi:10.1146/annurev-matsci-070909-104427
- [19] Grynblas M. Age and disease-related changes in the mineral of bone. *Calcified Tissue International*. 1993;53(1):S57–S64. doi:10.1007/BF01673403
- [20] Wang X, Shen X, Li X, Mauli Agrawal C. Age-related changes in the collagen network and toughness of bone. *Bone*. 2002;31(1):1–7. doi:10.1016/S8756-3282(01)00697-4
- [21] Cui W-Q, Won Y-Y, Baek M-H, Lee D-H, Chung Y-S, Hur J-H, Ma Y-Z. Age-and region-dependent changes in three-dimensional microstructural properties of proximal femoral trabeculae. *Osteoporosis International*. 2008;19(11):1579–1587. doi:10.1007/s00198-008-0601-7
- [22] Ding M, Hvid I. Quantification of age-related changes in the structure model type and trabecular thickness of human tibial cancellous bone. *Bone*. 2000;26(3):291–295. doi:10.1016/S8756-3282(99)00281-1
- [23] Macdonald HM, Nishiyama KK, Kang J, Hanley DA, Boyd SK. Age-related patterns of trabecular and cortical bone loss differ between sexes and skeletal sites: A population-based HR-pQCT study. *Journal of Bone and Mineral Research*. 2011;26(1):50–62. doi:10.1002/jbmr.171
- [24] Gong H, Zhang M, Yeung HY, Qin L. Regional variations in microstructural properties of vertebral trabeculae with aging. *Journal of Bone and Mineral Metabolism*. 2005;23(2):174–180. doi:10.1007/s00774-004-0557-4
- [25] Chen H, Shoumura S, Emura S, Bunai Y. Regional variations of vertebral trabecular bone microstructure with age and gender. *Osteoporosis International*. 2008;19(10):1473–1483. doi:10.1007/s00198-008-0593-3
- [26] Hamed E, Jasiuk I, Yoo A, Lee Y, Liszka T. Multi-scale modelling of elastic moduli of trabecular bone. *Journal of The Royal Society Interface*. 2012;9(72):1654–1673. doi:10.1098/rsif.2011.0814
- [27] Owen R, Reilly G. In vitro Models of Bone Remodelling and Associated Disorders. *Frontiers in Bioengineering and Biotechnology*. 2018;6:134. doi:10.3389/fbioe.2018.00134

- [28] Lamarche BA. Morphometric changes with age in human trabecular bone structural units (BSU) of the lumbar spine [Thesis]. Laurentian University of Sudbury; 2020. <https://zone.biblio.laurentian.ca/jspui/handle/10219/3616>
- [29] Skedros JG, Holmes JL, Vajda EG, Bloebaum RD. Cement lines of secondary osteons in human bone are not mineral-deficient: New data in a historical perspective. *The Anatomical Record Part A: Discoveries in Molecular, Cellular, and Evolutionary Biology*. 2005;286A(1):781–803. doi:10.1002/ar.a.20214
- [30] Budyn É, Hoc T. Analysis of micro fracture in human Haversian cortical bone under transverse tension using extended physical imaging. *International Journal for Numerical Methods in Engineering*. 2010;82(8):940–965. doi:10.1002/nme.2791
- [31] Mechanical properties and histology of cortical bone from younger and older men - Evans - 1976 - *The Anatomical Record* - Wiley Online Library. [accessed 2022 Feb 2]. <https://anatomypubs.onlinelibrary.wiley.com/doi/abs/10.1002/ar.1091850102>
- [32] Johannesdottir F, Allaire B, Bouxsein ML. Fracture Prediction by Computed Tomography and Finite Element Analysis: Current and Future Perspectives. *Current Osteoporosis Reports*. 2018;16(4):411–422. doi:10.1007/s11914-018-0450-z
- [33] Viceconti M, Qasim M, Bhattacharya P, Li X. Are CT-Based Finite Element Model Predictions of Femoral Bone Strengthening Clinically Useful? *Current Osteoporosis Reports*. 2018;16(3):216–223. doi:10.1007/s11914-018-0438-8
- [34] Hernandez CJ, van der Meulen MC. Understanding Bone Strength Is Not Enough. *Journal of Bone and Mineral Research*. 2017;32(6):1157–1162. doi:10.1002/jbmr.3078
- [35] Reznikov N, Bilton M, Lari L, Stevens MM, Kröger R. Fractal-like hierarchical organization of bone begins at the nanoscale. *Science*. 2018;360(6388):eaao2189. doi:10.1126/science.aao2189
- [36] Rho J-Y, Kuhn L, Zioupos P. Mechanical Properties and the Hierarchical Structure of Bone. *Medical engineering & physics*. 1998;20:92–102. doi:10.1016/S1350-4533(98)00007-1
- [37] McNally EA, Schwarcz HP, Botton GA, Arsenault AL. A Model for the Ultrastructure of Bone Based on Electron Microscopy of Ion-Milled Sections. *PLOS ONE*. 2012;7(1):e29258. doi:10.1371/journal.pone.0029258
- [38] Burr DB, Allen MR. *Basic and Applied Bone Biology*. Academic Press; 2019.
- [39] Yeni YN, Norman TL. Calculation of porosity and osteonal cement line effects on the effective fracture toughness of cortical bone in longitudinal crack growth. *Journal of Biomedical Materials Research*. 2000;51(3):504–509. doi:10.1002/1097-4636(20000905)51:3<504::AID-JBM27>3.0.CO;2-I
- [40] Dempster D, Lindsay R, Dempster, Lindsay. Pathogenesis of osteoporosis. *The Lancet*. 1993;341(8848):797–801. doi:10.1016/0140-6736(93)90570-7
- [41] Parfitt AM. Trabecular bone architecture in the pathogenesis and prevention of fracture. *The American Journal of Medicine*. 1987;82(1, Supplement 2):68–72. (Medical Management of Cardiovascular Hypertensive, and Metabolic). doi:10.1016/0002-9343(87)90274-9

- [42] Sözen T, Özişik L, Başaran NÇ. An overview and management of osteoporosis. *European Journal of Rheumatology*. 2017;4(1):46–56. doi:10.5152/eurjrheum.2016.048
- [43] Nalla RK, Kruzic JJ, Kinney JH, Ritchie RO. Effect of aging on the toughness of human cortical bone: evaluation by R-curves. *Bone*. 2004;35(6):1240–1246. doi:10.1016/j.bone.2004.07.016
- [44] Goda I, Ganghoffer J-F. Identification of couple-stress moduli of vertebral trabecular bone based on the 3D internal architectures. *Journal of the Mechanical Behavior of Biomedical Materials*. 2015;51:99–118. doi:10.1016/j.jmbbm.2015.06.036
- [45] Chan KS, Chan CK, Nicolella DP. Relating crack-tip deformation to mineralization and fracture resistance in human femur cortical bone. *Bone*. 2009;45(3):427–434. doi:10.1016/j.bone.2009.01.468
- [46] Evans FG, Bang S. Differences and relationships between the physical properties and the microscopic structure of human femoral, tibial and fibular cortical bone. *American Journal of Anatomy*. 1967;120(1):79–88. doi:10.1002/aja.1001200107
- [47] Evans FG. Mechanical properties and histology of cortical bone from younger and older men. *The Anatomical Record*. 1976;185(1):1–11. doi:10.1002/ar.1091850102
- [48] Koester KJ, Ager JW, Ritchie RO. The true toughness of human cortical bone measured with realistically short cracks. *Nature Materials*. 2008;7(8):672–677. doi:10.1038/nmat2221
- [49] Mohsin S, O'Brien FJ, Lee TC. Osteonal crack barriers in ovine compact bone. *Journal of Anatomy*. 2006;208(1):81–89. doi:10.1111/j.1469-7580.2006.00509.x
- [50] O'Brien FJ, Taylor D, Clive Lee T. The effect of bone microstructure on the initiation and growth of microcracks. *Journal of Orthopaedic Research*. 2005;23(2):475–480. doi:10.1016/j.orthres.2004.08.005
- [51] O'Brien FJ, Taylor D, Clive Lee T. Bone as a composite material: The role of osteons as barriers to crack growth in compact bone. *International Journal of Fatigue*. 2007;29(6):1051–1056. doi:10.1016/j.ijfatigue.2006.09.017
- [52] Zimmermann EA, Schaible E, Gludovatz B, Schmidt FN, Riedel C, Krause M, Vettorazzi E, Acevedo C, Hahn M, Püschel K, et al. Intrinsic mechanical behavior of femoral cortical bone in young, osteoporotic and bisphosphonate-treated individuals in low- and high energy fracture conditions. *Scientific Reports*. 2016;6(1):21072. doi:10.1038/srep21072
- [53] Gustafsson A. The role of microstructure for crack propagation in cortical bone [thesis/doccomp]. Lund University; 2019. <http://lup.lub.lu.se/record/d8243c0b-5dbb-4ea2-8893-af997801e0f6>
- [54] Montalbano T, Feng G. Nanoindentation characterization of the cement lines in ovine and bovine femurs. *Journal of Materials Research*. 2011;26(8):1036–1041. doi:10.1557/jmr.2011.46
- [55] Frasca P. Scanning-Electron Microscopy Studies of 'Ground Substance' in the Cement Lines, Resting Lines, Hypercalcified Rings and Reversal Lines of Human Cortical Bone. *Cells Tissues Organs*. 1981;109(2):115–121. doi:10.1159/000145373

- [56] Burr DB, Schaffler MB, Frederickson RG. Composition of the cement line and its possible mechanical role as a local interface in human compact bone. *Journal of Biomechanics*. 1988;21(11):939–945. doi:10.1016/0021-9290(88)90132-7
- [57] Gupta HS, Stachewicz U, Wagermaier W, Roschger P, Wagner HD, Fratzl P. Mechanical modulation at the lamellar level in osteonal bone. *Journal of Materials Research*. 2006;21(8):1913–1921. doi:10.1557/jmr.2006.0234
- [58] Langer M, Pacureanu A, Suhonen H, Grimal Q, Cloetens P, Peyrin F. X-Ray Phase Nanotomography Resolves the 3D Human Bone Ultrastructure. *PLOS ONE*. 2012;7(8):e35691. doi:10.1371/journal.pone.0035691
- [59] Milovanovic P, vom Scheidt A, Mletzko K, Sarau G, Püschel K, Djuric M, Amling M, Christiansen S, Busse B. Bone tissue aging affects mineralization of cement lines. *Bone*. 2018;110:187–193. doi:10.1016/j.bone.2018.02.004
- [60] Dong XN, Guo XE. Geometric Determinants to Cement Line Debonding and Osteonal Lamellae Failure in Osteon Pushout Tests. *Journal of Biomechanical Engineering*. 2004;126(3):387–390. doi:10.1115/1.1762901
- [61] Oftadeh R, Perez-Viloria M, Villa-Camacho JC, Vaziri A, Nazarian A. Biomechanics and Mechanobiology of Trabecular Bone: A Review. *Journal of Biomechanical Engineering*. 2015 [accessed 2022 Mar 21];137(1). <https://doi.org/10.1115/1.4029176>. doi:10.1115/1.4029176
- [62] Townsend PR, Rose RM, Radin EL. Buckling studies of single human trabeculae. *Journal of Biomechanics*. 1975;8(3):199–201. doi:10.1016/0021-9290(75)90025-1
- [63] Lievers WB, Poljsak AS, Waldman SD, Pilkey AK. Effects of dehydration-induced structural and material changes on the apparent modulus of cancellous bone. *Medical Engineering & Physics*. 2010;32(8):921–925. doi:10.1016/j.medengphy.2010.06.001
- [64] Zysset PK, Guo XE, Hoffler CE, Moore KE, Goldstein SA. Elastic modulus and hardness of cortical and trabecular bone lamellae measured by nanoindentation in the human femur. *Journal of Biomechanics*. 1999;32(10):1005–1012. doi:10.1016/s0021-9290(99)00111-6
- [65] Turner CH, Rho J, Takano Y, Tsui TY, Pharr GM. The elastic properties of trabecular and cortical bone tissues are similar: results from two microscopic measurement techniques. *Journal of Biomechanics*. 1999;32(4):437–441. doi:10.1016/s0021-9290(98)00177-8
- [66] Rho J-Y, Tsui TY, Pharr GM. Elastic properties of human cortical and trabecular lamellar bone measured by nanoindentation. *Biomaterials*. 1997;18(20):1325–1330. doi:10.1016/S0142-9612(97)00073-2
- [67] Chevalier Y, Pahr D, Allmer H, Charlebois M, Zysset P. Validation of a voxel-based FE method for prediction of the uniaxial apparent modulus of human trabecular bone using macroscopic mechanical tests and nanoindentation. *Journal of Biomechanics*. 2007;40(15):3333–3340. doi:10.1016/j.jbiomech.2007.05.004
- [68] Hoffler CE, Moore KE, Kozloff K, Zysset PK, Goldstein SA. Age, gender, and bone lamellae elastic moduli. *Journal of Orthopaedic Research*. 2000;18(3):432–437. doi:10.1002/jor.1100180315

- [69] Zysset PK, Goulet RW, Hollister SJ. A Global Relationship Between Trabecular Bone Morphology and Homogenized Elastic Properties. *Journal of Biomechanical Engineering*. 1998;120(5):640–646. doi:10.1115/1.2834756
- [70] Rho JY, Roy ME, Tsui TY, Pharr GM. Elastic properties of microstructural components of human bone tissue as measured by nanoindentation. *Journal of Biomedical Materials Research*. 1999;45(1):48–54. doi:10.1002/(sici)1097-4636(199904)45:1<48::aid-jbm7>3.0.co;2-5
- [71] Brennan O, Kennedy OD, Lee TC, Rackard SM, O'Brien FJ. Biomechanical properties across trabeculae from the proximal femur of normal and ovariectomised sheep. *Journal of Biomechanics*. 2009;42(4):498–503. doi:10.1016/j.jbiomech.2008.11.032
- [72] Lips P, Courpron P, Meunier PJ. Mean wall thickness of trabecular bone packets in the human iliac crest: Changes with age. *Calcified Tissue Research*. 1978;26(1):13–17. doi:10.1007/BF02013227
- [73] Lamarche BA, Thomsen JS, Andreasen CM, Lievers WB, Andersen TL. 2D size of trabecular bone structure units (BSU) correlate more strongly with 3D architectural parameters than age in human vertebrae. *Bone*. 2022;160:116399. doi:10.1016/j.bone.2022.116399
- [74] Ming-Yuan H, Hutchinson JW. Crack deflection at an interface between dissimilar elastic materials. *International Journal of Solids and Structures*. 1989;25(9):1053–1067. doi:10.1016/0020-7683(89)90021-8
- [75] Barenblatt GI. The formation of equilibrium cracks during brittle fracture. General ideas and hypotheses. Axially-symmetric cracks. *Journal of Applied Mathematics and Mechanics*. 1959;23(3):622–636. doi:10.1016/0021-8928(59)90157-1
- [76] de Vree JHP, Brekelmans WAM, van Gils MAJ. Comparison of nonlocal approaches in continuum damage mechanics. *Computers & Structures*. 1995;55(4):581–588. doi:10.1016/0045-7949(94)00501-S
- [77] Donaldson F, Ruffoni D, Schneider P, Levchuk A, Zwahlen A, Pankaj P, Müller R. Modeling microdamage behavior of cortical bone. *Biomechanics and Modeling in Mechanobiology*. 2014;13(6):1227–1242. doi:10.1007/s10237-014-0568-6
- [78] Khoei AR. *Extended Finite Element Method: Theory and Applications*. John Wiley & Sons; 2014.
- [79] Haider IT, Goldak J, Frei H. Femoral fracture load and fracture pattern is accurately predicted using a gradient-enhanced quasi-brittle finite element model. *Medical Engineering & Physics*. 2018;55:1–8. doi:10.1016/j.medengphy.2018.02.008
- [80] Bettamer A, Hambli R, Allaoui S, Almhdie-Imjabber A. Using visual image measurements to validate a novel finite element model of crack propagation and fracture patterns of proximal femur. *Computer Methods in Biomechanics and Biomedical Engineering: Imaging & Visualization*. 2017;5(4):251–262. doi:10.1080/21681163.2015.1079505
- [81] Hambli R, Bettamer A, Allaoui S. Finite element prediction of proximal femur fracture pattern based on orthotropic behaviour law coupled to quasi-brittle damage. *Medical Engineering & Physics*. 2012;34(2):202–210. doi:10.1016/j.medengphy.2011.07.011

- [82] Hambli R. A quasi-brittle continuum damage finite element model of the human proximal femur based on element deletion. *Medical & Biological Engineering & Computing*. 2013;51(1):219–231. doi:10.1007/s11517-012-0986-5
- [83] Marco M, Giner E, Caeiro-Rey JR, Miguélez MH, Larraínzar-Garijo R. Numerical modelling of hip fracture patterns in human femur. *Computer Methods and Programs in Biomedicine*. 2019;173:67–75. doi:10.1016/j.cmpb.2019.03.010
- [84] Giner E, Belda R, Arango C, Vercher-Martínez A, Tarancón JE, Fuenmayor FJ. Calculation of the critical energy release rate  $G_c$  of the cement line in cortical bone combining experimental tests and finite element models. *Engineering Fracture Mechanics*. 2017;184:168–182. doi:10.1016/j.engfracmech.2017.08.026
- [85] Miehe C, Welschinger F, Hofacker M. Thermodynamically consistent phase-field models of fracture: Variational principles and multi-field FE implementations. *International Journal for Numerical Methods in Engineering*. 2010;83(10):1273–1311. doi:10.1002/nme.2861
- [86] Bourdin B, Francfort GA, Marigo J-J. The Variational Approach to Fracture. *Journal of Elasticity*. 2008;91(1):5–148. doi:10.1007/s10659-007-9107-3
- [87] Bourdin B, Francfort GA, Marigo J-J. Numerical experiments in revisited brittle fracture. *Journal of the Mechanics and Physics of Solids*. 2000;48(4):797–826. doi:10.1016/S0022-5096(99)00028-9
- [88] Shen R, Waisman H, Yosibash Z, Dahan G. A novel phase field method for modeling the fracture of long bones. *International Journal for Numerical Methods in Biomedical Engineering*. 2019;35(8):e3211. doi:10.1002/cnm.3211
- [89] Gültekin O, Dal H, Holzapfel GA. Numerical aspects of anisotropic failure in soft biological tissues favor energy-based criteria: A rate-dependent anisotropic crack phase-field model. *Computer Methods in Applied Mechanics and Engineering*. 2018;331:23–52. doi:10.1016/j.cma.2017.11.008
- [90] Gültekin O, Dal H, Holzapfel GA. A phase-field approach to model fracture of arterial walls: Theory and finite element analysis. *Computer Methods in Applied Mechanics and Engineering*. 2016;312:542–566. (Phase Field Approaches to Fracture). doi:10.1016/j.cma.2016.04.007
- [91] Gültekin O, Dal H, Holzapfel GA. Crack phase-field modeling of anisotropic rupture in fibrous soft tissues. *CIMNE*; 2017. p. 139–150. <https://upcommons.upc.edu/handle/2117/180603>
- [92] Wu C, Fang J, Zhang Z, Entezari A, Sun G, Swain MV, Li Q. Fracture modeling of brittle biomaterials by the phase-field method. *Engineering Fracture Mechanics*. 2020;224:106752. doi:10.1016/j.engfracmech.2019.106752
- [93] Gustafsson A, Isaksson H. Phase field models of interface failure for bone application - evaluation of open-source implementations. *Theoretical and Applied Fracture Mechanics*. 2022 Jun 7:103432. doi:10.1016/j.tafmec.2022.103432
- [94] Luo Q, Nakade R, Dong X, Rong Q, Wang X. Effect of mineral–collagen interfacial behavior on the microdamage progression in bone using a probabilistic cohesive finite element model. *Journal of the Mechanical Behavior of Biomedical Materials*. 2011;4(7):943–952. doi:10.1016/j.jmbbm.2011.02.003

- [95] Maghsoudi-Ganjeh M, Lin L, Wang X, Zeng X. Computational investigation of ultrastructural behavior of bone using a cohesive finite element approach. *Biomechanics and Modeling in Mechanobiology*. 2019;18(2):463–478. doi:10.1007/s10237-018-1096-6
- [96] Mischinski S, Ural A. Finite Element Modeling of Microcrack Growth in Cortical Bone. *Journal of Applied Mechanics*. 2011 [accessed 2022 Mar 22];78(4). <https://doi.org/10.1115/1.4003754>. doi:10.1115/1.4003754
- [97] An B, Zhang D. An analysis of crack growth in dentin at the microstructural scale. *Journal of the Mechanical Behavior of Biomedical Materials*. 2018;81:149–160. doi:10.1016/j.jmbbm.2018.02.029
- [98] Mischinski S, Ural A. Interaction of microstructure and microcrack growth in cortical bone: a finite element study. *Computer Methods in Biomechanics and Biomedical Engineering*. 2013;16(1):81–94. doi:10.1080/10255842.2011.607444
- [99] Wang M, Zimmermann EA, Riedel C, Busse B, Li S, Silberschmidt VV. Effect of micro-morphology of cortical bone tissue on fracture toughness and crack propagation. *Procedia Structural Integrity*. 2017;6:64–68. (XXVII International Conference «Mathematical and Computer Simulation in Mechanics of Solids and Structures. Fundamentals of static and dynamic fracture», MCM 2017, 25–27 September 2017, Saint-Petersburg, Russia). doi:10.1016/j.prostr.2017.11.010
- [100] Xu X-P, Needleman A. Numerical simulations of fast crack growth in brittle solids. *Journal of the Mechanics and Physics of Solids*. 1994;42(9):1397–1434. doi:10.1016/0022-5096(94)90003-5
- [101] Mirzaei M, Alavi F, Allaveisi F, Naeini V, Amiri P. Linear and nonlinear analyses of femoral fractures: Computational/experimental study. *Journal of Biomechanics*. 2018;79:155–163. doi:10.1016/j.jbiomech.2018.08.003
- [102] Ural A, Mischinski S. Multiscale modeling of bone fracture using cohesive finite elements. *Engineering Fracture Mechanics*. 2013;103:141–152. (Advances in Failure Assessment Using Fracture and Damage Mechanics.). doi:10.1016/j.engfracmech.2012.05.008
- [103] Belytschko T, Black T. Elastic crack growth in finite elements with minimal remeshing. *International Journal for Numerical Methods in Engineering*. 1999;45(5):601–620. doi:10.1002/(SICI)1097-0207(19990620)45:5<601::AID-NME598>3.0.CO;2-S
- [104] Melenk JM, Babuška I. The partition of unity finite element method: Basic theory and applications. *Computer Methods in Applied Mechanics and Engineering*. 1996;139(1):289–314. doi:10.1016/S0045-7825(96)01087-0
- [105] Song J-H, Areias PMA, Belytschko T. A method for dynamic crack and shear band propagation with phantom nodes. *International Journal for Numerical Methods in Engineering*. 2006;67(6):868–893. doi:10.1002/nme.1652
- [106] Budyn E, Hoc T, Jonvaux J. Fracture strength assessment and aging signs detection in human cortical bone using an X-FEM multiple scale approach. *Computational Mechanics*. 2008;42(4):579–591. doi:10.1007/s00466-008-0283-1

- [107] Raeisi Najafi A, Arshi AR, Eslami MR, Fariborz S, Moeinzadeh MH. Micromechanics fracture in osteonal cortical bone: A study of the interactions between microcrack propagation, microstructure and the material properties. *Journal of Biomechanics*. 2007;40(12):2788–2795. doi:10.1016/j.jbiomech.2007.01.017
- [108] Raeisi Najafi A, Arshi AR, Saffar KP, Eslami MR, Fariborz S, Moeinzadeh MH. A fiber-ceramic matrix composite material model for osteonal cortical bone fracture micromechanics: Solution of arbitrary microcracks interaction. *Journal of the Mechanical Behavior of Biomedical Materials*. 2009;2(3):217–223. doi:10.1016/j.jmbbm.2008.06.003
- [109] Budyn É, Hoc T. Multiple scale modeling for cortical bone fracture in tension using X-FEM. *European Journal of Computational Mechanics*. 2007;16(2):213–236. doi:10.3166/remn.16.213-236
- [110] Abdel-Wahab AA, Maligno AR, Silberschmidt VV. Micro-scale modelling of bovine cortical bone fracture: Analysis of crack propagation and microstructure using X-FEM. *Computational Materials Science*. 2012;52(1):128–135. (Proceedings of the 20th International Workshop on Computational Mechanics of Materials - IWCMM 20). doi:10.1016/j.commat.2011.01.021
- [111] Idkaidek A, Jasiuk I. Cortical bone fracture analysis using XFEM – case study. *International Journal for Numerical Methods in Biomedical Engineering*. 2017;33(4):e2809. doi:10.1002/cnm.2809
- [112] Idkaidek A, Koric S, Jasiuk I. Fracture analysis of multi-osteon cortical bone using XFEM. *Computational Mechanics*. 2018;62(2):171–184. doi:10.1007/s00466-017-1491-3
- [113] Li S, Abdel-Wahab A, Demirci E, Silberschmidt VV. Fracture process in cortical bone: X-FEM analysis of microstructured models. In: Bigoni D, Carini A, Gei M, Salvadori A, editors. *Fracture Phenomena in Nature and Technology*. Cham: Springer International Publishing; 2014. p. 43–55. doi:10.1007/978-3-319-04397-5\_5
- [114] Rodriguez-Florez N, Carriero A, Shefelbine SJ. The use of XFEM to assess the influence of intra-cortical porosity on crack propagation. *Computer Methods in Biomechanics and Biomedical Engineering*. 2017;20(4):385–392. doi:10.1080/10255842.2016.1235158
- [115] Feerick EM, Liu X (Cheryl), McGarry P. Anisotropic mode-dependent damage of cortical bone using the extended finite element method (XFEM). *Journal of the Mechanical Behavior of Biomedical Materials*. 2013;20:77–89. doi:10.1016/j.jmbbm.2012.12.004
- [116] Gustafsson A, Khayyeri H, Wallin M, Isaksson H. An interface damage model that captures crack propagation at the microscale in cortical bone using XFEM. *Journal of the Mechanical Behavior of Biomedical Materials*. 2019;90:556–565. doi:10.1016/j.jmbbm.2018.09.045
- [117] Hammond MA, Wallace JM, Allen MR, Siegmund T. Mechanics of linear microcracking in trabecular bone. *Journal of Biomechanics*. 2019;83:34–42. doi:10.1016/j.jbiomech.2018.11.018
- [118] Salem M, Westover L, Adeeb S, Duke K. Prediction of failure in cancellous bone using extended finite element method. *Proceedings of the Institution of Mechanical Engineers, Part H: Journal of Engineering in Medicine*. 2020;234(9):988–999. doi:10.1177/0954411920936057
- [119] Salem M. Investigation of pelvic bone fracture mechanism and simulated treatment. :153.

- [120] Abaqus User Subroutines Reference Guide (6.13). [accessed 2022 Jul 7].  
<http://130.149.89.49:2080/v6.13/books/sub/default.htm?startat=ch01s01asb26.html>
- [121] Abaqus Analysis User's Manual (6.10). [accessed 2022 Jun 22].  
<http://130.149.89.49:2080/v6.10/books/usb/default.htm?startat=pt04ch10s06at33.html>
- [122] Sun H, Ferasat K, Nowak P, Gravelle L, Gaffran N, Anderson C, Sirola T, Pintar O, Lievers WB, Kim IY, et al. Implementing a non-local lattice particle method in the open-source large-scale atomic/molecular massively parallel simulator. *Modelling and Simulation in Materials Science and Engineering*. 2022;30(5):054001. doi:10.1088/1361-651X/ac6b4a
- [123] Cancellous bone label QS:Lit, "tessuto osseo spugnoso". 29/09/2019.  
[https://commons.wikimedia.org/wiki/File:Spongy\\_bone\\_-\\_Trabecular\\_bone\\_-\\_Normal\\_trabecular\\_bone\\_Trabecular\\_bone\\_etc\\_--\\_Smart-Servier\\_%28cropped%29.jpg](https://commons.wikimedia.org/wiki/File:Spongy_bone_-_Trabecular_bone_-_Normal_trabecular_bone_Trabecular_bone_etc_--_Smart-Servier_%28cropped%29.jpg)

## Appendix A: Fortran code for the cement line UDMGINI subroutine

```

SUBROUTINE UDMGINI (FINDEX, NFINDEX, FNORMAL, NDI, NSHR, NTENS, PROPS,
1 NPROPS, STATEV, NSTATEV, STRESS, STRAIN, STRAINEE, LXFEM, TIME,
2 DTIME, TEMP, DTEMP, PREDEF, DPRED, NFIELD, COORDS, NOEL, NPT,
3 KLAYER, KSPT, KSTEP, INC, KDIRCYC, KCYCLELCF, TIMECYC, SSE, SPD,
4 SCD, SVD, SMD, JMAC, JMATYP, MATLAYO, LACCFLA, CELENT, DROT, ORI)
C
C      INCLUDE 'ABA_PARAM.INC'
CC
C      DIMENSION FINDEX (NFINDEX), FNORMAL (NDI, NFINDEX), COORDS (*),
1 STRESS (NTENS), STRAIN (NTENS), STRAINEE (NTENS), PROPS (NPROPS),
2 STATEV (NSTATEV), PREDEF (NFIELD), DPRED (NFIELD), TIME (2),
3 JMAC (*), JMATYP (*), DROR (3, 3), ORI (3, 3)

C      DIMENSION PS (3), AN (3, 3), WT (6)
C      PS (1)=0.0
C      PS (2)=0.0
C      PS (3)=0.0

C
C ROTATE THE STRAIN TO GLOBAL SYSTEM IF THERE IS ORIENTATION
C
C      CALL ROTSIG (STRAIN, ORI, WT, 2, NDI, NSHR)
C
C MAXIMUM PRINCIPAL STRAIN CRITERION
C
C      CALL SPRIND (STRAIN, PS, AN, 2, NDI, NSHR)
C      SIG1 = PS (1)
C      KMAX=1
C      DO K1 = 2, NDI
C          IF (PS (K1) .GT. SIG1) THEN
C              SIG1 = PS (K1)
C              KMAX = K1
C          END IF
C      END DO
C      FINDEX (1) = SIG1/PROPS (1)
C      DO K1=1, NDI
C          FNORMAL (K1, 1) = AN (KMAX, K1)
C      END DO

C
C QUADRATIC separation-interaction CRITERION
C
C      FINDEX (2) = (STRAIN (1) / PROPS (2)) ** 2.0 + (STRAIN (NDI+1) /
$      PROPS (3)) ** 2.0
C
C      FINDEX (2) = sqrt (FINDEX (2))
C
C      DO K1=1, NDI
C          FNORMAL (K1, 2) = ORI (K1, 1)
C      END DO
C      RETURN
C      END

```

## Appendix B: Python script for trabecular geometry generation

This section will go over the python script that was used to generate the hexagonal BSU geometry. The code will be broken into parts for better clarity. When each function is called for the first time in the script, the function itself will also be provided. The function names are highlighted in yellow, and the functions themselves are shaded in light gray for clarity.

```
#params that can be edited

meshSize=1.8
displacementLoad=10
height = 375 #height of the hex
width = 75 #width of the hex
plateHeight = 400.0
plateWidth = 150.0
thickness_CL = 5.0 #Thickness of the cement line
shiftDown = height*1.5+2
shiftRight = 62
angle=80

#params that should not be edited!!!!
angleWidth=(height/2)/(math.tan(angle*math.pi/180))
layerShift = 0
sheetSize = max(plateHeight, plateWidth) * 3
changeInHight = (height + thickness_CL) / 2
angleForm = (thickness_CL- math.cos(angle*math.pi/180)* thickness_CL/2)/
math.sin(angle*math.pi/180)
crackHeight= (plateHeight / 2)
changeInWidth = (width+(width-angleWidth-angleWidth))+(2*angleForm)

creatPartPlate(sheetSize,plateWidth,plateHeight)
```

---

```
def creatPartPlate(sheetSize,plateWidth,plateHeight):

    mdb.models['Model-1'].ConstrainedSketch(name='__profile__',
sheetSize=sheetSize)

    mdb.models['Model-1'].sketches['__profile__'].rectangle(point1=(0.0,
0.0), point2=(plateWidth, plateHeight))

    mdb.models['Model-1'].Part(dimensionality=TWO_D_PLANAR, name='Plate',
type=DEFORMABLE_BODY)

    mdb.models['Model-1'].parts['Plate'].BaseShell(sketch= mdb.models['Model-
1'].sketches['__profile__'])

del mdb.models['Model-1'].sketches['__profile__']
```

---

```

# The following section of code partitions the created plate into a set of
# tiled hexagons with a specified offset
# The code below is a set of nested loops that draw a hexagon starting from
# the bottom left corner. Each iteration of the i loop draws an additional hex
# in the current row.
# Each iteration of the j loop shifts up to the next row, and offsets the row
# horizontally for proper tiling
# The cement line is also partitioned at the same time, to reduce the number
# of loops.

```

```

mdb.models['Model-1'].ConstrainedSketch(gridSpacing=5, name='__profile__',
sheetSize=sheetSize, transform=mdb.models['Model-
1'].parts['Plate'].MakeSketchTransform(sketchPlane=mdb.models['Model-
1'].parts['Plate'].faces.findAt((0.1, 0.1, 0.0), (0.0, 0.0, 1.0)),
sketchPlaneSide=SIDE1, sketchOrientation=RIGHT, origin=(0.0, 0.0, 0.0)))

```

```

mdb.models['Model-
1'].parts['Plate'].projectReferencesOntoSketch(filter=COPLANAR_EDGES,
sketch=mdb.models['Model-1'].sketches['__profile__'])

```

```

for j in range(0, int((plateHeight / height * 2 )+5)):

```

```

    for i in range(0, int(plateWidth / width / 2 + 4)):

```

```

        point=creatHexPoints(changeInWidth, changeInHight, layerShift,
shiftDown, shiftRight, j, i, width, height,angleWidth)

```

```

        drawHex(point,thickness_CL)

```

```

        partitionCL(changeInWidth, changeInHight, layerShift, shiftDown,
shiftRight, j, i, width, height, point)

```

```

        if (j % 2) == 1:

```

```

            layerShift = 0

```

```

        else:

```

```

            layerShift = (angleWidth-width) - angleForm

```

```

mdb.models['Model-1'].sketches['__profile__'].rectangle(point1=(0.0,
crackHeight-5), point2=(10.0, crackHeight+5))

```

```

mdb.models['Model-1'].parts['Plate'].PartitionFaceBySketch(faces=
mdb.models['Model-1'].parts['Plate'].faces.findAt(((0.1, 0.1,0.0), )),
sketch=mdb.models['Model-1'].sketches['__profile__'])

```

```

del mdb.models['Model-1'].sketches['__profile__']

```

---

```

def creatHexPoints(changeInWidth, changeInHeight, layerShift, shiftDown,
shiftRight, j, i, width, height,angleWidth):

    point_1 = (changeInWidth * i + layerShift - shiftRight, height +
changeInHeight * j - shiftDown)
    point_2 = (angleWidth + changeInWidth * i + layerShift - shiftRight,
height * 1.5 + changeInHeight * j - shiftDown)
    point_3 = (width-angleWidth + changeInWidth * i + layerShift -
shiftRight, height * 1.5 + changeInHeight * j - shiftDown)
    point_4 = (width + changeInWidth * i + layerShift - shiftRight, height +
changeInHeight * j - shiftDown)
    point_5 = (width-angleWidth + changeInWidth * i + layerShift -
shiftRight, height * .5 + changeInHeight * j - shiftDown)
    point_6 = (angleWidth + changeInWidth * i + layerShift - shiftRight,
height * .5 + changeInHeight * j - shiftDown)
    point = [point_1, point_2, point_3, point_4, point_5, point_6, point_1]
    return (point)

```

---

```

def drawHex(point,thickness_CL):
    for k in range(0, 6):
        mdb.models['Model-1'].sketches['__profile__'].Line(point1=(point[k]),
point2=(point[k + 1]))
        mdb.models['Model-
1'].sketches['__profile__'].Line(point1=(point[5]),point2=((point[1][0]),(poi
nt[1][1]+thickness_CL)))
        mdb.models['Model-
1'].sketches['__profile__'].Line(point1=(point[4]),point2=(point[2][0],
point[2][1] +thickness_CL))

```

---

```

def partitionCL(changeInWidth, changeInHeight, layerShift, shiftDown,
shiftRight, j, i, width, height, point):

    mdb.models['Model-1'].sketches['__profile__'].Line(point1=(point[0]),
point2=(width-angleWidth + changeInWidth * i + layerShift - shiftRight + (an
gleWidth-width) - angleForm, height * .5 + changeInHeight * (j + 1) -
shiftDown))

    mdb.models['Model-1'].sketches['__profile__'].Line(point1=(point[1]),
point2=(width + changeInWidth * i + layerShift - shiftRight + (angleWidth-
width) - angleForm, height + changeInHeight * (j + 1) - shiftDown))

    if (j != 0):
        mdb.models['Model-1'].sketches['__profile__'].Line(point1=(point[0]),
point2=(width-angleWidth + changeInWidth * i + layerShift - shiftRight + (an
gleWidth-width) - angleForm, height * 1.5 + changeInHeight * (j - 1) -
shiftDown))

        mdb.models['Model-1'].sketches['__profile__'].Line(point1=(point[5]),
point2=(width + changeInWidth * i + layerShift - shiftRight + (angleWidth-
width) - angleForm, height + changeInHeight * (j - 1) - shiftDown))

```

---

*#This section of code creates a number of sets that allow proper property, load, and mesh allocation.*

```
for j in range(0, int(plateHeight / height * 2+5)):
    for i in range(0, int(plateWidth / width / 2 + 4)):
        point=creatHexPoints(changeInWidth, changeInHight, layerShift,
shiftDown, shiftRight, j, i, width, height,angleWidth)
        creatSetBSU(point, plateHeight, plateWidth, i, j)
        creatSetAngleCementLine(point, plateHeight, plateWidth, i, j)
    if (j % 2) == 1:
        layerShift = 0
    else:
        layerShift = (angleWidth-width) - angleForm
```

*#This section deals with the 4 corners of the sample.*

```
mdb.models['Model-1'].parts['Plate'].Set(faces=mdb.models['Model-1'].parts['Plate'].faces.findAt(((0.1, plateHeight - 0.1, 0.0),), ((plateWidth - 0.1, plateHeight - 0.1, 0.0),), ((0.1, 0.1, 0.0),), ((plateWidth - 0.1, 0.1, 0.0),), ), name='Temp')
mdb.models['Model-1'].parts['Plate'].SetByBoolean(name='BSU', sets=(mdb.models['Model-1'].parts['Plate'].sets['Temp'], mdb.models['Model-1'].parts['Plate'].sets['BSU']))
mdb.models['Model-1'].parts['Plate'].Set(faces=mdb.models['Model-1'].parts['Plate'].faces.getByBoundingBox(0, crackHeight-5, 0, 10, crackHeight+5, 0), name='Temp')
mdb.models['Model-1'].parts['Plate'].SetByBoolean(name='BSU', sets=(mdb.models['Model-1'].parts['Plate'].sets['Temp'], mdb.models['Model-1'].parts['Plate'].sets['BSU']))
```

```

def creatSetBSU (point, plateHeight, plateWidth, i, j):

    if (i == 0 and j == 0):

        mdb.models['Model-1'].parts['Plate'].Set(faces=mdb.models['Model-1'].parts['Plate'].faces.findAt((-1, -1, 0.0),), name='Temp')

        mdb.models['Model-1'].parts['Plate'].Set(name='BSU', objectToCopy=mdb.models['Model-1'].parts['Plate'].sets['Temp'])

    else:

        if (point[0][0] >= 0 and point[0][1] >= 0 and point[0][0] <= plateWidth and point[0][1] <= plateHeight):

            mdb.models['Model-1'].parts['Plate'].Set(faces=mdb.models['Model-1'].parts['Plate'].faces.findAt(((point[0][0] + 0.01, point[0][1], 0.0),), ((point[1][0]+ 0.01 , point[0][1], 0.0),), ((point[2][0]+ 0.01, point[0][1], 0.0),),), name='Temp')

            mdb.models['Model-1'].parts['Plate'].SetByBoolean(name='BSU', sets=(mdb.models['Model-1'].parts['Plate'].sets['Temp'], mdb.models['Model-1'].parts['Plate'].sets['BSU']))

        elif (point[3][0] >= 0 and point[3][1] >= 0 and point[3][0] <= plateWidth and point[3][1] <= plateHeight):

            mdb.models['Model-1'].parts['Plate'].Set(faces=mdb.models['Model-1'].parts['Plate'].faces.findAt(((point[3][0] - 0.01, point[3][1], 0.0),), ((point[2][0] - 0.01, point[3][1], 0.0),), ((point[1][0] - 0.01, point[3][1], 0.0),),), name='Temp')

            mdb.models['Model-1'].parts['Plate'].SetByBoolean(name='BSU', sets=(mdb.models['Model-1'].parts['Plate'].sets['Temp'], mdb.models['Model-1'].parts['Plate'].sets['BSU']))

        if (point[1][1] >= 0 and point[1][0] >= 0 and point[1][0] <= plateWidth and point[1][1] <= plateHeight):

            mdb.models['Model-1'].parts['Plate'].Set(faces=mdb.models['Model-1'].parts['Plate'].faces.findAt(((point[1][0]+0.01, point[1][1]-0.1, 0.0),), ((point[1][0]-0.01, point[1][1]-0.1, 0.0),), ((point[2][0]+0.01, point[1][1]-0.1, 0.0),),), name='Temp')

            mdb.models['Model-1'].parts['Plate'].SetByBoolean(name='BSU', sets=(mdb.models['Model-1'].parts['Plate'].sets['Temp'], mdb.models['Model-1'].parts['Plate'].sets['BSU']))

```

```

        elif (point[2][0] >= 0 and point[2][1] >= 0 and point[2][0] <=
plateWidth and point[2][1] <= plateHeight):

            mdb.models['Model-1'].parts['Plate'].Set(faces=mdb.models['Model-
1'].parts['Plate'].faces.findAt(((point[2][0] + 0.01, point[2][1] - 0.1,
0.0),), ((point[2][0] - 0.01, point[2][1] - 0.1, 0.0),),
((point[1][0] - 0.01, point[2][1] - 0.1, 0.0),), ), name='Temp')

            mdb.models['Model-1'].parts['Plate'].SetByBoolean(name='BSU',
sets=(mdb.models['Model-1'].parts['Plate'].sets['Temp'], mdb.models['Model-
1'].parts['Plate'].sets['BSU']))

        if (point[4][0] >= 0 and point[4][1] >= 0 and point[4][0] <=
plateWidth and point[4][1] <= plateHeight):

            mdb.models['Model-1'].parts['Plate'].Set(faces=mdb.models['Model-
1'].parts['Plate'].faces.findAt(((point[4][0] + 0.01, point[4][1] + 0.1,
0.0),), ((point[4][0] - 0.01, point[4][1] + 0.1, 0.0),),
((point[5][0] - 0.01, point[4][1] + 0.1, 0.0),), ), name='Temp')

            mdb.models['Model-1'].parts['Plate'].SetByBoolean(name='BSU',
sets=(mdb.models['Model-1'].parts['Plate'].sets['Temp'], mdb.models['Model-
1'].parts['Plate'].sets['BSU']))

        elif (point[5][0] >= 0 and point[5][1] >= 0 and point[5][0] <=
plateWidth and point[5][1] <= plateHeight):

            mdb.models['Model-1'].parts['Plate'].Set(
faces=mdb.models['Model-1'].parts['Plate'].faces.findAt((point[5][0],
point[5][1] + 0.1, 0.0),), name='Temp')

            mdb.models['Model-1'].parts['Plate'].Set( faces=mdb.models[
'Model-1'].parts['Plate'].faces.findAt(((point[5][0] + 0.01, point[5][1] +
0.1, 0.0),), ((point[5][0] - 0.01, point[5][1] + 0.1, 0.0),), ((point[4][0] +
0.01, point[5][1] + 0.1, 0.0),), ), name='Temp')

            mdb.models['Model-1'].parts['Plate'].SetByBoolean(name='BSU',
sets=(mdb.models['Model-1'].parts['Plate'].sets['Temp'], mdb.models['Model-
1'].parts['Plate'].sets['BSU']))

```

```

def creatSetAngleCementLine (point, plateHeight, plateWidth, i, j):

    if (point[0][0]>=0 and point[0][1]-0.1>=0 and point[0][0]<=plateWidth and
point[0][1]<=plateHeight-0.1):

        mdb.models['Model-1'].parts['Plate'].Set(faces=mdb.models['Model-
1'].parts['Plate'].faces.findAt(((point[0][0], point[0][1]+0.1, 0.0),)),
name='TempOne')

        elif (point[1][1] - 0.1 >= 0 and point[1][0] >= 0 and point[1][0] <=
plateWidth + 0.1 and point[1][1] <= plateHeight):

            mdb.models['Model-1'].parts['Plate'].Set(faces=mdb.models['Model-
1'].parts['Plate'].faces.findAt(((point[1][0]-0.1, point[1][1], 0.0),)),
name='TempOne')

            elif (i == 0 and j == 0):

                mdb.models['Model-1'].parts['Plate'].Set(faces=mdb.models['Model-
1'].parts['Plate'].faces.findAt((-1, -1, 0.0),),name='TempOne')

                if (point[3][0]>=0 and point[3][1]-0.1>=0 and point[3][0]<=plateWidth and
point[3][1]<=plateHeight-0.1):

                    mdb.models['Model-1'].parts['Plate'].Set(faces=mdb.models['Model-
1'].parts['Plate'].faces.findAt(((point[3][0], point[3][1]+0.1, 0.0),)),
name='TempTwo')

                    elif (point[2][1] + 0.1 >= 0 and point[2][0] >= 0 and point[2][0] <=
plateWidth - 0.1 and point[2][1] <= plateHeight):

                        mdb.models['Model-1'].parts['Plate'].Set(faces=mdb.models['Model-
1'].parts['Plate'].faces.findAt(((point[2][0]+0.1, point[2][1], 0.0),)),
name='TempTwo')

                        elif (i==0 and j==0):

                            mdb.models['Model-1'].parts['Plate'].Set(faces=mdb.models['Model-
1'].parts['Plate'].faces.findAt((-1, -1, 0.0),), name='TempTwo')

                            if (i!=0 or j!=0):

                                mdb.models['Model-1'].parts['Plate'].SetByBoolean(name='CL_SetOne',
sets=(mdb.models['Model-1'].parts['Plate'].sets['TempOne'],
mdb.models['Model-1'].parts['Plate'].sets['CL_SetOne']))

                                mdb.models['Model-1'].parts['Plate'].SetByBoolean(name='CL_SetTwo',
sets=(mdb.models['Model-1'].parts['Plate'].sets['TempTwo'],
mdb.models['Model-1'].parts['Plate'].sets['CL_SetTwo']))

                                else:

                                    mdb.models['Model-1'].parts['Plate'].Set(name='CL_SetOne',
objectToCopy=mdb.models['Model-1'].parts['Plate'].sets['TempOne'])

                                    mdb.models['Model-1'].parts['Plate'].Set(name='CL_SetTwo',
objectToCopy=mdb.models['Model-1'].parts['Plate'].sets['TempTwo'])

```

```

creatSetCementLine(plateHeight, plateWidth)

creatSetsTop_Bottom_Edges(plateHeight, plateWidth)

#Cleaning up all of the temporary sets
del mdb.models['Model-1'].parts['Plate'].sets['TempTwo']
del mdb.models['Model-1'].parts['Plate'].sets['TempOne']
del mdb.models['Model-1'].parts['Plate'].sets['Temp']

#Creates a wire part that will be used as the initial crack location

creatPartCrack(crackHeight)

#Each of the modules in the Abaqus GUI wear automated, with the use of the
following functions.
#Each of the functions is as robust as I was able to make them. In theory
they can be edited to work in other projects.
setCLOrientation(angle)

creatAssembly()

setProperty()

creatStep()

creatXFEM_CrackDomain(crackHeight)

creatLoads(plateHeight, displacementLoad)

creatMesh(meshSize, plateWidth, plateHeight)

#Creates a Job

mdb.Job(atTime=None, contactPrint=OFF, description='', echoPrint=OFF,
explicitPrecision=SINGLE, getMemoryFromAnalysis=True, historyPrint=OFF,
memory=90, memoryUnits=PERCENTAGE, model='Model-1', modelPrint=OFF,
multiprocessingMode=DEFAULT, name=(str(width)+'X'+str(height)+'_angle_'+str(an
gle)+'M'+str(int(meshSize/1))+'_'+str(int(round(meshSize%1*10))))),
nodalOutputPrecision=SINGLE, numCpus=1, numGPUs=0, queue=None,
resultsFormat=ODB, scratch='', type=ANALYSIS, userSubroutine='', waitHours=0,
waitMinutes=0)

#Write an input file.

mdb.jobs[(str(width)+'X'+str(height)+'_angle_'+str(angle)+'M'+str(int(meshSiz
e/1))+'_'+str(int(round(meshSize%1*10))))].writeInput()

```

---

```
def creatSetCementLine (plateHeight, plateWidth):
    p = mdb.models['Model-1'].parts['Plate']

    c = p.faces

    faces=c.getByBoundingBox(0, 0, 0, plateWidth, plateHeight, 0)

    p.Set(faces=faces, name="Everything")

    p.SetByBoolean(name='CL_All', operation=DIFFERENCE,
sets=(p.sets['Everything'], mdb.models['Modell'].parts['Plate'].sets['BSU']))

    p.SetByBoolean(name='CL_Temp', operation=DIFFERENCE,
sets=(p.sets['CL_All'],mdb.models['Modell'].parts['Plate'].sets['CL_SetOne']
)

    p.SetByBoolean(name='CL_Straight', operation=DIFFERENCE,
sets=(p.sets['CL_Temp'],mdb.models['Modell'].parts['Plate'].sets['CL_SetTwo']
))
```

---

```
def creatSetsTop_Botttom_Edges(plateHeight, plateWidth):

    p = mdb.models['Model-1'].parts['Plate']

    c = p.edges

    edges = c.getByBoundingBox(0, plateHeight, 0, plateWidth, plateHeight, 0)

    p.Set(edges=edges, name="EdgeTop")

    edges = c.getByBoundingBox(0, 0, 0, plateWidth,0, 0)

    p.Set(edges=edges, name="EdgeBottom")
```

---

---

```

def creatPartCrack(crackHeight):

    mdb.models['Model-1'].ConstrainedSketch(name='__profile__',
sheetSize=200.0)mdb.models['Modell1'].sketches['__profile__'].Line(point1=(0.0
, crackHeight), point2=(5.0, crackHeight))

    mdb.models['Model
1'].sketches['__profile__'].HorizontalConstraint(addUndoState=False,
entity=mdb.models['Modell1'].sketches['__profile__'].geometry[2])mdb.models['M
odell1'].Part(dimensionality=TWO_D_PLANAR, name='Crack', type=DEFORMABLE_BODY)

    mdb.models['Model-1'].parts['Crack'].BaseWire(sketch=mdb.models['Model-
1'].sketches['__profile__'])

    del mdb.models['Model-1'].sketches['__profile__']

```

---

```

def setCLOrirntation(angle):

    mdb.models['Model
1'].parts['Plate'].MaterialOrientation(additionalRotationField='', additionalR
otationType=ROTATION_ANGLE, angle=90, axis=AXIS_3, fieldName='',
localCsys=None, orientationType=SYSTEM, region=mdb.models['Model-
1'].parts['Plate'].sets['CL_Straight'], stackDirection=STACK_3)

    mdb.models['Model-
1'].parts['Plate'].MaterialOrientation(additionalRotationField='', additionalR
otationType=ROTATION_ANGLE, angle=90, axis=AXIS_3, fieldName='',
localCsys=None, orientationType=SYSTEM, region=mdb.models['Model-
1'].parts['Plate'].sets['BSU'], stackDirection=STACK_3)

    mdb.models['Model-
1'].parts['Plate'].MaterialOrientation(additionalRotationField='',
additionalRotationType=ROTATION_ANGLE, angle=angle+90, axis=AXIS_3,
fieldName='', localCsys=None, orientationType=SYSTEM, region=mdb.models['Model-
1'].parts['Plate'].sets['CL_SetOne'], stackDirection=STACK_3)

    mdb.models['Model-1'].parts['Plate'].MaterialOrientation(
additionalRotationField='', additionalRotationType=ROTATION_ANGLE, angle=-
angle-90, axis=AXIS_3, fieldName='', localCsys=None, orientationType=SYSTEM,
region=mdb.models['Modell1'].parts['Plate'].sets['CL_SetTwo'], stackDirection=S
TACK_3)

```

---

```

def creatAssembly():

    mdb.models['Model-1'].rootAssembly.Instance(dependent=ON, name='Crack-1',
part=mdb.models['Model-1'].parts['Crack'])

    mdb.models['Model-1'].rootAssembly.Instance(dependent=ON, name='Plate-1',
part=mdb.models['Model-1'].parts['Plate'])

```

---

---

```

def setProperty():
    # Create material

    mdb.models['Model-1'].Material(name='BSU')

    mdb.models['Model-1'].materials['BSU'].Elastic(table=((15.0, 0.3),))

    mdb.models['Model 1'].materials['BSU'].MaxpeDamageInitiation
(table=((0.004,),))

    mdb.models['Model-1'].materials['BSU'].maxpeDamageInitiation
.DamageEvolution(table=((0.2,),), type=ENERGY)

    mdb.models['Model-1'].Material(name='Cement Line')

    mdb.models['Model-1'].materials['Cement Line'].Elastic(table=((18.0,
0.3),))

    mdb.models['Model-1'].materials['Cement Line'].MaxpeDamageInitiation
(table=((0.004,),))

    mdb.models['Model-1'].materials['Cement Line'].maxpeDamageInitiation
.DamageEvolution(table=((0.2,),), type=ENERGY)

    # Create section

    mdb.models['Model-1'].HomogeneousSolidSection(material='BSU', name='BSU',
thickness=None)

    mdb.models['Model-1'].HomogeneousSolidSection(material='Cement Line',
name='Cement Line', thickness=None)

    # Assign Section
    mdb.models['Model-1'].parts['Plate'].SectionAssignment(offset=0.0,
offsetField='', offsetType=MIDDLE_SURFACE, region=mdb.models['Model-
1'].parts['Plate'].sets['BSU'], sectionName='BSU', thicknessAssignment=FROM_SEC
TION)

    mdb.models['Model-1'].parts['Plate'].SectionAssignment(offset=0.0,
offsetField='', offsetType=MIDDLE_SURFACE, region=mdb.models['Model-
1'].parts['Plate'].sets['CL_All'], sectionName='CementLine', thicknessAssignmen
t=FROM_SECTION)

```

---

---

```

def creatStep():

    mdb.models['Model-1'].StaticStep(adaptiveDampingRatio=0.05,
    continueDampingFactors=False, initialInc=1e-05, maxInc=0.002, maxNumInc=1000,
    minInc=1e-10, name='Displacement', previous='Initial',
    stabilizationMagnitude=0.0002, stabilizationMethod=DISSIPATED_ENERGY_FRACTION)

    mdb.models['Model-1'].fieldOutputRequests['F-Output
1'].setValues(variables=('S', 'PE', 'PEEQ', 'PEMAG', 'LE', 'U', 'RF', 'CF',
'CTRESS', 'CDISP', 'PHILSM', 'PSILSM', 'ENRRTXFEM', 'STATUS', 'STATUSXFEM'))

    # Note that this line changes the maximum number of "cutbacks" abaqus
dose for each step. It's the eighth value of "timeIncrementation" The
original value is 5. I recommend a value of 15 or larger for XFEM work.

    mdb.models['Model 1'].steps['Displacement'].control.setValues(
allowPropagation= OFF, resetDefaultValues=OFF, timeIncrementation=(4.0, 8.0,
9.0, 16.0, 10.0, 4.0, 12.0, 15.0, 6.0, 3.0, 50.0))

```

---

```

def creatXFEM_CrackDomain(crackHeight):

    # Creat the XFEM crack domain

    mdb.models['Model-
1'].rootAssembly.engineeringFeatures.XFEMCrack(crackDomain=mdb.models['Model-
1'].rootAssembly.instances['Plate-1'].sets['Everything'],
crackLocation=Region(edges=mdb.models['Model1'].rootAssembly.instances['Crack
-1'].edges.findAt(((1.0, crackHeight, 0.0),)), ), name='Crack-1')

```

---

```

def creatMesh(meshSize, plateWidth, plateHeight):

    mdb.models['Model-1'].parts['Plate'].setMeshControls(elemShape=QUAD,
regions=mdb.models['Model-1'].parts['Plate'].faces.getByBoundingBox(0, 0, 0,
plateWidth, plateHeight, 0))

    mdb.models['Model-1'].parts['Plate'].seedPart(deviationFactor=0.1,
minSizeFactor=0.1, size=meshSize)

    mdb.models['Model-1'].parts['Plate'].seedEdgeBySize(constraint=FINER,
deviationFactor=0.1, edges= mdb.models['Model1'].parts['Plate'].edges.findAt(
((5, plateHeight/2-5, 0.0),), ((10.0, plateHeight/2, 0.0),), ((5,
plateHeight/2+5, 0.0),), ((0.0, plateHeight/2, 0.0),), ), minSizeFactor=0.1,
size=1.5)

    mdb.models['Model-1'].parts['Plate'].generateMesh()

```

---

```

def creatLoads(plateHeight, displacementLoad):

    # Create and set loads

    mdb.models['Model-1'].DisplacementBC(amplitude=UNSET,
createStepName='Displacement', distributionType=UNIFORM, fieldName='',
fixed=OFF, localCsys=None, name='Top Edge', region=mdb.models['Model-
1'].rootAssembly.instances['Plate-1'].sets['EdgeTop'], u1=UNSET,
u2=displacementLoad, ur3=0.0)

    mdb.models['Model-1'].DisplacementBC(amplitude=UNSET,
createStepName='Displacement', distributionType=UNIFORM, fieldName='',
fixed=OFF, localCsys=None, name='Bottom Edge', region=mdb.models['Model-
1'].rootAssembly.instances['Plate-1'].sets['EdgeBottom'], u1=UNSET, u2=0.0,
ur3=0.0)

    mdb.models['Model-1'].rootAssembly.Set(name='Top Corner',
vertices=mdb.models['Model-1'].rootAssembly.instances['Plate-
1'].vertices.findAt(((0, plateHeight, 0.0),)))

    mdb.models['Model-1'].DisplacementBC(amplitude=UNSET,
createStepName='Displacement', distributionType=UNIFORM, fieldName='',
fixed=OFF, localCsys=None, name='Top Corner', region=mdb.models['Model-
1'].rootAssembly.sets['Top Corner'], u1=0.0, u2=UNSET, ur3=0.0)

    mdb.models['Model-1'].rootAssembly.Set(name='Bottom Corner',
vertices=mdb.models['Model-1'].rootAssembly.instances['Plate-
1'].vertices.findAt(((0.0,0.0, 0.0),)))

    mdb.models['Model-1'].DisplacementBC(amplitude=UNSET,
createStepName='Displacement', distributionType=UNIFORM, fieldName='',
fixed=OFF, localCsys=None, name='Bottom Corner', region=mdb.models['Model-
1'].rootAssembly.sets['Bottom Corner'], u1=0.0, u2=0.0, ur3=0.0)

```